

DISSERTATION

SINGLE POTENTIAL ELECTRODEPOSITION OF NANOSTRUCTURED
BATTERY MATERIALS FOR LITHIUM-ION BATTERIES

Submitted by

James Matthew Mosby

Department of Chemistry

In partial fulfillment of the requirements
For the Degree of Doctor of Philosophy

Colorado State University

Fort Collins, Colorado

Summer 2010

COLORADO STATE UNIVERSITY

April 30, 2010

WE HEREBY RECOMMEND THAT THE DISSERTATION PREPARED UNDER OUR SUPERVISION BY JAMES MATTHEW MOSBY ENTITLED SINGLE POTENTIAL ELECTRODEPOSITION OF NANOSTRUCTURED BATTERY MATERIALS FOR LITHIUM-ION BATTERIES BE ACCEPTED AS FULFILLING IN PART REQUIREMENTS FOR THE DEGREE OF DOCTOR OF PHILOSOPHY.

Committee on Graduate work

C. Michael Elliott

Branka M. Ladanyi

Venkatesan Manivannan

Matthew P. Shores

Advisor: Amy L. Prieto

Department Chair: Ellen R. Fisher

ABSTRACT OF DISSERTATION

SINGLE POTENTIAL ELECTRODEPOSITION OF NANOSTRUCTURED
BATTERY MATERIALS FOR LITHIUM-ION BATTERIES

The increasing reliance on portable electronics is continuing to fuel research in the area of low power lithium-ion batteries, while a new surge in research for high power lithium-ion batteries has been sparked by the demand for plug-in hybrid electric vehicles (PHEV) and plug-in electric vehicles (PEV). To compete with current lead-acid battery chemistry, a few of the shortcomings of lithium-ion battery chemistry need to be addressed. The three main drawbacks of lithium-ion batteries for this application are: (1) low power density, (2) safety, and (3) the high cost of manufacturing. This dissertation covers the development of a low cost fabrication technique for an alternative anode material with high surface area geometries. The anode material is safer than the conventional anode material in lithium-ion batteries and the high surface area geometries permit higher power densities to be achieved.

Electrodeposition is an inexpensive alternative method for synthesizing materials for electronics, energy conversion and energy storage applications relative to traditional solid state techniques. These techniques led to expensive device fabrication. Unlike most solid state synthesis routes, electrodeposition can usually be performed from common solutions and at moderate conditions. Three other benefits of using electrodeposition are:

(1) it allows precise control of composition and crystallinity, (2) it provides the ability to deposit on complex shapes, and (3) it can deposit materials with nanoscale dimensions. The use of electrodeposition for alternative anode materials results in the deposition of the material directly onto the current collector that is used for the battery testing and applications without the need of additional binders and with excellent electrical contact. While this improves the characterization of the material and lowers the weight of the non-active materials within a battery, it also allows the anode to be deposited onto current collectors with different sizes, shapes, and surface areas. This is advantageous because high surface area materials benefit from improved kinetics for solid state transformations and from decreases in mechanical degradation that occurs during the lithiation and delithiation of battery materials.

Intermetallic materials are an alternative to conventional anode materials because they have high capacities and react reversibly with lithium at potentials that hinder the dendrite formation of metallic lithium. Unfortunately, the volume expansion associated with the lithiation and delithiation of intermetallic materials is usually large (over 300%). With this in mind a procedure for the electrodeposition of Cu_2Sb from aqueous solutions was developed and is presented in this thesis. Cu_2Sb is an intermetallic that lithiates at potentials more positive than the potential needed to plate lithium metal, and has a volume expansion less than 100%. Electrodeposition of an intermetallic with a relatively small volume expansion and with high surface area morphology should dramatically reduce material degradation during battery cycling, thus promoting the life of the material.

To electrodeposit Cu_2Sb from aqueous solutions, soluble salts of Cu^{2+} and Sb^{3+} were needed. There are many Cu^{2+} salts that are highly soluble in water, but most Sb^{3+} salts cause formation of Sb_2O_3 in aqueous solutions. To obtain Sb^{3+} in aqueous solutions, citric acid was used as a complexing agent. The results presented in this dissertation show that solution speciation plays an important role in the electrochemistry of aqueous citrate solutions of both copper and antimony. The cyclic voltammograms (CVs) presented here show that the reduction potential of Cu^{2+} shifted in the negative direction and the reduction potential of Sb^{3+} shifted in the positive direction with an increase in pH. Also, Cu_2Sb films were deposited at a single potential (-1050 mV vs. SSCE) from aqueous solutions at pH 6. We determined that the deposition potential not only affected the crystallinity of the deposited Cu_2Sb , but also the ratio of antimony to copper. The temperature of the solution bath, as well as the smoothness of the growth substrate, were found to provide control over the crystallinity of the deposited Cu_2Sb . The ability to electrodeposit crystalline Cu_2Sb onto a variety of conducting surfaces is uncommon for intermetallics.

The ability to deposit Cu_2Sb onto transmission electron microscopy (TEM) grids has allowed the investigation of the morphology, composition, and crystallinity of Cu_2Sb during the nucleation and growth of the material. This investigation demonstrated that multiple transformations occur during the early stage of the nucleation of Cu_2Sb . A deeper understanding of this electrodeposition procedure for this compound will be useful for extending this technique to other crystalline intermetallics. Using the procedure developed for the single potential deposition of Cu_2Sb films, the information from the TEM investigation and the results of a qualitative mathematical treatment, a

pulse potential deposition procedure for depositing Cu_2Sb nanowire arrays was developed. This procedure leads not only to the deposition of crystalline Cu_2Sb nanowires, but also to uniform filling of the templates to afford wires of uniform composition and length.

After the development of the procedures for the electrodeposition of Cu_2Sb films and nanowire arrays from aqueous solutions at a single potential, the battery performance of the deposited Cu_2Sb was examined. The ability to directly electrodeposit Cu_2Sb onto the current collector has: (1) improved the characterization of the material during the lithiation and delithiation processes, (2) decreased the weight of inactive components, and (3) allowed for the deposition of high surface area Cu_2Sb . The preliminary battery testing of electrodeposited Cu_2Sb supported the absence of impurities in the deposited material and demonstrated that the electrodeposited Cu_2Sb lithiated and delithiated similarly to Cu_2Sb synthesized with different techniques. The deposition of Cu_2Sb onto TEM grids was used for the first time without binder to characterize the morphology, composition and crystallinity changes that occur during the lithiation and delithiation of Cu_2Sb . Superior capacity retention and rate performance was achieved with Cu_2Sb electrodeposited onto high surface area copper foil. This superior performance demonstrates the improvement in battery performance that is expected from Cu_2Sb nanowires, which have an order of magnitude higher surface area relative to the copper foam.

James Matthew Mosby
Department Chemistry
Colorado State University
Fort Collins, Co 80523
Summer 2010

SINGLE POTENTIAL ELECTRODEPOSITION OF NANOSTRUCTURED BATTERY MATERIALS FOR LITHIUM-ION BATTERIES

TABLE OF CONTENTS

1	Anode Materials for Li-ion Batteries	
1.1	The basics of Li-ion battery technology.....	2
1.2	Graphite's dominance as an anode material	6
1.3	Alternative anode materials.....	9
1.4	Antimonide anode materials.....	12
1.5	Current synthesis routes for battery materials.....	18
1.6	References.....	20
2	Electrodeposition of Cu ₂ Sb Nanowire Array	
2.1	Benefits of using electrodeposition as synthesis and fabrication route.....	23
2.2	The improvements in properties expected from arrays of Cu ₂ Sb nanowires.....	26
	Using AAO templates to grow arrays of Cu ₂ Sb nanowires.....	31
2.3	Complications that arise during deposition of intermetallic materials.....	33
2.4	References.....	36
3	Solution Chemistry Relevant to Copper-Antimony-Citrate Aqueous System	
3.1	Avoiding the formation of Sb ₂ O ₃ in aqueous solutions.....	41
3.2	Experimental procedures.....	43
3.3	Initial solution electrochemistry.....	46
3.4	The pH dependence of the electrochemistry of citric acid.....	50
3.5	The pH dependence of the electrochemistry of copper citrate.....	53
3.6	The pH dependence of the electrochemistry of antimony citrate.....	57
3.7	The pH dependence of the electrochemistry of antimony copper citrate.....	61
3.8	Conclusions.....	65
3.9	References.....	66
4	The Single Potential Deposition of Cu ₂ Sb films	
4.1	Introduction.....	69
4.2	Experimental procedures.....	69
4.3	Optimizing the deposition potential.....	71

4.4	Temperature effect on crystallinity.....	76
4.5	Cu ₂ Sb electrodeposited from aqueous solutions.....	78
4.6	Conclusions.....	84
4.7	References.....	85
5	Nucleation Process Involved In the Single Potential Deposition of Cu ₂ Sb	
5.1	Microscopy studies of electrodeposition nucleation.....	87
5.2	Experimental procedures.....	91
5.3	Characterization.....	93
5.4	Electrodeposition of Cu ₂ Sb onto TEM grids.....	94
5.5	Scanning electron microscopy.....	96
5.6	Transmission electron microscopy.....	99
5.7	Discussion.....	103
5.8	Proposed deposition mechanism based on solution chemistry and nucleation processes.....	107
5.9	Conclusions.....	109
5.9	References.....	110
6	Electrodeposition of Cu ₂ Sb Nanowire Arrays	
6.1	Introduction.....	113
6.2	Experimental procedures.....	113
6.3	Cu ₂ Sb nanowire arrays obtained using procedure for Cu ₂ Sb films.....	115
6.4	Introduction to pulse potential electrodeposition of Cu ₂ Sb nanowire array.....	117
6.5	Optimizing the pulse potential deposition of Cu ₂ Sb films.....	119
6.6	Optimizing the pulse potential deposition of Cu ₂ Sb nanowire arrays.....	121
6.7	Pulse potential deposition of Cu ₂ Sb onto gold substrates.....	124
6.8	Modified pulse potential deposition based on theory and TEM investigation.....	128
6.9	Conclusions.....	132
6.10	References.....	132
7	Mathematics of Pulse Potential Deposition	
7.1	Introduction to math of pulse deposition.....	134
7.2	Mathematical treatment of potential pulse deposition.....	139
7.3	Conclusion.....	148
7.4	References.....	149
8	Battery Performance of Cu ₂ Sb Material	
8.1	Introduction.....	151
8.2	Experimental procedures.....	151
8.3	Voltage profile of electrodeposited Cu ₂ Sb films.....	157
8.4	Lithiation and de-lithiation of Cu ₂ Sb deposited onto TEM grids.....	161
8.5	Cycling performance of electrodeposited Cu ₂ Sb.....	170
8.6	Conclusions.....	172
8.7	References.....	173
9	Optimizing the Battery Performance of Cu ₂ Sb Material	
9.1	Introduction.....	175

9.2 Experimental procedures.....	175
9.3 The effect of the Cu ₂ Sb film thickness of cycle performance.....	176
9.4 Cycling performance of Cu ₂ Sb based on potential limits.....	180
9.5 Cycling performance of high surface area Cu ₂ Sb	184
9.6 Cycle performance of Cu ₂ Sb nanowires.....	188
9.7 Conclusions.....	190
9.8 References.....	191
10 Conclusions	
10.1 Single potential deposition of Cu ₂ Sb thin films from aqueous solutions.....	193
10.2 Optimizing the Cu ₂ Sb film deposition.....	193
10.3 Electron microscopy investigation of the electrodeposition of Cu ₂ Sb.....	194
10.4 Pulse potential deposition of Cu ₂ Sb nanowire arrays.....	195
10.5 Preliminary Cu ₂ Sb battery testing.....	196
10.6 Optimizing the battery performance of Cu ₂ Sb.....	196

LIST OF FIGURES

Figure 1.1	Schematic of conventional lithium-ion battery	3
Figure 1.2	Lithiation and delithiation of natural graphite.....	8
Figure 1.3	Comparison of the capacity of different anode material.....	10
Figure 1.4	Cycle performance of Sn and Sn alloys.....	12
Figure 1.5	Crystal structures of the Cu_2Sb , Li_2CuSb , Li_3Sb	15
Figure 1.6	Potential profile of the lithiation and delithiation of Cu_2Sb	16
Figure 2.1	Examples of electrodeposited nanostructures from literature.....	25
Figure 2.2	Schematic of 3D nanowire array battery.....	30
Figure 2.3	Schematic of nanowire array with and without separator.....	31
Figure 3.1	Drawing of citric acid.....	43
Figure 3.2	Cyclic voltammograms of citrate solutions at pH 1.2.....	48
Figure 3.3	Cyclic voltammograms of citrate solutions at pH 6.....	49
Figure 3.4	Cyclic voltammograms of citric acid at different pHs.....	51
Figure 3.5	Calculated speciation diagram of citric acid.....	52
Figure 3.6	Cyclic voltammograms of copper citrate at different pHs.....	53
Figure 3.7	Calculated speciation diagram of copper citrate solution.....	55
Figure 3.8	Calculated speciation diagram of antimony citrate solution.....	57
Figure 3.9	Cyclic voltammograms of antimony citrate at different pH.....	58
Figure 3.10	Cyclic voltammograms of antimony, copper citrate solutions at different pHs.....	60
Figure 3.11	Cyclic voltammograms of deposition solution on different working electrodes.....	62
Figure 4.1	X-ray photoelectron spectroscopy of electrodeposited Cu_2Sb	65
Figure 4.2	X-ray diffraction of Cu_2Sb films deposited at different potentials.....	73
Figure 4.3	Scanning electron microscopy images of Cu_2Sb films deposited at different potentials.....	74
Figure 4.4	X-ray diffraction of Cu_2Sb films deposited at different temperatures.....	75
Figure 4.5	Scanning electron microscopy images of Cu_2Sb films deposited at different temperatures.....	77
Figure 4.6	X-ray diffraction of Cu_2Sb films using optimized electrodeposition procedure.....	78
Figure 4.7	X-ray diffraction of annealed Cu_2Sb film electrodeposited with optimized procedure.....	79
Figure 4.8	Scanning electron microscopy image of the cross section of a Cu_2Sb film.....	80
Figure 4.9	X-ray diffraction of Cu_2Sb film deposited on gold substrate.....	81

Figure 4.10	X-ray diffraction patterns of Cu ₂ Sb films deposited on untreated substrates.....	82
Figure 5.1	Cyclic voltammograms of deposition solution on transmission electron microscopy grids.....	84
Figure 5.2	Fitting Cu ₂ Sb electrodeposition curve to the nucleation models for progressive and instantaneous nucleation.....	93
Figure 5.3	Scanning electron microscopy images of the density of Cu ₂ Sb nucleation sites.....	97
Figure 5.4	Scanning electron microscopy and energy dispersive spectroscopy of the morphology of the nucleation sites	99
Figure 5.5	Transmission electron microscopy images of the Cu ₂ Sb nucleation sites after a deposition of 0.1 s and 0.25 s.....	100
Figure 5.6	Transmission electron microscopy images of the Cu ₂ Sb nucleation sites after a deposition of 0.5 s and 1.0 s.....	102
Figure 5.7	Energy dispersive spectroscopy of Cu ₂ Sb nucleation sites at the different nucleation times.....	103
Figure 5.8	Schematic of Cu ₂ Sb deposition.....	105
Figure 5.9	Maximum current of reduction peak versus scan rate of different citrate solutions.....	108
Figure 6.1	X-ray diffraction of Cu ₂ Sb nanowire arrays deposited with single potential.....	116
Figure 6.2	Scanning electron microscopy images of Cu ₂ Sb nanowire arrays grown with single potential.....	117
Figure 6.3	Schematic of the square wave single for the pulse potential deposition.....	119
Figure 6.4	X-ray diffraction of Cu ₂ Sb film deposited using pulse potential deposition	121
Figure 6.5	X-ray diffraction of Cu ₂ Sb nanowire array using pulse deposition.....	122
Figure 6.6	Scanning electron microscopy images of Cu ₂ Sb nanowire arrays deposited with pulse potential deposition.....	123
Figure 6.7	Experimental current profile of pulse potential deposition of Cu ₂ Sb on gold.....	126
Figure 6.8	X-ray diffraction of Cu ₂ Sb film pulse potential deposited on gold substrate.....	128
Figure 6.9	Experimental potential and current profile of pulse potential deposition of Cu ₂ Sb nanowire array.....	129
Figure 6.10	X-ray diffraction of Cu ₂ Sb nanowire arrays deposited with pulse potential deposition.....	130
Figure 6.11	Scanning electron microscopy of Cu ₂ Sb nanowire arrays deposited with pulse potential deposition.....	131
Figure 7.1	Circuit diagram used to model current profile.....	135
Figure 7.2	Schematic of diffusion profile from a pulse deposition.....	137
Figure 7.3	Calculated current profile for a single potential step deposition.....	142
Figure 7.4	Calculated concentration profile for a single potential step deposition.....	143
Figure 7.5	Calculated current profile for pulse potential deposition.....	145

Figure 7.6	Calculated concentration profiles for single potential and pulse potential deposition.....	147
Figure 7.7	Calculated concentration profile for pulse potential deposition of Cu_2Sb	148
Figure 8.1	Potential profiles of the lithiation and delithiation of Cu_2Sb taken with different potentiostats.....	154
Figure 8.2	Schematics of Swagelok cells used for battery testing.....	156
Figure 8.3	Potential profile of the lithiation and delithiation of Cu_2Sb at slow rates.....	158
Figure 8.4	Potential profile of the charge and discharge of a $\text{Cu}_2\text{Sb}/\text{LiCoO}_2$ full cell.....	160
Figure 8.5	Scanning electron microscopy images of Li_2CuSb at first charge plateau.....	162
Figure 8.6	Scanning electron microscopy image of Li_3Sb at second lithiation plateau.....	164
Figure 8.7	Transmission electron microscopy image of Li_2CuSb at first charge plateau.....	165
Figure 8.8	Transmission electron microscopy image of Li_3Sb at second lithiation plateau.....	166
Figure 8.9	Scanning electron microscopy image of fully lithiated material.....	167
Figure 8.10	Scanning electron microscopy image of Cu_2Sb after lithiation and delithiated using slow rates.....	169
Figure 8.11	Scanning electron microscopy image of Cu_2Sb after lithiation and delithiated using fast rates.....	170
Figure 8.12	Cycle performance of Cu_2Sb films using different potentiostats.....	171
Figure 9.1	Cycle performance of Cu_2Sb films based on thickness.....	178
Figure 9.2	Scanning electron microscopy image of solid electrolyte interface composite.....	179
Figure 9.3	Scanning electron microscopy image of the cross section of solid electrolyte interface composite	180
Figure 9.4	Cycle performance of Cu_2Sb films using a lower potential limit of 600 mV vs. Li/Li^+	182
Figure 9.5	Cycle performance of Cu_2Sb films using a lower potential limit of 500 mV vs. Li/Li^+	184
Figure 9.6	Scanning electron microscopy image of high surface area copper sponge with Cu_2Sb	185
Figure 9.7	Cycle performance of Cu_2Sb on higher surface area copper sponge	187
Figure 9.8	Potential profiles of the lithiation and delithiation of Cu_2Sb nanowires.....	189
Figure 9.10	Scanning electron microscopy images of Cu_2Sb nanowire arrays after cycling versus lithium metal.....	190

LIST OF TABLES

Table 3.1	Concentrations of copper and antimony in Cu_2Sb electrodeposition solutions.....	45
Table 4.1	X-ray photoelectron spectroscopy composition data of Cu_2Sb films deposited at different potentials.....	72
Table 6.1	Table of pulse potential deposition parameters for electrodeposition of Cu_2Sb films.....	120
Table 6.2	Table of pulse potential deposition parameters for electrodeposition of Cu_2Sb nanowire arrays.....	122
Table 6.3	Table of pulse potential deposition parameters for electrodeposition of Cu_2Sb films on gold substrates.....	127
Table 9.1	Different discharge rates used to investigate Cu_2Sb deposited on high surface area copper sponge.....	186

ACKNOWLEDGMENTS

The work reported in this thesis is only part of the vast experience that has made up my Ph. D. studies at the department of chemistry at Colorado State University. Behind this research, were experiences and interactions with people that cannot be described on paper. The science presented stems from the rich opportunities presented to me throughout my degree. Looking back at the beginning of my Ph. D. studies, I never pictured myself being lucky enough to participate in the projects and with the people that now I take for granted every day. Sometimes it all feels like a dream. Yet, It has not all been glory. This experience has pushed me past my breaking point both mentally and physically many times. Getting through the bad and enjoying the good was not because of any personal strength that I hold, it is from the people that have supported me throughout the last five years.

First, I would like to thank those who directly impacted my everyday life as a graduate student. This includes the people in my research group, some who started at the same time as I did and some who have since joined. From long group meetings, to dealing with me day after day for five years these people continued to provide fruitful discussions and moral support throughout the different hurdles that I encountered. With this group, I need to thank other graduate students that have become my friends and have laughed and griped with me along the way. In particular I need to thank a post doc (Derek Johnson), who has helped me become the scientist that I am today, while experimenting with all of the crazy ideas that we came up with (during brain storming sessions) that have provided some of the interesting experimental results

reported where in. I also need to thank the friends that have put up with me since high school, always providing a means to escape the pain of graduate school.

Second, I would like to thank the people who have become my mentors during the last five years. The professors in the Department of Chemistry have always treated me with respect whether I deserved it or not. Professors with open doors, open minds, and always willing to take time (which they don't have) to help with even the most minute things makes the Department of Chemistry at CSU a special place. They have provided me with knowledge that has pushed every aspect of my research and opportunities that I never thought would be presented to me.

In particular I need to thank my advisor, Amy Prieto. Since she introduced me to my new love (solid-state chemistry), and provided a learning environment which allowed me to accomplish the unthinkable. She let me think freely and follow ideas that sometimes didn't have a clear purpose. Yet, she kept me focused on what I needed to do to complete this stage of my career. During times that I questioned my reasons for being a graduate student she convinced me that I wasn't wasting my time. When most were sleeping (past midnight) she helped with papers, presentations and random questions. Through personal life changing events she never stopped supporting me throughout this process. I hope that the work presented in this thesis represents a fraction of what she taught me.

Lastly, I need to thank my family. A group of people who have watched a kid who asked too many questions, partied too much in high school, reinvented himself in college, get lost in the field of chemistry. The support my family has provided along every step of my life which has led me to where I am today and continued through my graduate studies even though I have spent less and less time being part of their life is something I will never be able to pay back. I

will never take for granted the sacrifice that my wife Heidi and my kids Cayden and Ayden have had to endure while I enjoyed submersing myself in solid-state chemistry.

Enjoy!!

CHAPTER 1

ANODE MATERIALS FOR LITHIUM-ION BATTERIES

1.1 The basics of Lithium-ion battery technology

Rechargeable lithium-ion batteries are the current choice to power portable electronics, accounting for 63% of portable battery sales worldwide.² The reliance on lithium-ion batteries in the portable electronic industry is compared to metallic lithium, which has safety issues, lithium-ion batteries have the highest volumetric and gravimetric energy density.² The high energy density is coupled with long cycle life. These two properties of lithium-ion batteries are superior over other battery chemistries and has secured their use in the portable electronic market.² Increasing reliance on portable electronics is continuing to fuel research in low power lithium-ion batteries, while a new surge in research for high power lithium-ion batteries has been sparked by the need of plug-in hybrid electric vehicles (PHEV) and plug-in electric vehicles (PEV). To compete with the nickel-metal hydride battery chemistry that is currently being used in this market a few of the short comings of the lithium-ion chemistry need to be addressed. The two main shortcomings of lithium-ion batteries for this application are: (1) low power density and (2) safety. Before these are discussed in detail the basics of a lithium-ion battery will be reviewed.

A lithium-ion battery is made up of electrochemical cells which are connected in series and parallel such that the appropriate voltage and capacity are obtained for the application of interest. The conventional cell used in most portable electronic equipment consists of cathode (LiCoO_2) and anode (LiC_6) materials that are physical separated by an electrically insulating porous membrane which is saturated in the electrolyte solution. A schematic of a typical lithium-ion cell in the charged state is shown in Figure 1.1 using graphite and LiCoO_2 as example materials. In the charged state the graphite is lithiated

and the LiCoO_2 is delithiated. As a load is placed across the copper current collector on the anode and the aluminum current collector on the cathode, electrons pass through the anode and the aluminum current collector on the cathode, electrons pass through the load while lithium-ions pass through the electrolyte (maintaining charge balance). When the polarity is reversed and the cell is charged the electrons flow into the anode accompanied by lithium-ions. A simplified energy diagram is superimposed onto the cell schematic and shows that in order for the electrons to pass through a load and not short the cell, the electrolyte must fulfill two requirements. The first requirement is the energy of the lowest unoccupied molecular orbital (LUMO) of the electrolyte must be higher in energy than the highest occupied molecular orbital (HOMO) of the anode. The second requirement is the LUMO of the cathode must be higher in energy than the HOMO of the electrolyte.

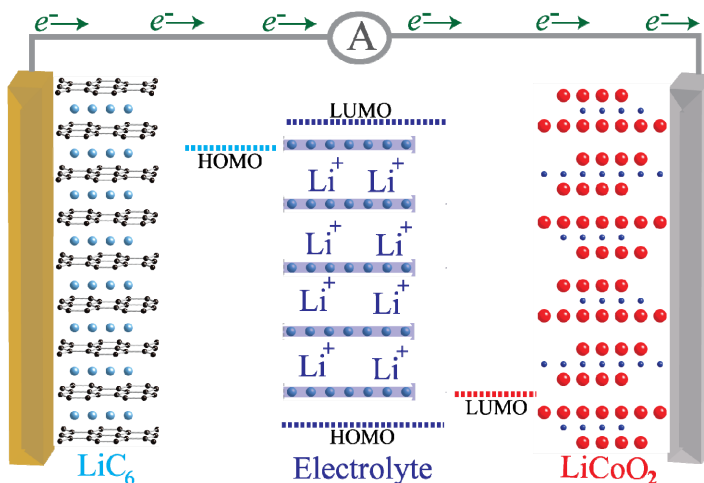


Figure 1.1: Schematic of the discharge of a charged lithium-ion cell. The anode (graphite) is on the left, while the cathode (LiCoO_2) is on the right. The two electrodes are separated by an electrolyte, which inhibits e^- s from passing but allows the diffusion of Li^+ . An energy diagram showing the required relative position of the HOMO and LUMO of the different materials is superimposed onto the schematic.

A side note on convention for secondary batteries needs to be addressed here. As a battery cell is discharged the spontaneous electrochemical reaction provides electrons to

the external circuit to do work and thus the cell is acting as a galvanic cell. During the discharge electrons are flowing to the CoO_2 which reduce the Co^{4+} to Co^{3+} and thus based on Faraday's definition the CoO_2 is called the cathode.⁴ The lithium-ions are being formed by the oxidation of lithium occurring at the LiC_6 and thus the graphite is the anode.⁴ Upon charging the battery cell, it becomes an electrolytic cell because a power source is used to reverse the chemical reaction, causing the reduction to occur at the graphite electrode and the oxidation to occur at the lithium cobalt oxide electrode. Following Faraday's definition of a cathode the graphite during the charge process is the cathode and the anode is the lithium cobalt oxide. This confusion is simplified by referring to the electrode which by Faraday's definition is the cathode as the cell is acting as a galvanic cell as the cathode of the battery cell (LiCoO_2). Likewise, the electrode which by Faraday's definition is the anode as the cell is acting as a galvanic cell is referred to as the anode of the battery cell (C_6).

On top of this confusion is that both cathode and anode materials for lithium-ion batteries are tested in "half cells" versus lithium metal. According to the convention just described this means that both cathode (LiCoO_2) and anode (C_6) materials are the cathode in these half cells. This leads to false reports in the literature as papers describe "Ultra High Capacity Cathode Material...." for which the material would be the anode material (with poor capacity) in a full lithium-ion cell, but it is tested in a half cell which by convention it is the cathode (only in a lithium metal battery). To circumvent this confusion in this thesis the electrode materials will be assigned as cathode materials *if they fit Faraday's definition of a cathode material in a full lithium-ion cell during the galvanic process*. Similarly anode materials in this thesis will refer to materials that *fit*

Faraday's definition of an anode material in a full lithium-ion cell during the galvanic process.

The electrodes used in conventional lithium-ion batteries consist of the active materials suspended within a conducting slurry, which is then applied to a current collector and dried. The slurry is made of 80% active material and 20% inactive material. The inactive material consists of a polymer (poly-vinylidene fluoride) and a conducting carbon (graphite powder). The slurry has two major roles: (1) it provides electrical contact between the current collector and active material, and (2) it provides mechanical stability for the active material during the charge and discharge process. The common current collectors used for lithium ion batteries are copper for the anode and aluminum for the cathode. The electrodes within a battery cell are separated by a micro-porous polypropylene membrane. The membrane and void space of the cell are filled with a non-aqueous electrolyte solution, commonly 1M LiPF_6 in ethylene carbonate(EC)/diethylene carbonate(DEC) (1:1 v:v.). Improvements are being sought for all three main components of lithium-ion batteries in order to improve the capacity, power and safety.

There are two routes that researchers are currently pursuing to improve the cathode and anode materials. The first is exploring new materials that can store large amounts of lithium, and/or have fast lithium insertion kinetics. The second is to use nano-scale morphologies to decrease the lithium-ion diffusion path lengths, and improve material stability. It has been shown that the cycle performance and rate capabilities of anode and cathode material with nanoscale morphology are greatly improved over the same material with bulk dimensions.⁵⁻¹⁴ In this context cycle performance refers to

capacity retention as a function of cycle number, while rate capability refers to the capacity obtained when the material is charged/discharged with high current densities. The most obvious improvement is in the charge and discharge rate of a material. Because the diffusion of the lithium within the cathode and anode is solid-state diffusion, the shorter the distance the lithium travels within an electrode, and thus the faster a lithium-ion can be inserted and removed. Thus, short diffusion distances lead to improvements in high power performance. A less obvious improvement from reducing the material dimensions is the decrease in material degradation. The improvement is because materials with small dimensions have lower overall energy strain during volume changes and thus pulverize less than bulk material. For the electrolyte, current research is focused on new materials that improve the electronic and thermal stability of the electrolyte while increasing the lithium-ion conductivity.¹⁵

The primary goal for this research is to improve the rate performance and cycle stability of an anode material for lithium-ion batteries. This goal was achieved by using a new anode material (Cu_2Sb) with nanoscale morphologies. The properties of Cu_2Sb that make it a good alternative to graphite as an anode material for lithium-ion batteries and the improvements from using nanoscale morphology will be discussed later. First, some of the standard properties of graphite-based anodes will be discussed.

1.2 Graphite's dominance as an anode material

Lithium metal batteries are plagued by dendritic metallic lithium forming during repeated charge and discharge cycles. These penetrate the separator layer, reducing cycle life and causing safety concerns. By using carbon as a host material Sony was the first to commercialize lithium-ion batteries.¹ The carbon host inhibited the formation of

dendritic lithium and thus improved the cycle life and safety of the battery. Depending on the type of carbon used the capacity can range from 250 mAh g^{-1} to 500 mAh g^{-1} .¹ As already mentioned the carbon is typically suspended within a slurry which is cast upon the copper current collector. For high power applications the carbon particle diameter is minimized through grinding before being intimately mixed with the slurry.¹ Although reversible capacities of 450 mAh g^{-1} have been reported, the practical capacity of commercialized graphite electrodes is 350 mAh g^{-1} with a theoretical capacity of 372 mAh g^{-1} (LiC_6).¹⁶

The difference between graphite's practical and theoretical capacity is from the unavoidable formation of a solid-electrolyte-interface (SEI), which forms as different electrolyte components are degraded at the low potentials needed to lithiate the carbon material. The formation of the SEI consumes lithium-ions leading to irreversible capacity loss. Figure 1.2 is an example of the potential profile of natural graphite during the first lithiation and delithiation (adopted from Flandrois *et al.*¹). During the first charge of the natural graphite at constant current the potential quickly drops from the open circuit potential ($3000 \text{ mV vs. Li/Li}^+$) before a voltage plateau is found at $800 \text{ mV vs. Li/Li}^+$ (Figure 1.2a). Following this plateau three more voltage plateaus representing the different stages of graphite lithiation are encountered below $300 \text{ mV vs Li/Li}^+$. Upon discharging the natural graphite, the three plateaus below $300 \text{ mV vs Li/Li}^+$ are still present, but the first plateau in the charge curve at $800 \text{ mV vs. Li/Li}^+$ is not seen (Figure 1.2b).¹

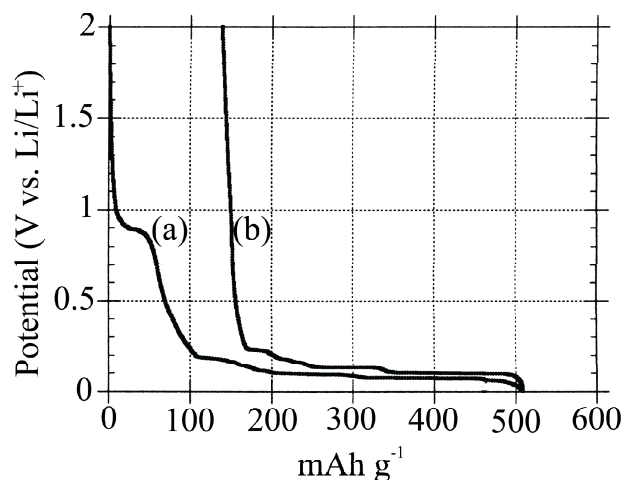


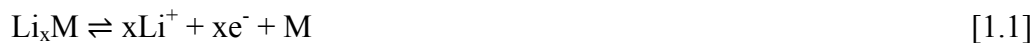
Figure 1.2: Potential profiles of the lithiation **(a)** and dilithiation **(b)** of natural graphite. The voltage is versus Li^+/Li . The graphite was tested in a coin cell in 1M LiPF_6 propylene carbonate (PC), ethylene carbonate (EC), dimethyl carbonate (DMC) (1:1:1 by vol.), at a rate of 20 mA g^{-1} . Adopted from Flandrois *et al.*¹

The first plateau at 800 mV vs. Li/Li^+ in Figure 1.2a is the irreversible formation of the SEI layer, and therefore no charge is obtained at this voltage during the discharge of the material (Figure 1.2b). This reduces the capacity of natural graphite to 150 mAh g^{-1} . The three plateaus below 300 mV vs. Li/Li^+ in Figure 1.2 corresponding to the different stages of the lithiation of graphite are sometimes not distinguishable, depending on the type of the graphite used.¹ To charge the graphite material commonly used in lithium-ion batteries requires potentials lower than 100 mV vs. Li/Li^+ . The proximity of this potential to the potential needed to plate metallic lithium can lead to dendrite formation of lithium metal (as in the case with lithium metal batteries). Apart from this safety concern, carbon based anode materials have been used in lithium-ion batteries for over thirty years based on three key properties. These three properties are: (1) a higher capacity than the conventional cathode materials (such as LiCoO_2), (2) a low lithiation voltage (providing a 3500 mV cell vs. LiCoO_2), and (3) after the first irreversible capacity loss, good cycle life.

Research into alternative anode materials to graphite for lithium-ion batteries has been driven by the desire to (1) increase the capacity of the material, and (2) reduce the risk of lithium dendrite formation. Finding an anode material with a higher capacity than carbon will decrease the weight and thus increase the capacity of a battery. However, the benefit of high capacity anode materials is limited. This is because the capacity of the cathode is the current limiting factor that needs to be addressed in order to increase the energy density of lithium-ion batteries. This means there is a limited return that can be reached with high capacity anode materials until new high capacity cathode materials are found. As mentioned previously the potential required to lithiate carbon materials is low enough that lithium dendrites can still form. This, as well as thermal runaway reactions of the electrolyte at these low potentials have caused serious safety issues, brought to the public eye with laptop fires.¹⁷

1.3 Alternative anode materials

One of the main classes of materials investigated as alternatives to graphite are Li alloys which have seen some commercial success by Sony[®] and Fuji[®].³ The basis of using lithium alloys as anode material stems from the highly reversible reactions of numerous elements with lithium metals according to Eq. 1.1.³



Eq. 1.1 is highly reversible and in some cases the lithium is stored in the host material as a ion and not elemental lithium which allows high densities of lithium to be stored in the material allowing theoretical specific gravimetric and volumetric capacities close to that of metallic lithium.³ Examples of the specific capacities of certain alternative anode materials are shown in Figure 1.3. The first thing that is apparent from Figure 1.3 is that

that silicon has a much larger gravimetric and volumetric capacity than metallic lithium. After careful examination it can be seen that most of the alternative anode materials shown in Figure 1.3 have a higher volumetric capacity of lithium metal with graphite having the smallest.

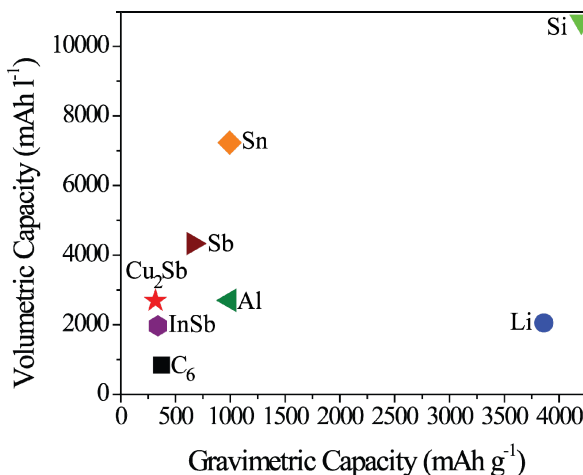


Figure 1.3: Specific volumetric and gravimetric capacity of anode materials for lithium-ion batteries. Values were calculated from number of lithium inserted per formula unit of the highest lithiated form. Volumetric capacities were calculated using crystallographic densities from ICSD.

Another benefit of the alternative anode materials shown in Figure 1.3 (except C₆, Li, and Si) is the lithiation potentials are usually above 100 mV vs. Li/Li⁺, which is positive enough to diminish the possibility of growing dendrites of metallic lithium.³ Although these lithium alloys have higher capacities than graphite, they have been plagued by limited cycle life. The poor cycle performance is caused by large volume expansion that occurs during the lithiation and delithiation of the alloys. Besides lithium metal the top materials shown in Figure 1.3 have a volume change for the charge and discharge over 300%. The large volume expansion of these brittle materials produces mechanical stresses that lead to the pulverization of the material, which typically causes failure within the first couple of cycles.³

Fuji Photo Celltec Co. found a way to reduce the pulverization of amorphous tin oxide in the 1990s which led to the commercialization of the “Stalion” lithium cell.³ One of the techniques used to decrease the pulverization is to control the amount of lithiation. There are multiple lithium-tin phases that can be reached during the lithiation at room temperature with a ratio of lithium to tin from 0.4-4.4.³ If only one lithium per tin is added providing a theoretical capacity of 213.3 mAh g^{-1} , the volume expansion is kept minimal and the degree of pulverization is reduced dramatically.³ Another technique that is used to decrease the pulverization of tin electrodes during cycling is changing the shape, size, porosity and texture of the tin.³ This was demonstrated by Winter *et al.* by comparing the cycle performance of electrodeposited thin films of tin. The electrodeposited thin film with fine grain structure was found to have greater mechanical stability than the electrodeposited film with large grain structure.³ These two techniques improved the cycle performance of tin anodes, but the capacity loss due to pulverization is still too great to be commercially viable.

Fuji’s amorphous tin oxide anode material had a stable capacity of 600 mAh g^{-1} and used another concept to improve the cycle performance of the material. The concept was to use an inactive host material (SnO , B_2O_3 , $\text{Sn}_2\text{P}_2\text{O}_7$, Al_2O_3) to improve structural integrity. During the first reaction the lithium reacts with the oxygen from the tin oxide irreversibly forming Li_2O , freeing the tin, which reacts reversibly with lithium.¹⁷ The basis of the idea is to disperse the reactive particles within a mixed-conducting metallic matrix. The inactive matrix should allow rapid transport of the lithium-ions and provide a mechanical stability to the active material forcing it to keep its microstructure during the charge and discharge. There was a considerable amount of research performed on

both mixed inorganic and polymeric host material in the late 1990s, which demonstrated that using small (<200 nm) particles of active material greatly improved the cycle performance of the material.³ The cycle performance of alloys far exceeded that of single element materials. One example from Winter *et al.* is shown in Figure 1.4, which shows the cycle performance of electrodeposited Sn, Sn/SnSb and Sn/SnAg₃/SnAg₄ alloys.³ cycle performance exceeded that of electrodeposited tin.³ The electrodeposited tin (Figure 1.4a) lost almost all capacity after 25 cycles as compared to both alloys (Figure 1.4b and C) which still had 95% of the original capacity after 150 cycles.³ Results, such as those shown in Figure 1.4 demonstrated that the smaller the domains of active and host material the better the cycle performance.³

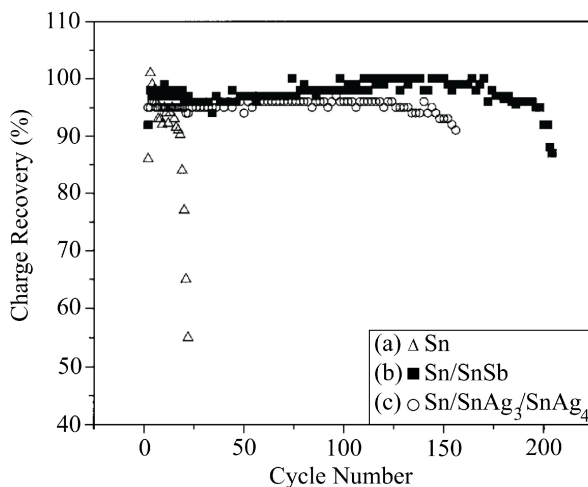


Figure 1.4: Cycle performance of electrodeposited (a) Sn, (b) Sn/SnSb and (c) Sn/SnAg₃/SnAg₄ on copper substrates in 1 M LiClO₄/PC. A current density of 0.25 mA cm⁻² and a voltage cut-off of 1.2 V vs. Li⁺/Li was used for the cycling. Adopted from winter *et al.*³

1.4 Antimonide anode materials

The next step in the progression of using active materials within a host matrix with small domains was to investigate intermetallic materials in which one element acts as a host matrix and the other exchanges with the lithium-ions during the charge and

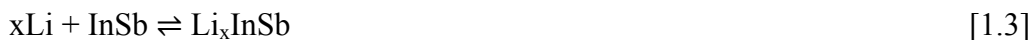
discharge. The volume change of such an intermetallic is small in comparison to the single element material discussed above, because the host material only has to expand and contract to account for the size difference between the lithium-ion and second element that is exchanged by lithium. J. T. Vaughey, J. O'Hara, and M. M. Thackeray, were the first to report the use of InSb as an anode material for lithium-ion batteries, exploiting the face centered cubic (fcc) arrangement of the antimony atoms that is maintained for the duration of the charge and discharge.¹⁸ During the first two steps of the charge process the lithium-ions insert into the interstitial sites of the zinc-blende framework ending up with Li_2InSb causing only a 1.8% change in volume.¹⁸ Further lithiation forces the indium to be extracted as more lithium is inserted into the antimony matrix according to Eq. 1.2.¹⁸



The final charge stage is reached when $x = 1$ and Li_3Sb is obtained. While the theoretical gravimetric capacity of InSb (349.6 mAh g^{-1}) is only half of elemental antimony capacity (679.2 mAh g^{-1}), the corresponding volume expansion is 7x smaller than the volume change of pure antimony.¹⁸ The small 7% volume change that occurs during the lithiation of InSb should make the capacity lost during cycling unnoticeable, but after only 20 cycles the capacity has already dropped to 30% of the theoretical value.¹⁸

The reversible process that provides 70% of the capacity to be maintained after 20 cycles is the process shown in Eq. 1.2.¹⁹ Besides indium being expensive and not environmentally friendly, the extruded indium that does not get re-incorporated back into the antimony matrix forms whiskers after numerous cycles which have the ability to short-circuit the cell.¹⁹⁻²⁰ The problems found with InSb did not eliminate the interest in

intermetallic materials as alternative anode materials. The poor cycle performance of InSb was determined to be due to the irreversibility of the first lithiation (Eq. 1.3), which was determined using EXAFS experiments that showed not all of the indium was reinserted during the delithiation.¹⁹



Following the work done with InSb, the lithiation of Cu₂Sb was investigated. Copper antimonide is interesting for several reasons: (1) the capacity is similar to graphite's (323 mAh g⁻¹), (2) the lithiation potential is 500 mV more positive than graphite, (3) the antimony is in a similar fcc array found in InSb, (4) compared to indium, copper is a cheap abundant material which does react with lithium and (5) upon extraction from the antimony matrix the copper should also help with electrical conduction. During cycling, the antimony atoms act as a matrix in which the lithium/copper exchange takes place. As shown in the schematic in Figure 1.1, the antimony array only has to expand and contract to allow the exchange of lithium and copper. The overall volume change of 65% during the lithiation of Cu₂Sb is not significantly larger than InSb overall volume expansion of 47%.²⁰ This relatively small volume change experienced by Cu₂Sb is responsible for the excellent cycle performance which was first demonstrated by Fransson *et al.* who reported that 90% of the theoretical capacity was retained after 25 cycles.²⁰

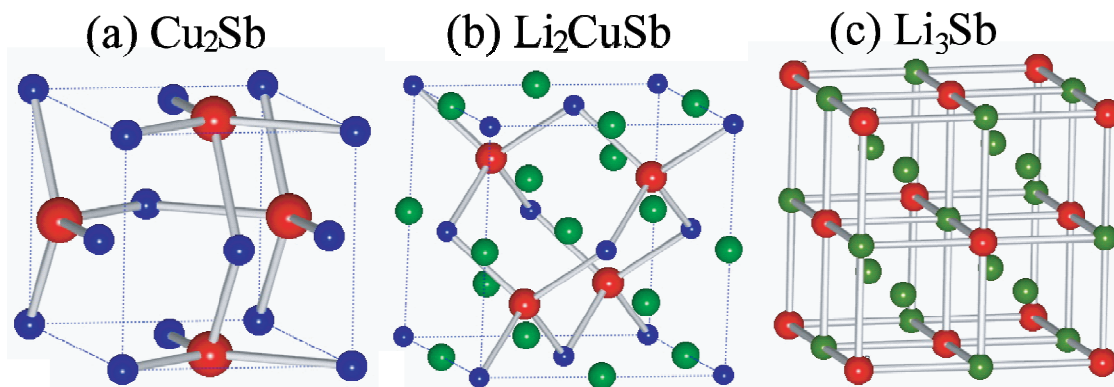


Figure 1.5: Crystal structure of (a) Cu_2Sb , (b) Li_2CuSb and (c) Li_3Sb created using CrystalMaker[®]. The red spheres are antimony atoms the blue spheres are copper atoms and the green spheres are lithium.

The different phases that are encountered during the lithiation of Cu_2Sb have been investigated using X-ray diffraction (XRD) which show that the lithiation occurs in a series of steps similar to the lithiation of InSb .²⁰ During the first lithiation shown in Figure 1.2, there is a small amount of charge measured above 900 mV vs. Li/Li^+ corresponding to the formation of an SEI layer. The first plateau corresponding to the lithiation of Cu_2Sb is at 800 mV vs. Li/Li^+ and from the XRD results was determined to correspond to Eq. 1.4.²⁰



A solid solution is formed during this first plateau following Eq. 1.4 until $x = 2$ and $y = 1$ at which point Li_2CuSb is formed indicated by XRD.²⁰ After a slight drop in potential a second plateau at 600 mV vs. Li/Li^+ corresponding to the second lithiation step as describe in Eq. 1.5 is obtained.



Unlike the indium in the InSb case the extruded copper does not react with lithium, so after the plateau at 600 mV vs. Li/Li^+ the voltage quickly drops to zero (Figure 1.2).

Upon switching the polarity and delithiating the material two plateaus are observed corresponding to the reverse of Eq. 1.4 and Eq. 1.5.²⁰ There is a slight over potential needed during the delithiation; that is the two plateaus observed on the discharge are c.a. 300 mV more positive then the corresponding charge plateaus (Figure 1.2). The charge and discharge of electrodeposited copper antimonide shown in Figure 1.2 was performed with a current of $1.58 \times 10^{-6} \text{ A cm}^{-2}$ to insure thermodynamic phases were reached and permitted Cu_2Sb to be reformed after one complete cycle.²⁰

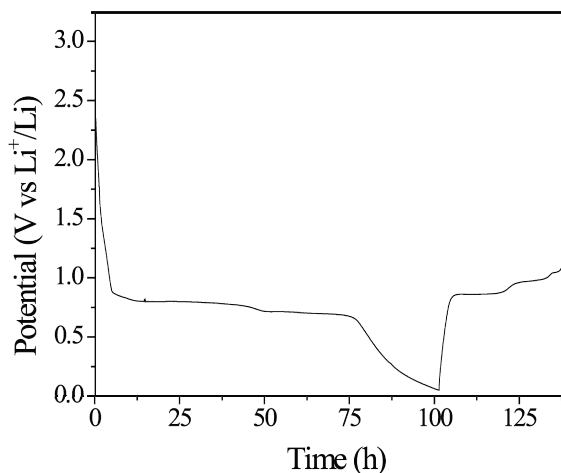


Figure 1.6: Charge and discharge curve of a half cell containing electrodeposited Cu_2Sb film and lithium metal. The electrolyte was composed of 1 M LiClO_4 in ethylene carbonate, dimethylene carbonate, and dimethylene carbonate (1:1:1 by vol.). The half cell was cycled at $1.58 \times 10^{-6} \text{ A cm}^{-2}$.

As mentioned before, Fransson *et al.* also demonstrated that 90% of the theoretical capacity of Cu_2Sb was retained after 25 cycles.²¹ The Cu_2Sb used in this investigation was synthesized by ball milling copper and antimony powder together, and as evidenced from the first lithiation there was a considerable amount of oxide present causing some of the irreversible capacity loss.²¹ Since this report other synthesis techniques have been used to synthesize Cu_2Sb . In one solution-based route Cu_2Sb is precipitated from the solution according to Eq. 1.6.²²



The lithiation of the precipitated product before and after annealing was investigated in a binder matrix against lithium metal.²¹ The delithiation profile of the annealed Cu_2Sb synthesized with this route had two extra plateaus; the first at 200 and the second at 1100 mV vs. Li/Li^+ .²¹ These plateaus are most likely from impurities encountered during synthesis. The capacity retention of the Cu_2Sb synthesized according to Eq. 1.6 was only 26.3% of the theoretical specific capacity.²¹ This was improved to 72.8% by annealing, but still was found to be considerably less than found for the ball milled samples.²⁰⁻²¹ The cycle performance of Cu_2Sb synthesized with two different reductive solution routes, in which it was clear from XRD that Sb_2O_3 was present, was also found to be poor.²³⁻²⁴ In one case only 57.2% of the theoretical capacity was present after 15 cycles, and in the second case 61.9% of the theoretical capacity was retained after 50 cycles.²³⁻²⁴ The battery testing in these examples was performed on Cu_2Sb particles dispersed within a binder. The binder is usually made with 80% active material (Cu_2Sb), 10% graphite and 10% (PVDF).^{20,22-27} There is one example in the literature where no binder was used to perform cycling studies of Cu_2Sb thin films that were pulsed laser deposited.²⁷ In this case the potential that the Cu_2Sb was charged to was found to play an important role in the capacity retention of the material.²⁷ Cycling between 1200 and 0 mV vs. Li/Li^+ , 61.9% of the theoretical capacity was retained after 50 cycles, but only 31.0% of the theoretical capacity was retained after 50 cycles when cycling between 1400 and 650 mV vs. Li/Li^+ .²⁷ Two theories have arisen to explain the discrepancies in capacity retention based on the reversibility of the first lithiation step represented in Eq. 1.4.

Matsuno *et al.* reported in 2007 using oxide free polycrystalline Cu_2Sb that Eq. 1.4 was irreversible and Cu_2Sb is not reformed upon the delithiation.²⁸ The absence of oxide meant that during the first lithiation no charge was encountered until the potential reached 800 mV vs. Li/Li^+ (which corresponds to the first lithiation step).²⁸ Upon delithiation only 280 mAh g^{-1} was recovered which is only 86.7% of the theoretical capacity, which they claim is evidence that only $\text{Li}_{1.6}\text{CuSb}$ can be reached.²⁸ From in-situ thermal analysis and density functional theory (DFT) study of the phase stability of the ternary phase diagram for Li-Cu-Sb they claim that the change from a cubic Li_xCuSb back to a tetragonal Cu_2Sb requires too much energy.²⁸⁻³⁰ At the same time this report came out Morcrette *et al.* performed a lithiation study of two types of Cu_2Sb in binder, and found similar results for the reversibility of Eq. 1.4 at normal cycle rates.²⁶ If the cycle rate was slow, or thermal energy was added to the system, Cu_2Sb could be obtained after a full cycle demonstrating thermodynamically Eq. 1.4 is reversible.²⁶ Work performed in our lab discussed in Chapter 8 demonstrates that the reversibility of Eq. 1.4 is kinetically controlled and not thermodynamically controlled.

1.5 Current Synthesis routes for battery materials

As mentioned in the previous section most of the battery testing on copper antimonide in the literature was performed with samples prepared by ball milling copper and antimony powders.^{20,23,26} Three solution route syntheses for Cu_2Sb have been found in the literature, all using a reducing agent to reduce the dissolved salts of copper and antimony.^{22,24,31-32} The reductions involved in the first two methods are time consuming, the shortest requiring 1.5 hours of refluxing.³² The solution method reported by Sarakonsri *et al.* required annealing under argon, after stirring the solution for one day.²²

The solution synthesis reported by Ren *et al.* is the least energy and time intensive synthesis found in the literature.²⁴ In this synthesis sodium citrate is used as a complexing agent and potassium borohydride is used to reduce Cu²⁺ and Sb³⁺ at pH 12 in what the authors describe as a “violent reduction reaction”.²⁴ The copper antimonide synthesized from both the ball mill and solution techniques are plagued with impurities, mainly antimony and copper oxides.^{20,22-24,26,31} Oxide impurities are problematic for battery testing since lithium reacts with oxide according to Eq. 1.7 irreversibly adding to the capacity loss during the first cycle.³³



Polycrystalline Cu₂Sb with no significant amounts of oxides has been synthesized using: thermal evaporation, growing crystals from melts, electron beam evaporation and pulse laser deposition.^{28-30,34-37} These types of techniques generally involve high temperatures, high vacuum, expensive equipment not capable of scaling up, and/or long synthesis times. Such requirements increases the cost of the synthesis in terms of energy needed and could be troublesome in obtaining the correct stoichiometry given that antimony has a much higher vapor pressure than copper. A commonality to all the syntheses mentioned in this section is the difficulty of scaling up the synthesis technique for commercial applications.

Another shortcoming of the techniques motioned above is that to perform battery testing in all but one case the synthesized Cu₂Sb is added to a binder. This adds complexity to the characterization of copper antimonide during the cycling procedure. The paper by Song *et al.* was the only example mentioned that no binder was added for battery testing, but insufficient characterization was performed to exploit the absence of

the binder.²⁷ The objective of this research is to use electrodeposition as a synthesis route to deposit Cu₂Sb thin films and nanowire arrays directly onto a current collector, so battery testing can be performed without a binder. The nanowire arrays should also have improved capacity retention and charge and discharge rates as discussed in the next chapter.

1.6 References

- (1) Flandrois, S.; Simon, B. *Carbon* **1999**, *37*, 165.
- (2) Long, J. W.; Dunn, B.; Rolison, D. R.; White, H. S. *Chemical Reviews* **2004**, *104*, 4463.
- (3) Winter, M.; Besenhard, J. O. *Electrochim Acta* **1999**, *45*, 31.
- (4) Bard, A. J.; Faulkner, L. R. *Electrochemical methods: fundamentals and applications*; 2 ed.; Wiley: New York, 2001.
- (5) Li, N. C.; Martin, C. R.; Scrosati, B. *Electrochemical and Solid State Letters* **2000**, *3*, 316.
- (6) Li, N. C.; Martin, C. R. *Journal of the Electrochemical Society* **2001**, *148*, A164.
- (7) Li, N. C.; Martin, C. R.; Scrosati, B. *Journal of Power Sources* **2001**, *97-8*, 240.
- (8) Patrissi, C. J.; Martin, C. R. *Journal of the Electrochemical Society* **2001**, *148*, A1247.
- (9) Sides, C. R.; Li, N. C.; Patrissi, C. J.; Scrosati, B.; Martin, C. R. *Mrs Bulletin* **2002**, *27*, 604.
- (10) Sides, C. R.; Martin, C. R. *Advanced Materials* **2005**, *17*, 125.
- (11) Ruffo, R.; Hong, S. S.; Chan, C. K.; Huggins, R. A.; Cui, Y. *The Journal of Physical Chemistry C* **2009**, *113*, 11390.
- (12) Park, M.-H.; Kim, M. G.; Joo, J.; Kim, K.; Kim, J.; Ahn, S.; Cui, Y.; Cho, J. *Nano Letters* **2009**, *9*, 3844.
- (13) Cui, L.-F.; Yang, Y.; Hsu, C.-M.; Cui, Y. *Nano Letters* **2009**, *9*, 3370.
- (14) Chan, C. K.; Ruffo, R.; Hong, S. S.; Huggins, R. A.; Cui, Y. *Journal of Power Sources* **2009**, *189*, 34.
- (15) Zhang, S. S. *Journal of Power Sources* **2006**, *162*, 1379.
- (16) Fujimoto, M.; Kida, Y.; Nohma, T.; Takahashi, M.; Nishio, K.; Saito, T. *Journal of Power Sources* **1996**, *63*, 127.
- (17) Besenhard, J. O.; Yang, J.; Winter, M. *Journal of Power Sources* **1997**, *68*, 87.
- (18) Vaughey, J. T.; O'Hara, J.; Thackeray, M. M. *Electrochemical and Solid-State Letters* **2000**, *3*, 13.
- (19) Kropf, A. J.; Tostmann, H.; Johnson, C. S.; Vaughey, J. T.; Thackeray, M. M. *Electrochemistry Communications* **2001**, *3*, 244.
- (20) Fransson, L. M. L.; Vaughey, J. T.; Benedek, R.; Edstrom, K.; Thomas, J. O.; Thackeray, M. M. *Electrochemistry Communications* **2001**, *3*, 317.
- (21) [Anon] *Mer-Mar Eng Rev* **1997**, 31.

- (22) Sarakonsri, I.; Johnson, C. S.; Hackney, S. A.; Thackeray, M. M. *Journal of Power Sources* **2006**, *153*, 319.
- (23) Zhang, G.; Huang, K. L.; Liu, S. Q.; Zhang, W.; Gong, B. L. *Journal of Alloys and Compounds* **2006**, *426*, 432.
- (24) Ren, J. G.; He, X. M.; Pu, W. H.; Jiang, C. Y.; Wan, C. R. *Electrochim Acta* **2006**, *52*, 1538.
- (25) Bryngelsson, H.; Eskhult, J.; Nyholm, L.; Edström, K. *Electrochim Acta* **2008**, *53*, 7226.
- (26) Morcrette, M.; Larcher, D.; Tarascon, J. M.; Edstrom, K.; Vaughey, J. T.; Thackeray, M. M. *Electrochim Acta* **2007**, *52*, 5339.
- (27) Song, S. W.; Reade, R. P.; Cairns, E. J.; Vaughey, J. T.; Thackeray, M. M.; Striebel, K. A. *Journal of the Electrochemical Society* **2004**, *151*, A1012.
- (28) Matsuno, S.; Noji, M.; Kashiwagi, T.; Nakayama, M.; Wakihara, M. *J. Phys. Chem. C* **2007**, *111*, 7548.
- (29) Masanobu, N.; Shinsuke, M.; Junichi, S.; Masataka, W. *Journal of The Electrochemical Society* **2008**, *155*, A505.
- (30) Shinsuke, M.; Makiko, N.; Masanobu, N.; Masataka, W.; Yo, K.; Hajime, M. *Journal of The Electrochemical Society* **2008**, *155*, A151.
- (31) Sarakonsri, T.; Apirattanawan, T.; Tungprasurt, S.; Tunkasiri, T. *J Mater Sci* **2006**, *41*, 4749.
- (32) Kulifay, S. M. *J Am Chem Soc* **1961**, *83*, 4916.
- (33) Li, J.-T.; Maurice, V.; Swiatowska-Mrowiecka, J.; Seyeux, A.; Zanna, S.; Klein, L.; Sun, S.-G.; Marcus, P. *Electrochim Acta* **2009**, *54*, 3700.
- (34) Pearson, W. B. *Can J Phys* **1964**, *42*, 519.
- (35) Ball, E. J. *Journal of the Chemical Society, Transactions* **1888**, *53*, 167.
- (36) Halimi, R.; Merabet, A. *Surf Sci* **1989**, *223*, 599.
- (37) Isshiki, T. N., K.; Sakamoto, T.; Uyesugi, K.; Saijo, H.; Shiojiri, M. *Physica Status Solidi A: Applied Research* **1993**, *139*, 421.

CHAPTER 2

ELECTRODEPOSITION OF Cu_2Sb NANOWIRE ARRAYS

2.1 Benefits of using electrodeposition as a synthesis route

As covered in the previous chapter the common synthesis techniques for copper antimonide are solid-state techniques that are energy intensive.¹⁻¹¹ The solution syntheses reported for Cu_2Sb are less energy intensive, but the products usually contain high number of impurities, especially oxides.¹²⁻¹⁵ There are two major drawbacks to all of these synthesis techniques. The first is they require high energy input, which would cause the commercial fabrication of Cu_2Sb to be expensive. The second drawback is these synthesis techniques require the material to be dispersed into a binder in order to make electrical connection to a current collector. There are two consequences from this: 1) the binder adds non-active weight to the battery, decreasing the capacity of a battery, and 2) the binder makes characterization of the Cu_2Sb during the charge and discharge difficult. This is because the Cu_2Sb has to be analyzed or removed from a matrix made up from the binder, which hinders X-ray diffraction (XRD), X-ray photoelectron spectroscopy (XPS), scanning electron microscopy (SEM), transmission electron microscopy (TEM) and energy dispersive spectroscopy (EDS). The binder also contributes mechanical stability to the Cu_2Sb hiding some of the physical processes that contribute to the degradation of the material during the charge and discharge. This makes it more difficult to design new materials and/or morphologies that address the process responsible for the degradation and thus the capacity loss that is experienced during cycling. Because of these shortcomings we chose to pursue a new synthesis route that allows Cu_2Sb to be directly deposited onto the current collector in a low cost manner.

Electrodeposition is becoming a popular alternative for synthesizing materials for electronic, energy conversion and energy storage applications that are usually by

synthesized with solid-state techniques making the devices extremely expensive. Unlike most solid state synthesis routes, electrodeposition can usually be performed at moderate conditions and from common solutions. Three other strengths of electrodeposition are: (1) it allows precise control of composition and crystallinity,¹⁷⁻¹⁹ (2) it provides the ability to deposit on complex shapes,²⁰⁻²² and (3) it can deposit materials with nanoscale dimensions.^{20,23-27} All three of these strengths make electrodeposition a powerful synthetic tool for anode materials, especially Cu_2Sb . As discussed in the first chapter, the small volume change that is responsible for the improvement in cycle performance, compared to elemental antimony, is from the crystal structure of Cu_2Sb , so control of the composition and crystallinity is extremely important. Electrodeposition also has the ability to deposit Cu_2Sb directly onto the current collector that is used for the battery testing and application without the addition of binder. While this improves the characterization of Cu_2Sb and lowers the weight of non-active materials within a battery, it also allows Cu_2Sb to be deposited onto current collectors with different sizes, shapes, and surface areas. High surface area improves the kinetics involved in the solid state transformations, and decreases the mechanical degradation that occurs during the lithiation and delithiation of battery materials.²⁹⁻³⁴

The improvement in battery performance materials with high surface area has made lithium-ion batteries one of the fields that have been dramatically affected by the emergence of nano-scale materials. Electrodeposition can be used to make nano-scaled materials using both top-down and bottom-up approaches.^{23,26-28,35-40} The electrodeposition of nano-scaled materials using the bottom-up approach relies on the precise control over the current and voltage in order to control the rate of nucleation and

growth of nanoparticles on different surfaces.^{28,37,39-43} Some examples from the literature are shown in Figure 2.1. Using modified surfaces, or surfaces with certain features such as steps that change the way deposits nucleate on the substrate, is another way bottom-up electrodeposition of nano-scale materials is achieved.⁴⁴ The top-down electrodeposition approaches to nano-scale synthesis use templates attached to substrates to direct the shape and size of the deposited material.^{23-25,45-47} Examples of nanoscale materials electrodeposited using top-down approach can be seen in Chapters 6 and 9 of this thesis.

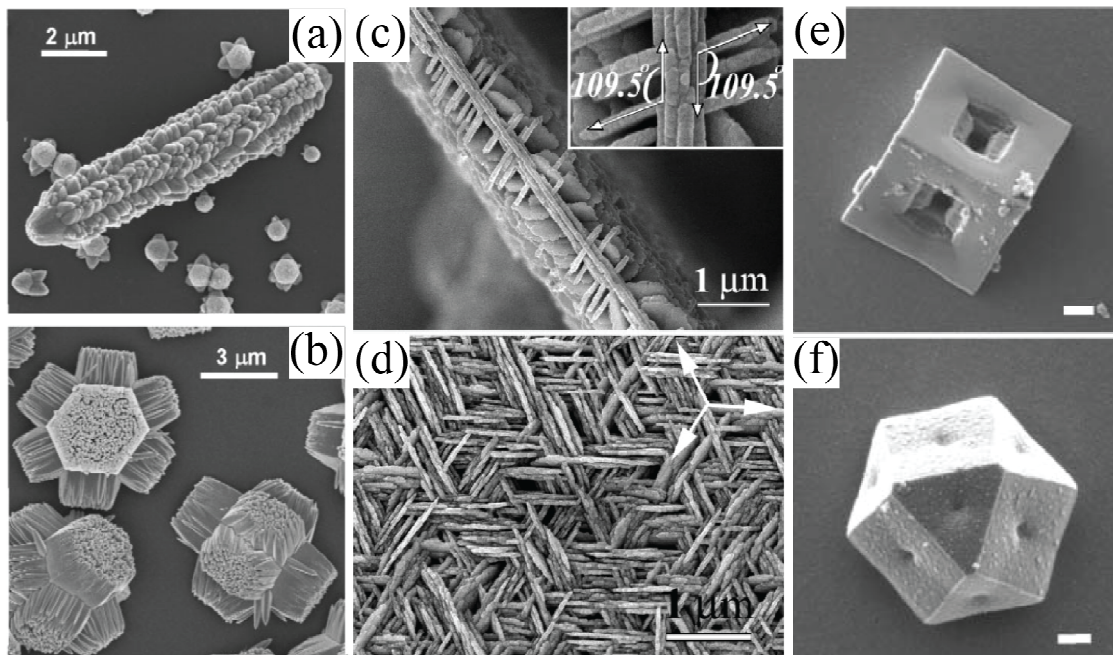


Figure 2.1: Examples from the literature of nanoscale materials electrodeposited without templates via bottom-up techniques. **(a)** Electrodeposited ZnO crystals **(b)** dense arrays of ZnO nanorods adopted from Sounart *et al.*¹⁶ **(c)** Side view, **(d)** top view of silver electrodeposited nanoarachidecture adopted from Zhu *et al.*²⁸ Cu₂O crystals electrodeposited with morphology control leading to **(e)** cubes and **(f)** tetradecagons, among other shapes. The scale bar in **(e)** and **(f)** is 1 μm the images were adopted from Choi *et al.*⁴⁰

While various types of templates have been implemented in the electrodeposition of materials, the most common templates used to make nano-scale battery materials are porous aluminum oxide (AAO) and track-etch polycarbonate (TEP) templates.³²⁻³³ By

placing a current collector on the back of an insulating AAO or TEP template, the electrodeposition occurs at the bottom of the pores where the current collector is exposed. As the deposition proceeds, arrays of particles, wires and rods are grown with diameters that range from 40 to 500 nm and lengths that range from 50 to 5000 nm.^{31-34,48} After the deposition is complete, the templates can be removed chemically, leaving behind arrays of particles, wires and rods. The diameters of the wires or rods are controlled by the pore diameter of the template while the length of the wires and rods is controlled by the duration of the electrodeposition.

2.2 The improvements in properties expected from arrays of Cu₂Sb nanowires

Martin *et al.* demonstrated for the first time in 1997 that nanotube morphology formed out of porous alumina templates improved the capacity retention and rate capabilities of LiMn₂O₄ during cycling.⁴⁹ This stimulated an enormous amount of work using “template synthesis” as a means of synthesizing nano-tubes, -wires, and -rods of cathode materials in order to elevate concentration polarization and slow diffusion rates caused by solid state lithium-ion diffusion.⁵⁰ It was found that the lack of concentration polarization in the nanotubes of a cathode material allowed the capacity to be an order of magnitude higher than for large particles of the same material in which not all of the material was able to be lithiated.⁴⁹⁻⁵⁰ The rate capabilities of the material were improved simply due to the shorter distance the lithium-ions had to travel in the material during a charge or discharge.⁴⁹⁻⁵⁰ It was also discovered that the capacity loss experienced during cycling was considerably less when nano-tube morphology was used, because the nano-scale dimensions keeps the absolute volume change small which reduces the mechanical strain caused by the volume change.⁴⁹⁻⁵¹

Soon after successful improvement in the capacity and rate performance of cathode materials was found using nano-tubes,-wires, and -rods the same strategy was implemented for anode materials. The first anode material to be grown in AAO templates and cycled was SnO₂ by Li *et al.*³¹⁻³² Nanowires with a diameter of 110 nm and a packing density of 5×10^8 nanowires cm⁻² exhibited an capacity increase with cycle numbers over 700 mAh g⁻¹ at a rate of 8C.³¹ The lack of degradation in the nanowire SnO₂ arrays was demonstrated after a capacity of 550 mAh g⁻¹ was maintained after 1400 cycles at a rate of 58C. This is a serious improvement over the fast pulverization thin film electrodes of SnO₂ which pulverize after a few dozen cycles.³² These results have also led to intense research on nano-wires, -rods, and -tubes of different anode materials with a variety of results.⁵²⁻⁶¹ In the examples given thus far of template grown cathode and anode materials, the synthesis techniques used to grow the material in the template has not been electrodeposition, but other solution or solid-state techniques. There are two examples in the literature where tin was electrodeposited within a template with the resulting rods and wires showing improved cycle stability even after 150 cycles.⁶²⁻⁶³

These examples from literature demonstrate that nanowires of electrode material grown using templates can improve the capacity, stability, and rate performance of the material. The literature presented in Chapter 1 provided evidence that the similarity of the crystal structures of Cu₂Sb and its lithiated product (Li₃Sb) also improves the cycle performance of the material. The goal of this research project is to combine the progress made in these two areas of the literature by fabricating Cu₂Sb nanowires in order to fabricate anode materials with superior lithium-ion battery performance. As mentioned

in Chapter 1 one of the causes of the irreversible capacity loss is slow kinetics between the Li_2CuSb and the Cu_2Sb phases. While nanowires of Cu_2Sb should benefit from the same properties mentioned for the SnO_2 nanowires, the small dimensions of the wires should also help with the slow kinetics between these two phases, thus increasing the reversible capacity of the material. SEM and TEM will be used to see how the Cu_2Sb wires with nanoscale dimensions in two directions are affected by the volume change. After the improvements of using a nanowire arrays Cu_2Sb electrode are tested, the wires will be implemented into a 3D solid-state battery that takes advantage of the nanoscale morphology of the nanowire array.

One of the benefits of nanowire electrode materials for lithium-ion batteries is the short distance that lithium ions have to diffuse within the material to obtain the necessary phase. This short diffusion distance increases the rate at which lithium ions can be removed from the material and decreases concentration polarization. In common lithium-ion batteries the two solid electrodes are separated by a liquid electrolyte, in which the lithium-ion diffusion is relatively fast. The slow diffusion within the electrode material is what limits the power available from a cell and thus electrode materials with nanoscale dimensions greatly improve the rate performance of a lithium-ion cell. Unfortunately, because of the need for electrochemical stability at negative potentials (c.a. 3000 mV vs. SHE) the electrolyte used in state-of-the-art lithium-ion batteries is based on carbonates and thus highly flammable. This safety issue was brought to the public's attention after a series of laptop fires prompted the recall of 4 million laptop batteries in 2006, the largest battery recall in the history of the electronic industry.⁶⁴ For HPEV and PEV this safety concern is much more serious considering the rough treatment vehicles routinely

encounter. For this reason an interest in solid-state lithium-ion batteries has developed. The major-short coming of an all-solid-state battery is the slow solid-state diffusion, which in conventional batteries only happens in the electrode materials, now becomes a problem in the solid electrolyte. Thus, the conventional thin film battery geometry where the anode and cathode are separated by a couple microns of electrolyte will lead to very poor power capability from the slow diffusion through a solid-electrolyte.

We are in the process of fabricating a 3D nanoscale battery based on nanowire arrays of Cu_2Sb . The geometry of such a battery elegantly addresses the slow solid-state-diffusion which is problematic for all solid-state batteries. Figure 2.1 is a schematic showing a magnified image of what the 3D nanoscale battery based on Cu_2Sb nanowire arrays would look like. In Figure 2.1 the nanowire array of Cu_2Sb is represented as grey wires (40 nm diameter) which are surrounded by the solid electrolyte (20 nm thick) shown in gold. The cathode material in the 3D nanowire array battery is integrated on top of the nanowires after the electrolyte has been formed using a method that allows the empty spaces (40 nm) between the wires to be filled. Looking at Figure 2.1 the improvement in diffusion from the geometry becomes evident as the lithium-ion diffusion path is much shorter than in a thin film configuration. The longest diffusion path in a battery based on the geometry shown in Figure 2.1 is from the center of a nanowire to the center of the empty space (cathode material). For example, with the wires density and pore size represented in Figure 2.1 the diffusion path length would be 60 nm which is only 6% of the path length in a thin film configuration.

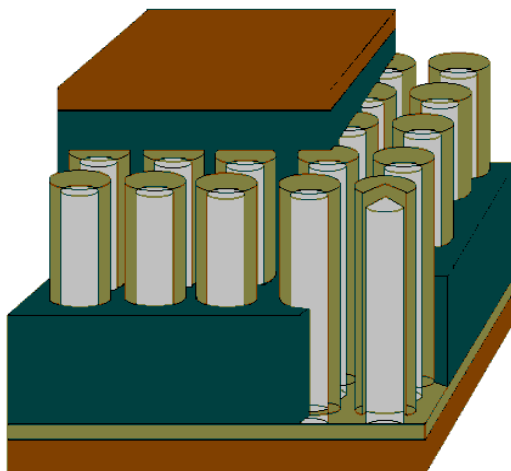


Figure 2.2: A schematic of a 3D nanoscale battery based on nanowire array of Cu_2Sb . The nanowire array of Cu_2Sb is represented in gray. The solid electrolyte surrounding the nanowire array is represented in gold, and the cathode material is represented in green. The current collectors are shown in brown. The wire diameter can range between 40 to 100 nm. The optimal electrolyte thickness would be less than 50 nm, and the amount of cathode added would be based on balancing the capacity of the Cu_2Sb nanowires.

While the idea of a 3D nanoscale battery has been around for some time, no successful fabrication method has been reported.⁶⁵ With this in mind we propose using electrodeposition to fabricate nanowire arrays of Cu_2Sb within alumina templates. After the nanowire array has been grown in the AAO template, the template is removed using either an acid or base leaving ideally a forest of Cu_2Sb nanowires, as shown schematically in Figure 2.2a. Then a solid electrolyte will be formed onto the wires of the array in a uniform, thin, conformal manner (as shown in Figure 2.2b). This step will be achieved either using solution-based electrochemical or self-limiting techniques. The nanoscale cathode material will then be drop-cast into the void space left behind after the formation of the solid electrolyte providing the complete solid-state 3D nanoscale battery represented in Figure 2.1. It has been calculated using the proposed geometry that energy densities (1538 Wh l^{-1}) and power densities ($3.86 \times 10^8 \text{ W l}^{-1}$) can be achieved, which are

orders of magnitude higher than conventional lithium-ion batteries. Not only does this fabrication procedure provide the means to fabrication a 3D nanoscale battery proposed by Long *et al.*, but each step of the fabrication is low-temperature solution-based, making the cost of fabrication economically superior to state-of-the-art techniques current used to fabricate thin film lithium-ion batteries.⁶⁵ The first step of this fabrication process and the focus of the research presented in this thesis is the electrodeposition of nanowire arrays of Cu_2Sb (Figure 2.2a).

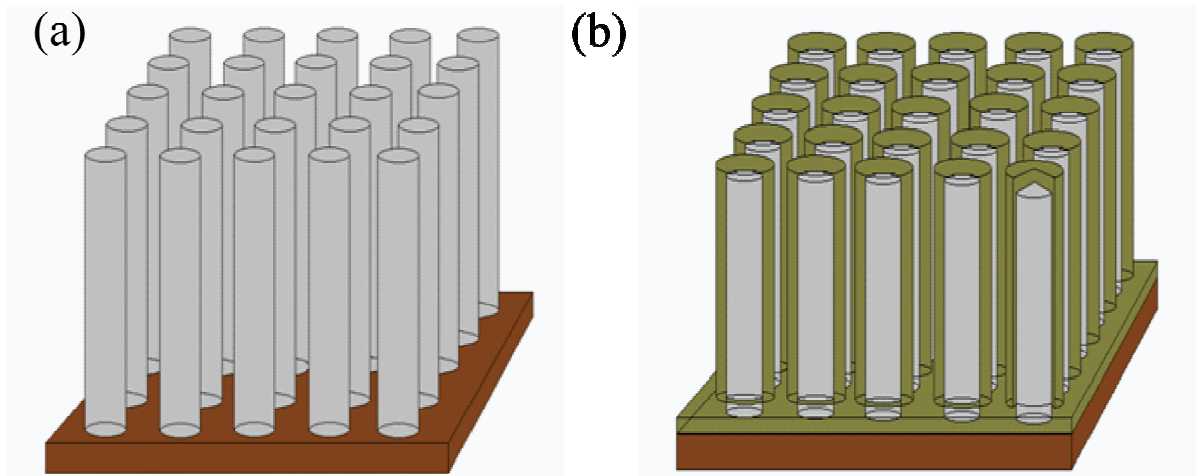


Figure 2.3: Schematics of (a) the Cu_2Sb nanowire array (grey) on a copper substrate (brown) after the AAO template has been removed, and (b) after the wires are coated with a solid electrolyte (green).

2.3 Using AAO templates to grow arrays of Cu_2Sb nanowires

Porous anodic alumina templates were chosen for the electrodeposition of Cu_2Sb nanowire arrays over track-etch polycarbonate templates for the following reasons: (1) AAO preparation does not require the special instrumentation that TEP does, (2) the pores in AAO templates are highly ordered and dense (7×10^{10} pores cm^{-2}), (3) the pore diameter of AAO templates is adjustable from 7 to 300 nm and is uniform for the entire length of the pore, and (4) after the wires are grown the template can be dissolved away

in acidic or basic medium.⁶⁶ Not only do TEP templates require special instrumentation to fabricate the pores, but the pores are usually cone shaped instead of cylinder shaped. Alumina templates are formed by anodizing aluminum metal in an acid, and require only a power supply. Some of the typical acids used are: 15% sulfuric acid, 3% oxalic acid, 5% chromic acid and 5% phosphoric acid.⁶⁷ A DC voltage is applied across the aluminum foil anode and the platinum mesh cathode, causing the formation of an aluminum oxide on the surface of the aluminum foil according to Eq. 2.1.⁶⁷



The oxygen layer is simultaneously dissolved by hydrogen ions on small periodically spaced locations driven by the applied electronic field according to Eq. 2.2.⁶⁷



The pore size can be controlled by changing the balance of these two reactions by manipulating the type of acid used, anodization voltage, and temperature. A hexagonal periodicity is formed on smooth aluminum foils from the equilibrium of Eq. 2.1 and 2.2. The space between the pores and the pore order can also be controlled by physical indentation and masking of the aluminum foil, allowing templates to be customized with a variety of pore densities and arrangements.⁶⁸

Once the AAO template has been made there are two routes which can be used to turn the AAO template into a working electrode for electrodeposition. The first route is to use strongly basic KOH to dissolve the barrier layer allowing the aluminum metal at the bottom of the pore to be used as a substrate.⁶⁶ The second route is to evaporate a metal substrate onto the top of the formed AAO template, then “dissolve” the remaining aluminum foil using HgCl_2 according to Eq. 2.3.⁶⁶



After the completion of Eq. 2.3 the barrier layer is then removed using strongly basic KOH solutions. Once the AAO template is turned into a working electrode following the procedures just discussed, the electrode is placed into a three electrode cell and wires are grown by applying a current between this working electrode and a counter electrode. The third electrode is a reference electrode and allows the potential of the working electrode to be measured and/or controlled during the deposition.

2.4 Complications that arise during the electrodeposition of intermetallic materials

The procedure outlined above has been used to deposit nanowire arrays of a variety of materials for a variety of applications.^{42,44,69-73} This fabrication technique for nanowire arrays of materials is relatively simple if the electrodeposition procedure for the material of interest has been developed, because the only thing that needs to be changed is the AAO electrode is used as the substrate instead of a thin conducting film. For most single element materials the electrodeposition procedure is known, but the electrodeposition of multi-element materials tends to be difficult. The difficulty arises from the required simultaneous control of the deposition rates and potentials for the elements that is needed to obtain the material of interest.^{23-24,66,74-76}

The deposition rate depends on many factors and varies differently for each element. The main factors that affect the deposition rates are: (1) potential, (2) temperature, (3) concentration, (4) pH, and (5) current efficiencies.²⁴ The potential control over the deposition rate is based on the Nernst equation and the standard redox potential (E^0) for the deposition of each element. The Nernst equation only allows the concentration to affect the deposition potential by $59/n$ mV per decade change in

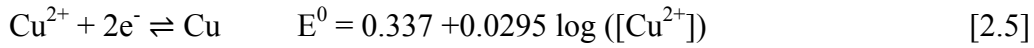
concentration (where n is the number of electrons).⁷⁷ A common means of controlling the deposition potentials for alloy electrodeposition is the use of complexing agents, which provide a larger control over the deposition potential according to Eq 2.4.⁷⁷

$$E_{\text{rev}} = E^0 + \frac{2.3RT}{nF} \log(K) + \frac{2.3RT}{nF} \log(C_{\text{Me}}) \quad [2.4]$$

The K is the stability constant of the complex, C_{Me} is the bulk concentration of the metal in solution, T is the temperature, R is the gas constant and F is Faraday's constant. The difference in the E^0 of the desired elements can vary over 1 V, and thus to achieve control of the deposition rate for each element it is sometimes required to perform a layer by layer electrodeposition of each element at different potentials. Alloy electrodeposition only requires the relative amounts of the elements present in the desired material to be controlled. An extra complexity in the electrodeposition of intermetallic or semiconductor materials is electrodeposition must lead to the appropriate crystal structure for the desired properties to be obtained. Thus, the layers from the electrodeposition are usually post-annealed in order to obtain the desired material.

As the goal of this research is to electrodeposit Cu_2Sb nanowire arrays, all the difficulties presented for the electrodeposition of multi-element materials will have to be taken into account. As mentioned in Chapter 1 the crystal structure of Cu_2Sb has an important role in reducing the volume change during the lithiation and delithiation and thus not only does the electrodeposited Cu_2Sb need to have a 2 to 1 atomic ratio of copper to antimony, but it needs to have the correct crystal structure. The electrodeposition of copper is one of the most studied electrodeposition metal with a vast amount of electrolytes and additives to choose from in the literature.^{22,25-26,35-36,40,44,63,71,78-}

⁹⁰ The standard E^0 for the reduction of Cu^{2+} from aqueous solution below pH 6 comes from Eq. 2.5.⁹¹



When the pH of the solution is above 6 then copper oxides are formed at potentials negative of 300 mV vs. SHE.⁹¹ The copper oxide formed from solutions with these pH values usually passivates the surface of the electrode and inhibits the deposition of copper metal.

The electrodeposition of antimony is much less well known but has been performed from organic solutions and aqueous solutions containing complexing agents.^{47,92-93} The complexing agents used in the electrodeposition of antimony and antimony alloys reported in the literature are used to keep Sb^{3+} in solution because antimony oxide precipitates out from solutions that are not highly acidic.^{24,74-75,94} The solubility can be quantified by Eq. 2.6.⁹¹



Without a complexing agent Eq. 2.6 shows that from a pH of 1 to 3 there is only 8.91×10^{-5} M to 8.91×10^{-7} M SbO^+ respectively, available for the deposition of antimony metal according to Eq. 2.7 and 2.8.⁹¹



Putting Eq. 2.6, 2.7 and 2.8 together the reduction potential for antimony from solutions with a pH range from 1-3 is 90 to -30 mV vs. SHE. According to Eq. 2.5 for the reduction potentials of Cu^{2+} and Sb^{3+} to be similar the concentration of Cu^{2+} would have to be less than 1×10^{-8} M at a pH of 1 and 1×10^{-12} M at a pH 3. This would make

depositing Cu₂Sb film of usable thicknesses extremely difficult if not impossible, thus like others, we chose to investigate the electrochemistry of antimony complexes in the presence of copper in order to develop a single potential deposition of Cu₂Sb.

2.5 References

- (1) Ball, E. J. *Journal of the Chemical Society, Transactions* **1888**, 53, 167.
- (2) Bryngelsson, H.; Eskhult, J.; Nyholm, L.; Edström, K. *Electrochim Acta* **2008**, 53, 7226.
- (3) Fransson, L. M. L.; Vaughey, J. T.; Benedek, R.; Edstrom, K.; Thomas, J. O.; Thackeray, M. M. *Electrochemistry Communications* **2001**, 3, 317.
- (4) Isshiki, T. N., K.; Sakamoto, T.; Uyesugi, K.; Saijo, H.; Shiojiri, M. *Physica Status Solidi A: Applied Research* **1993**, 139, 421.
- (5) Jürgen Nuss, M. J. *Z Anorg Allg Chem* **2002**, 628, 1152.
- (6) Morcrette, M.; Larcher, D.; Tarascon, J. M.; Edstrom, K.; Vaughey, J. T.; Thackeray, M. M. *Electrochim Acta* **2007**, 52, 5339.
- (7) Pearson, W. B. *Can J Phys* **1964**, 42, 519.
- (8) Pearson, W. B. *Z Kristallogr* **1985**, 171, 23.
- (9) Song, S. W.; Reade, R. P.; Cairns, E. J.; Vaughey, J. T.; Thackeray, M. M.; Striebel, K. A. *Journal of the Electrochemical Society* **2004**, 151, A1012.
- (10) Vitkina, T. Z.; Zhigadlo, N. D.; Ryzhkovskii, V. M. *Crystal Research and Technology* **1988**, 23, 945.
- (11) Zhang, G.; Huang, K. L.; Liu, S. Q.; Zhang, W.; Gong, B. L. *Journal of Alloys and Compounds* **2006**, 426, 432.
- (12) Ren, J. G.; He, X. M.; Pu, W. H.; Jiang, C. Y.; Wan, C. R. *Electrochim Acta* **2006**, 52, 1538.
- (13) Sarakonsri, I.; Johnson, C. S.; Hackney, S. A.; Thackeray, M. M. *Journal of Power Sources* **2006**, 153, 319.
- (14) Sarakonsri, T.; Apirattanawan, T.; Tungprasurt, S.; Tunkasiri, T. *J Mater Sci* **2006**, 41, 4749.
- (15) Kulifay, S. M. *J Am Chem Soc* **1961**, 83, 4916.
- (16) Sounart, T. L.; Liu, J.; Voigt, J. A.; Hsu, J. W. P.; Spoerke, E. D.; Tian, Z.; Jiang, Y. B. *Advanced Functional Materials* **2006**, 16, 335.
- (17) Innocenti, M.; Forni, F.; Pezzatini, G.; Raiteri, R.; Loglio, F.; Foresti, M. L. *J Electroanal Chem* **2001**, 514, 75.
- (18) Loglio, F.; Innocenti, M.; Pezzatini, G.; Foresti, M. L. *J Electroanal Chem* **2004**, 562, 117.
- (19) Padhi, D.; Gandikota, S.; Nguyen, H. B.; McGuirk, C.; Ramanathan, S.; Yahalom, J.; Dixit, G. *Electrochim Acta* **2003**, 48, 935.
- (20) Allred, D. B.; Cheng, A.; Sarikaya, M.; Baneyx, F.; xe; ois; Schwartz, D. T. *Nano Lett.* **2008**.
- (21) Osafo-Acquaah, A.; Shapir, Y.; Jorne, J. *Journal of the Electrochemical Society* **2006**, 153, C535.

- (22) Vandenbrande, P.; Winand, R. *Journal of Applied Electrochemistry* **1993**, *23*, 1089.
- (23) Amy L. Prieto, M. S. S., Marisol S. Martin-Gonzalez, Ronald Gronsky, Timothy Sands, And Angelica M. Stacy *Journal of American chemical Society* **2001**, *123*, 7160.
- (24) Amy L. Prieto. Marisol Martin-Gonzalez, j. K., Ronald Gronsky, Timothy Sands, and Angelica M. Stacy *Journal of American chemical Society* **2003**, *123*, 2388.
- (25) Gao, T.; Meng, G. W.; Zhang, J.; Wang, Y. W.; Liang, C. H.; Fan, J. C.; Zhang, L. D. *Appl Phys a-Mater* **2001**, *73*, 251.
- (26) Switzer, J. A.; Hung, C. J.; Huang, L. Y.; Switzer, E. R.; Kammler, D. R.; Golden, T. D.; Bohannan, E. W. *J. Am. Chem. Soc.* **1998**, *120*, 3530.
- (27) Tetsuya, O. *The Chemical Record* **2004**, *4*, 346.
- (28) Zhu, Y. C.; Geng, W. T. *J. Phys. Chem. C* **2008**.
- (29) Leitner, K.; Lerf, A.; Winter, M.; Besenhard, J. O.; Villar-Rodil, S.; Suarez-Garcia, F.; Martinez-Alonso, A.; Tascon, J. M. D. *Journal of Power Sources* **2006**, *153*, 419.
- (30) Li, N. C.; Martin, C. R. *Journal of the Electrochemical Society* **2001**, *148*, A164.
- (31) Li, N. C.; Martin, C. R.; Scrosati, B. *Electrochemical and Solid State Letters* **2000**, *3*, 316.
- (32) Li, N. C.; Martin, C. R.; Scrosati, B. *Journal of Power Sources* **2001**, 97-8, 240.
- (33) Sides, C. R.; Li, N. C.; Patrissi, C. J.; Scrosati, B.; Martin, C. R. *Mrs Bulletin* **2002**, *27*, 604.
- (34) Sides, C. R.; Martin, C. R. *Advanced Materials* **2005**, *17*, 125.
- (35) Gonzalo, R.; Humberto, G.; Ricardo, S.; Ricardo, E. M.; Enrique, A. D. *Electrochemical and Solid-State Letters* **2008**, *11*, K19.
- (36) M. Venkata Kamalakar, A. K. R. *Advanced Materials* **2008**, *20*, 149.
- (37) Milchev, A. *Russian Journal of Electrochemistry* **2008**, *44*, 619.
- (38) Radisic, A.; Vereecken, P. M.; Hannon, J. B.; Searson, P. C.; Ross, F. M. *Nano Lett.* **2006**, *6*, 238.
- (39) Xu, L.; Chen, Q.; Xu, D. *J. Phys. Chem. C* **2007**.
- (40) Choi, K. S. *Dalton T* **2008**, 5432.
- (41) Borissov, D.; Tsekov, R.; Freyland, W. *J Phys Chem B* **2006**, *110*, 15905.
- (42) Geoffroy, H.; Jan, D. H.; Karen, M.; Philippe, M. V. *Electrochemical and Solid-State Letters* **2008**, *11*, K47.
- (43) Tena-Zaera, R.; Elias, J.; Le; x; vy, C.; x; ment, C.; Bekeny, C.; Voss, T.; Mora, S.; x; Iva; x; Bisquert, J. *J. Phys. Chem. C* **2008**, *112*, 16318.
- (44) Fukami, K.; Kobayashi, K.; Matsumoto, T.; Kawamura, Y. L.; Sakka, T.; Ogata, Y. H. *Journal of The Electrochemical Society* **2008**, *155*, D443.
- (45) Borissov, D.; Isik-Uppenkamp, S.; Rohwerder, M. *The Journal of Physical Chemistry C* **2009**, *113*, 3133.
- (46) Jin, C. G.; Zhang, G. Q.; Qian, T.; Li, X. G.; Yao, Z. *J Phys Chem B* **2005**, *109*, 1430.
- (47) Zhang, Y.; Li, G. H.; Wu, Y. C.; Zhang, B.; Song, W. H.; Zhang, L. *Advanced Materials* **2002**, *14*, 1227.
- (48) Li, N. C.; Mitchell, D. T.; Lee, K. P.; Martin, C. R. *Journal of the Electrochemical Society* **2003**, *150*, A979.

- (49) Nishizawa, M.; Mukai, K.; Kuwabata, S.; Martin, C. R.; Yoneyama, H. *Journal of The Electrochemical Society* **1997**, *144*, 1923.
- (50) Che, G.; Jirage, K. B.; Fisher, E. R.; Martin, C. R.; Yoneyama, H. *Journal of The Electrochemical Society* **1997**, *144*, 4296.
- (51) Winter, M.; Besenhard, J. O. *Electrochim Acta* **1999**, *45*, 31.
- (52) Wu, M. S.; Chiang, P. C. J.; Lee, J. T.; Lin, J. C. *J Phys Chem B* **2005**, *109*, 23279.
- (53) Wang, Q.; Wen, Z. H.; Li, J. H. *Inorg Chem* **2006**, *45*, 6944.
- (54) Park, M. S.; Kang, Y. M.; Wang, G. X.; Dou, S. X.; Liu, H. K. *Advanced Functional Materials* **2008**, *18*, 455.
- (55) Li, W. Y.; Xu, L. N.; Chen, J. *Advanced Functional Materials* **2005**, *15*, 851.
- (56) Hu, Y. S.; Demir-Cakan, R.; Titirici, M. M.; Muller, J. O.; Schlogl, R.; Antonietti, M.; Maier, J. *Angewandte Chemie-International Edition* **2008**, *47*, 1645.
- (57) Lou, X. W.; Wang, Y.; Yuan, C. L.; Lee, J. Y.; Archer, L. A. *Advanced Materials* **2006**, *18*, 2325.
- (58) Lan, Y.; Gao, X. P.; Zhu, H. Y.; Zheng, Z. F.; Yan, T. Y.; Wu, F.; Ringer, S. P.; Song, D. Y. *Advanced Functional Materials* **2005**, *15*, 1310.
- (59) Cui, L. F.; Yang, Y.; Hsu, C. M.; Cui, Y. *Nano Letters* **2009**, *9*, 3370.
- (60) Cui, L. F.; Ruffo, R.; Chan, C. K.; Peng, H. L.; Cui, Y. *Nano Letters* **2009**, *9*, 491.
- (61) Chan, C. K.; Ruffo, R.; Hong, S. S.; Huggins, R. A.; Cui, Y. *Journal of Power Sources* **2009**, *189*, 34.
- (62) Jiang, D. D.; Fu, Y. B.; Ma, X. H. *Acta Physico-Chimica Sinica* **2009**, *25*, 1481.
- (63) Chou, S. L.; Wang, J. Z.; Liu, H. K.; Dou, S. X. *Electrochemistry Communications* **2009**, *11*, 242.
- (64) Krazit, T.; Kanellos, M. In *cnet news*; cnet: 2006.
- (65) Long, J. W.; Dunn, B.; Rolison, D. R.; White, H. S. *Chemical Reviews* **2004**, *104*, 4463.
- (66) Amy, L. P. Ph. D, Univerisyt of California, Berekeley, 2001.
- (67) Sadasivan, V.; Richter, C. P.; Menon, L.; Williams, P. F. *Aiche J* **2005**, *51*, 649.
- (68) Piao, Y. Z.; Kim, H. *J Nanosci Nanotechno* **2009**, *9*, 2215.
- (69) Qiaojian, H.; Carmen, M. L.; Matthias, B.; Ralu, D. *J Appl Phys* **2008**, *104*, 023709.
- (70) He, C.; Zhang, P.; Zhu, Y. F.; Jiang, Q. *J. Phys. Chem. C* **2008**.
- (71) Gerein, N. J.; Haber, J. A. *J Phys Chem B* **2005**, *109*, 17372.
- (72) Gao, T.; Meng, G. W.; Wang, Y. W.; Sun, S. H.; Zhang, L. *Journal of Physics-Condensed Matter* **2002**, *14*, 355.
- (73) Changwook Kim, W. G. M. B. I. M. R. H. C. K. K. *Advanced Materials* **2008**, *20*, 1859.
- (74) Martin-Gonzalez, M.; Prieto, A. L.; Knox, M. S.; Gronsky, R.; Sands, T.; Stacy, A. M. *Chemistry of Materials* **2003**, *15*, 1676.
- (75) Martin-Gonzalez, M.; Prieto, A. L.; Gronsky, R.; Sands, T.; Stacy, A. M. *Advanced Materials* **2003**, *15*, 1003.
- (76) Marisol, S. M.-G.; Amy, L. P.; Ronald, G.; Timothy, S.; Angelica, M. S. *Journal of The Electrochemical Society* **2002**, *149*, C546.
- (77) Eliaz, N.; Gileadi, E. *Mod. Aspects Electrochem. FIELD Full Journal Title:Modern Aspects of Electrochemistry* **2008**, *42*, 191.

- (78) Winand, R. *Electrochim Acta* **1998**, *43*, 2925.
- (79) Walsh, F. C.; Herron, M. E. *J Phys D Appl Phys* **1991**, *24*, 217.
- (80) Vazquez-Arenas, J.; Vazquez, G.; Melendez, A. M.; Gonzalez, I. *Journal of the Electrochemical Society* **2007**, *154*, D473.
- (81) Survila, A.; Sironiene, B. *Soviet Electrochemistry* **1992**, *28*, 1443.
- (82) Sudipta, R.; Landolt, D. *Journal of The Electrochemical Society* **1995**, *142*, 3021.
- (83) Shao, W.; Zangari, G. *The Journal of Physical Chemistry C* **2009**, *113*, 10097.
- (84) Raub, E.; Dehoust, G.; Ramcke, K. *Metall* **1968**, *22*, 573.
- (85) Li-Shian, J.; Jeng-Kuei, C.; Thou-Jen, T.; Sun, I.-W. *Journal of The Electrochemical Society* **2009**, *156*, D193.
- (86) Kim, S. K. C. a. J. J. *Journal of the Electrochemical Society* **2006**, *153*, C822.
- (87) Kim, S. K.; Josell, D.; Moffat, T. P. *Journal of the Electrochemical Society* **2006**, *153*, C616.
- (88) Jung, S.; Gross, M. D.; Gorte, R. J.; Vohs, J. M. *Journal of the Electrochemical Society* **2006**, *153*, A1539.
- (89) Chyan, O.; Arunagiri, T. N.; Ponnuswamy, T. *Journal of the Electrochemical Society* **2003**, *150*, C347.
- (90) Biallozo, Sg *Electrochim Acta* **1972**, *17*, 1243.
- (91) Pourbaix, M. *Atlas of Electrochemical Equilibria in Aqueous Solutions*; 2nd ed.; National Association of Corrosion Engineers: Houston, 1974.
- (92) Mohamed, A. S. F. a. A. K. *Bulletin of Electrochemistry* **1990**, *6*, 677.
- (93) Ghosh, J. C.; Kappana, A. N. *Journal of Physical Chemistry* **1924**, *28*, 149.
- (94) Mosby, J. M.; Prieto, A. L. *J Am Chem Soc* **2008**, *130*, 10656.

CHAPTER 3

SOLUTION CHEMISTRY RELEVANT TO COPPER-ANTIMONY-CITRATE AQUEOUS SYSTEMS

Some of the text contained in this chapter consists of an article that appears in: Mosby, J. M.; Prieto, A. L. *Journal of American Chemical Society* **2008**, 130, 32, 10656.

3.1 Avoiding the formation of Sb_2O_3 in aqueous solutions

The first step in developing a procedure for the direct electrodeposition of Cu_2Sb from aqueous solution at a single potential was to investigate the electrochemistry of both antimony and copper salts. The first complexity is the insolubility of Sb_2O_3 in aqueous solutions, which was demonstrated in the end of the last chapter where it was determined that only micro-molar amounts of Sb^{3+} would be available for the deposition of Cu_2Sb even in solutions with a pH less than 3. The reduction of the micro-molar amounts of Sb^{3+} to antimony metal from these acidic solutions is also not possible because the high concentration of protons present are reduced to H_2 at potentials less negative than what is required to reduce Sb^{3+} according to Eq. 3.1.¹



It is therefore imperative to force Sb^{3+} to remain soluble in less acidic solutions and/or shift its reduction potential to less negative values. The literature shows this can be accomplished by using ligands to complex with Sb^{3+} , thus increasing the aqueous solubility, allowing antimony metal and alloys to be electrodeposited from aqueous solutions.³⁻¹⁰ The most common ligands used in antimony electrodeposition are tartaric and citric acids, which are also widely studied as brighteners, and levelers in the deposition and plating baths of other materials.^{5,11-19} The resulting complexation of the Sb^{3+} by the citrate species allows solutions with higher pH values to be used than found when tartrate was used. The presence of the citrate species in solution not only increases the solubility of Sb^{3+} at low pH, but also permits electrochemistry to be performed in solutions with higher pH because the electrochemical window can be widened to more

negative potentials. Both of these consequences of citrate complexation are critical for the direct deposition of Cu_2Sb developed in the work reported in this thesis.

In addition to binding with Sb^{3+} , citric acid also complexes with Cu^{2+} , thus deposition solutions containing Cu^{2+} , Sb^{3+} and citrate will have both Cu-citrate and Sb-citrate complexes. Details on the speciation of these complexes and the electrochemistry of solutions containing them will be given in later sections. For now, some basic information on the coordination environment for the antimony and copper citrate complexes will be discussed. Citric acid is a monohydroxy triprotic acid with a hydroxyl group in the alpha position relative to one of the carboxylic acid groups and in a beta position relative to the other two carboxylic groups (Figure 3.1). Das *et al.* used titrations to demonstrate that citric acid behaves as a tridentate ligand in the presence of Sb^{3+} .² The coordination number of the trivalent antimony was found to be four in the presence of citrate because the carboxylic acid alpha to the hydroxyl group, the hydroxyl group, one of the carboxylic acids beta to the hydroxyl group, and a water are all coordinated to the antimony.² The protonation of the carboxylic group that is not coordinated to antimony and the coordinated water was found to vary with pH. Divalent copper also has a coordination number of four in the presence of citrate, but in the copper case the citrate only acts as a bidentate ligand. The copper coordinates with the acidic oxygen of one of the beta carboxylic acids and the carboxyl oxygen of the alpha carboxylic acid.²⁰ Depending on the relative concentrations and pH the other two coordination sites are either hydrated or a second molecule of citrate coordinates with copper in the same way as the first citrate ligand.¹⁹ It has also been shown with titrations that di-copper di-citrate complexes are present at higher pH values.²⁰ As the complexes change with pH, the

reduction behavior of the metal ions from these citrate complexes was found to depend on pH.

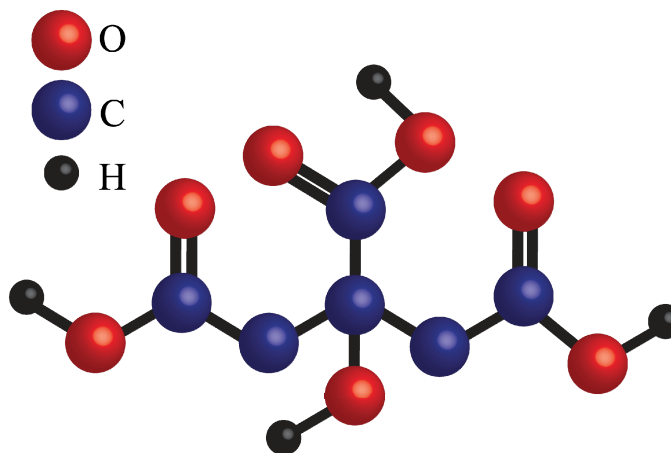


Figure 3.1: Drawing of citric acid the carbon atoms are represented in blue, the oxygen atoms are in red, and the hydrogen atoms are in grey. Only the acidic hydrogen atoms have been shown for clarity.

The pH of the solution plays an important role while expanding the electrochemical window of the deposition solution in the negative direction by decreasing the concentration of H_3O^+ . The degree of protonation of the citrate ligand complexed to the Cu^{2+} and Sb^{3+} also affects the reduction potential of the elements. After the experimental details are given, these effects will be discussed in detail.

3.2 Experimental procedure

The aqueous solutions used to perform the cyclic voltammetry studies reported in this chapter and for depositing Cu_2Sb films discussed throughout the rest of this thesis were all prepared with Millipore water (18 Ω). The solutions contained 0.2-0.8 M citric acid (99.5+%, Aldrich), 0.025-0.05 M antimony (III) oxide (nanopowder, 99.9+, Aldrich), and 0.04-0.1 M copper nitrate hemipentahydrate (99.9+%, Aldrich). The solutions were prepared by adding the citric acid to the Millipore water, followed by the

addition of Sb_2O_3 . The dissolution of the antimony oxide was aided by mechanical stirring, and takes over three hours. After the solution became clear the copper nitrate was added at which point the solution turned deep blue. After the addition of the copper nitrate the pH of the solution is 0.9 to 1.5 depending on the concentration of citric acid added. The solution pH was adjusted to different values using 5 M potassium hydroxide (ACS certified, Fisher) until oxides crashed out typically occurring above pH 7. As the pH increases the blue color of the solution darkens.

All cyclic voltammograms (CVs) and depositions were conducted using a three-electrode cell. In both cases platinum gauze was used as a counter electrode, and a saturated sodium calomel electrode (SSCE) 243 mV versus the standard hydrogen electrode (SHE) was used as the reference electrode. All potentials listed for the results in this chapter and chapters to follow will be against the SSCE, unless another reference potential is specified. For the CVs either a platinum (1.6 mm) or a glassy carbon (3.0 mm) disk electrode were used as the working electrode (WE), both purchased from BASi. For most CVs no attempt at degassing the solutions was made, otherwise the degassed CVs were taken using a glass Van Dyne cell and the nitrogen gas was ran through a glass bubbler. Three different potentiostats were used to run CVs of the deposition solution. The first potentiostat and the one used to perform the pH studies was a BAS 100B, the second was a CHI 660 workstation, and the third one was a Gamry Ref3000.

Some inconsistencies were seen in the CVs of the deposition solution in late 2007 and early 2008. At first the inconsistencies were thought to be from refluxing the solution to aid in the dissolution the Sb_2O_3 , but it was found this was not the problem.

Because the inconsistency in the CVs was an extra oxidation peak which matched an oxidation peak of solutions that only contained copper-citrate (as discussed later) the ratio of Cu^{2+} to Sb^{3+} was adjusted down to a ratio of 1 to 1 respectively. The extra oxidation peak in the CVs went away with a ratio of 1 to 1, but the films produced contained both antimony metal and Cu_2Sb . Because of this, the solution preparation was reexamined in order to find the source of the inconsistency. After looking through lab notebooks a large mistake was found, the molecular weight of the copper nitrate used to make the “2:1” solution was for $\text{Cu}(\text{NO}_3)_2$ ($187.422 \text{ g mol}^{-1}$), when in actuality copper(II) nitrate hemi(pentahydrate) was the precursor of Cu^{2+} used with a molecular weight of $232.59 \text{ g mol}^{-1}$. This meant that less Cu^{2+} was added to the solutions than was needed. When a new copper precursor copper(II) nitrate trihydrate was used to make the solutions the correct molecular weight ($241.60 \text{ g mol}^{-1}$) was used and the solutions had a 2 to 1 ratio of copper to antimony. The extra amount of Cu^{2+} added to the solutions was the source of the extra oxidation peak seen in the CVs. Table 1 shows how this error propagated and changed over the two year period.

Table 3.1- Concentrations of the species in solution after careful examination of the data in the lab notebooks. A clear shift in the concentration ratio of Cu^{2+} to Sb^{3+} is seen after new copper precursor was used (correct MW).

Date	Concentration	Concentration	Concentration	Ratio
	Citrate	Sb^{3+}	Cu^{2+}	
	M	M	M	
6/1/2006	0.80	0.05	0.08	1.6
6/1/2007	0.40	0.05	0.08	1.6
8/2/2007	0.40	0.05	0.08	1.6
8/28/2007	0.40	0.05	0.10	2.0
12/4/2007	0.40	0.05	0.10	2.0
12/21/2007	0.40	0.05	0.10	2.00
3/11/2008	0.40	0.05	0.10	2.02

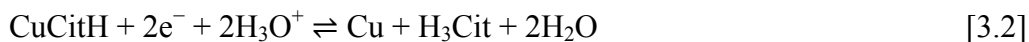
While this error in concentration added extra peaks in the CVs of the solution, the films deposited were not affected because the reduction potential required to deposit the copper species responsible for the extra oxidation peak is more negative than the deposition potential used. Therefore this copper species was not deposited onto the electrode during the deposition of Cu_2Sb . These details will be discussed in later sections with the corresponding CVs that represent the electrochemistry that is occurring.

The optimal concentration of citric acid was determined by varying the concentration of citric acid between 2-8 M in solutions containing 0.05 M Sb_2O_3 and $\text{Cu}(\text{NO}_3)_2$ separately. As the concentration of citric acid increased, the copper cathodic peak current decreased. This can be attributed to the equilibrium of the copper citrate complex; i.e. the more citric acid added the less free copper ions in solution. No difference in the anodic or cathodic current was observed for the antimony solutions. This is because of the requirement sufficient citric acid be present to complex all the antimony in order to prevent the formation of Sb_2O_3 . The lower limit of citric acid needed to dissolve Sb_2O_3 , forming 0.05 M solutions, was found to be 0.4 M. Because lower concentrations of citric acid are desired for the copper deposition and at least 0.4 M citric acid was needed to keep Sb^{3+} in solution, 0.4 M citric acid was used in all the resulting solutions.

3.3 Initial solution electrochemistry

The first deposition solutions studied contained 0.8 M citric acid, 0.1 M $\text{Cu}(\text{NO}_3)_2$ and 0.05 M Sb_2O_3 . Examining the CV of this solution (Figure 3.2d) reveals that scanning in the negative direction from an initial potential of 0.0 mV results in a broad peak at -180 mV. Following this peak the reduction of H_3O^+ leads to hydrogen evolution at -500

mV according to Eq. 3.1. After the polarity is switched a single anodic peak is seen at 340 mV. By comparison to the CV of 0.1 M Cu(NO₃)₂ and 0.8 M citric acid (Figure 3.2c) it is apparent that these peaks correspond to the deposition and oxidation of copper following Eq. 3.2.



Where HCit²⁻ represents the singly protonated citrate ion and the H₃Cit represents the fully protonated citric acid. A CV of 0.05 M Sb₂O₃ and 0.8 M citric acid is shown in Figure 3.2b, the evolution of hydrogen in this solution starts at -360 mV. This is the same potential that hydrogen evolution occurs in a blank solution (Figure 3.2a) which indicates that nothing is deposited onto the platinum electrode. This along with the absence of an anodic peak demonstrates that the evolution of hydrogen limits the electrochemical window such that the reduction of Sb³⁺ does not occur. A cathodic peak at 250 mV is seen in all the CVs Figure 3.2, ascribed to a phenomena occurring on the surface of the Pt working electrode, which will be discussed in Section 3.7.

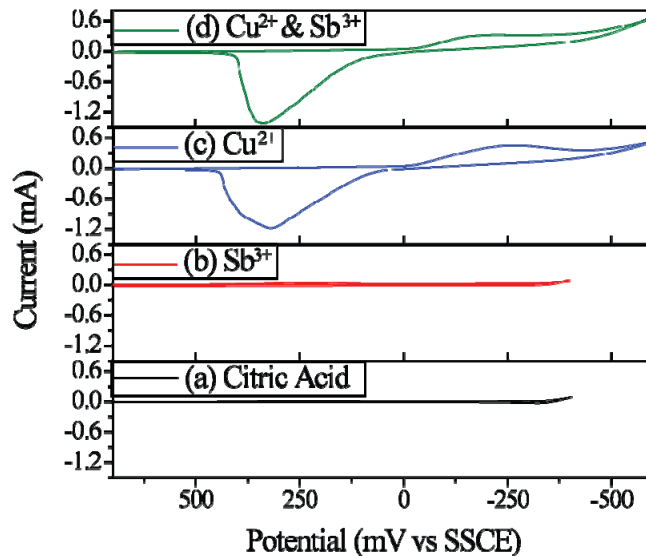


Figure 3.2: CVs of solutions with 0.8 M citric acid, pH 1.2, (a) blank, (b) 0.05 M Sb_2O_3 , (c) 0.1 M $\text{Cu}(\text{NO}_3)_2$, (d) 0.025 M Sb_2O_3 and 0.1 M $\text{Cu}(\text{NO}_3)_2$ at a pH 1.2. The scan rate was 400 mV s^{-1} and the reference electrode was SSCE.

The absence of a deposition peak for antimony in the CV in Figure 3.2b is most likely from the electrochemical window being limited by the reduction of H_3O^+ , which does not allow the Sb^{3+} reduction potential to be reached. In order to extend the electrochemical window, the pH of the solutions examined in Figure 3.2 was increased. Initial experiments showed two cathodic peaks were found to converged in CVs of solutions containing Cu^{2+} , Sb^{3+} , and citric acid at a pH of 6 (Figure 3.3d). Figure 3.3 contains CVs of the same four solutions examined in Figure 3.2, but with three parameters changed. First the concentration of the citric acid was cut in half to 0.4 M; second, the Sb^{3+} concentration was decreased to 0.05 M; and third, the pH of the solutions was adjusted to 6. It was found that there are major differences between the CVs of all four solutions shown in Figure 3.2 and Figure 3.3. This prompted a more thorough investigation into the effect that pH has on the electrochemistry of the solutions, which will be discussed in the following sections. The only differences for the first three

solutions that will be pointed out at this time are: (1) the blank (Figure 3.3a) has a second cathodic peak at -700 mV, (2) the CV of the antimony citrate solution (Figure 3.3c) has a shallow cathodic peak at -1000 mV and anodic peaks at 50 mV, and (3) the separation of the cathodic and anodic peak in the CV of the copper citrate solution (Figure 3.3b) has increased by approximately -750 mV. The differences between the CVs of the solutions containing both Sb^{3+} and Cu^{2+} are at a pH of 6 the cathodic peak is shifted to -1000 mV and has a shoulder at -1100 mV, while the anodic peak has shifted to 100 mV. Combining the speciation work reported in the literature with electrochemistry performed in the laboratory a more detailed analysis of the solution behavior exhibited in Figure 3.3 will be presented in the following sections.

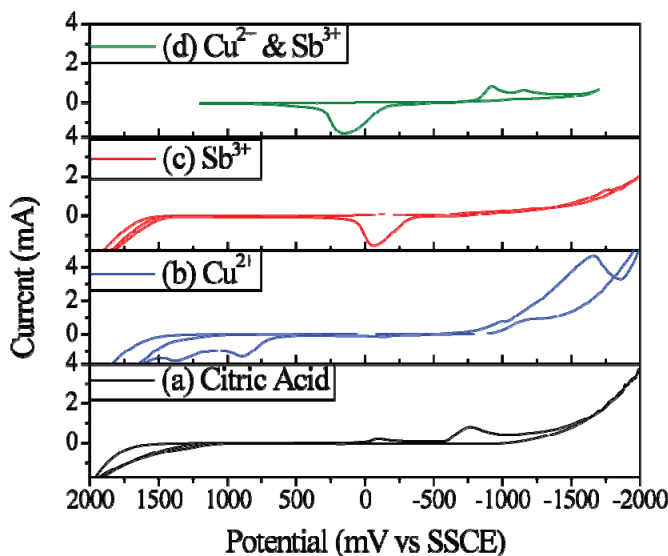


Figure 3.3: CVs of solutions containing (a) 0.4 M citric acid pH 6, (b) 0.1 M $\text{Cu}(\text{NO}_3)_2$, (c) 0.025 M Sb_2O_3 , (d) 0.025 M Sb_2O_3 and 0.1 M $\text{Cu}(\text{NO}_3)_2$ at a pH of 6. The scan rate was 250 mV s^{-1} and the reference electrode was SSCE.

Many researchers have studied the solution chemistry of copper citrate. Of those, Rode *et al.* provides details on the speciation of copper citrate solutions and lists an overview of the stability constants for the different copper citrate complexes that have

been tabulated over the years.¹⁹ Antimony citrate, however, has not been as extensively studied, and as a result a clear agreement on the complexes formed and their corresponding stability constants has yet to be reached. No papers with specific information on solution parameters containing copper, antimony and citric acid were found. But, there is one report of crystallizing $[\text{CuSb}(\text{C}_6\text{H}_6\text{O}_7^{2-})(\text{C}_6\text{H}_5\text{O}_7^{3-})(\text{H}_2\text{O}_2)] \cdot 2.5\text{H}_2\text{O}$ from acidic solutions of citric acid, antimony oxide, and copper nitrate.¹³ This last paper hints that mixed-metal complexes could be present in solution. The electrochemistry of each of these solutions will be investigated at different pH values to determine the origin of the two cathodic peaks that converge to a similar potential at a pH 6 in CVs of solutions containing Sb^{3+} , Cu^{2+} , and citric acid.

3.4 The pH dependence of the electrochemistry of citric acid

As mentioned previously, citric acid is a triprotic acid, and thus the pH of the solution controls the degree of deprotonation, which in turn controls the electrochemistry as has been shown in comparing CVs of citrate solutions at pH 1.2 (Figure 3.2a) and at pH 6 (Figure 3.3a). To determine the origin of the second reduction peaks that appears at -700 mV in Figure 3.3a, CVs of solutions with pHs of 1, 2, 3, 4, 5, and 6 were taken (Figure 3.4). A clear transition in the shape of the CVs between pH 4 (Figure 3.4b) and 5 (Figure 3.4c) was observed. The CVs of the citrate solutions at pH 1 and 2 were omitted from Figure 3.4 for clarity, as the key transition is seen from pH 3-5 (Figure 3.4a). The CVs were run starting at an open circuit potential (OCP) of c.a. 500 mV and first scanned in the negative direction. For all three acidic solutions (pH 1, 2, 3) a small cathodic peak was encountered at c.a. 0 mV (surface rearrangement on platinum electrode) followed by a dramatic increase in current due to the reduction of H_3O^+ and the evolution of

hydrogen. These two processes occurred at 0 mV and -450 mV at a pH of 3 (Figure 3.4a) and both shift in the negative direction with increasing pH. This trend continues as the pH is increased, except there is a dramatic shift in the potential corresponding to the hydrogen evolution from pH 3 to pH 5. The evolution of hydrogen in the CVs of the citrate solution at pH 5 (Figure 3.4c) occurs 800 mV more negative than in solutions at pH 3. The larger electrochemical window at this pH allows for the observation of a new reduction peak at -1000 mV. At a pH of 4 this peak is starting to take shape, but there is no evidence of it in solutions that have a pH less than 3. This peak is still present in CVs of citrate solutions at a pH 6 (Figure 3.4d) with the onset starting at the same potential (-600 mV) as in CVs of solutions at pH 5, but the peak maximum has shifted in the positive direction to a potential of -800 mV. Nothing specific in the literature has been found that provides insight on the reduction process that is occurring at -800 mV.

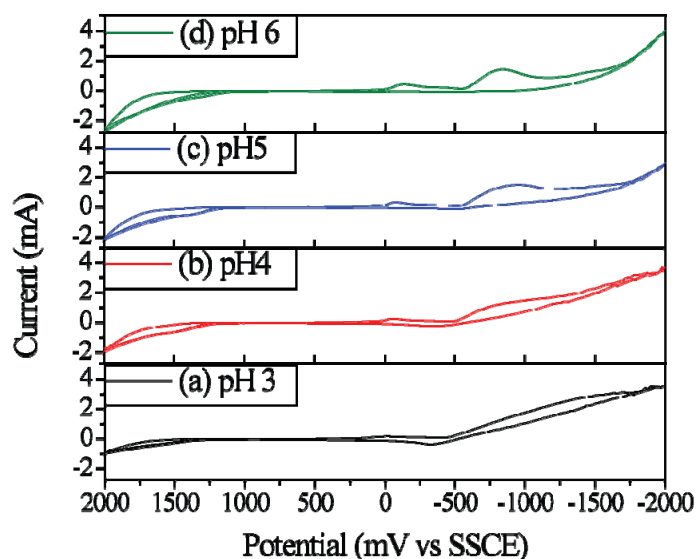


Figure 3.4: CVs of 0.4 M citric acid at (a) pH 3, (b) pH 4, (c) pH 5, and (d) pH 6. The scan rate was 500 mV s^{-1} and reference electrode was SSCE.

In an attempt to understand what the reduction process corresponding to the peak seen at -800 mV is in the CVs of solutions at a pH of 5 and 6 (Figure 3.4c & d) a

speciation diagram for citric acid was created following the procedure used by Rode *et al.*¹⁹ The dashed lines in the calculated speciation diagram for citric acid from pH 1 to 7 (Figure 3.5) represent the pH values of the CVs shown in Figure 3.4. For this discussion the abbreviation (Cit^{3-}) will correspond to the fully deprotonated citric acid, (HCit^{2-}) to the doubly deprotonated citric acid, (H_2Cit^-) to the singly deprotonated citric acid and (H_3Cit) as the fully protonated citric acid. In solutions with a pH of 2 or less the citric acid present is almost all in the H_3Cit form with a small amount of H_2Cit^- present (Figure 3.5). In a solution at a pH of 3 there is almost an equal amount of H_3Cit and H_2Cit^- with almost no HCit^{2-} present. H_2Cit^- is the predominate species at a pH 4 with almost equal amounts of H_3Cit and HCit^{2-} present (Figure 3.5).

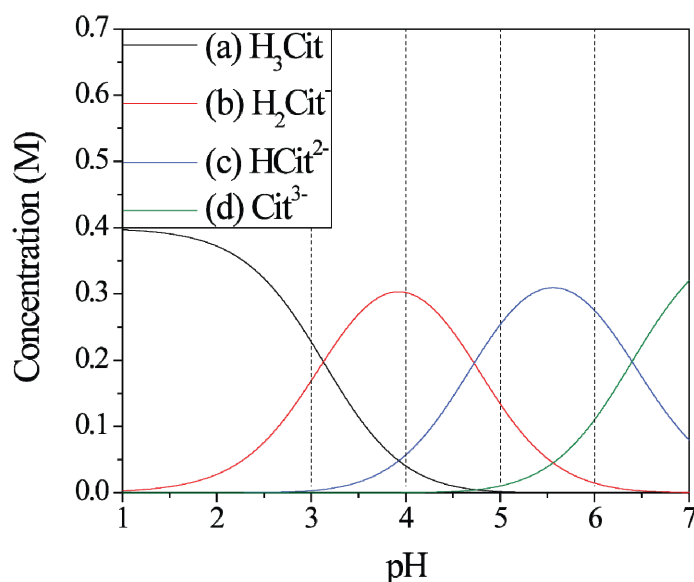


Figure 3.5: Calculated speciation diagram of 0.4 M citric acid. The concentrations of; **(a)** H_3Cit , **(b)** H_2Cit^- , **(c)** HCit^{2-} , and **(d)** Cit^{3-} are shown by the curves while the dashed lines represent the pHs of the CVs in Figure 3.3.

The small amount of (50 mM) of the HCit^{2-} present in a solution at a pH of 4 could account for the second cathodic peak starting to take shape at this pH. This conclusion is based on HCit^{2-} being the citrate species present in the highest

concentration at pH 5 and 6 where the reduction peak at -700 mV is dominant. The calculated speciation diagram in Figure 3.5 predicts that Cit^{3-} will be the predominate citrate species in solutions with a pH above 6.5. The CVs of solutions with a pH 7 and 11 were taken (not shown) and are almost indistinguishable from each other with the maximum current of the cathodic peak at -700 mV, an order of magnitude lower than the corresponding peak in the CVs of the solutions at pH 5 and 6. This further confirms that HCit^{2-} is the species being reduced at -700 mV in citrate solutions at pH 5 and 6. Following the common reduction path of carboxylic acids it can be predicted that the protonated carboxylic acid is being reduced to a primary alcohol according to Eq. 3.3.²¹



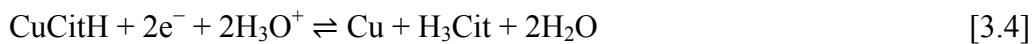
The reduction of a carboxylic acid to a primary alcohol is known to proceed using LiAlH_4 as the reducing agent but not NaBH_4 .²¹ This further supports that the reduction peak seen in the Figure 3.4c & d corresponds to Eq. 3.3, as the estimated reduction potentials for LiAlH_4 and NaBH_4 are -626 and -526 mV vs. SSCE respectively.²² With the reduction potential of LiAlH_4 where the reduction peak at -700 mV (Figure 3.4c & d) begins. The actual product of this reduction is not yet known, because there is a possibility that the reduction of one of the carboxylic acids causes the rearrangement into a cyclic hydrocarbon or reduction of other carboxylic acids.

3.5 The pH dependence of the electrochemistry of copper citrate

The copper citrate electrochemistry with respect to pH will be discussed next, since there is a considerable amount of literature to support the discussion.^{11-12,16,18-20,23-26} The paper by Rode *et al.* gives a good review of the different copper citrate complexes that are thought to exist in aqueous solutions and providing stability constants found for

them.¹⁹ For the concentrations and pH that are of interest to the deposition of Cu₂Sb only four of the fourteen listed are relevant. These four are: (1) CuCitH, (2) Cu₂Cit₂²⁻, (3) Cu₂Cit₂H₋₁³⁻, and (4) Cu₂Cit₂H₋₂⁴⁻.¹⁹ Rode *et al.* used the stability constants to create speciation diagrams of copper citrate solutions to describe the effect pH has on steady state polarization measurements.¹⁹ Following the experiments performed for citrate solutions and Rode *et al.*, cyclic voltammetry of copper citrate solutions with different pH will be compared to the calculated speciation diagram. The focus of the discussion will be on solutions with pH values of 2, 3, 4, and 6 (Figure 3.6), based on the calculated speciation diagram shown in Figure 3.7 (dotted lines).

The CVs of the copper citrate solutions were started at the OCP (100 mV) and first scanned in the positive direction to 2000 mV at which point the polarity was switched. The only electrochemistry observed during this anodic scan was the oxidation of water which started at 1400 mV. Upon switching the polarity, a cathodic peak at -500 mV characteristic of metal deposition was observed in solutions at pH 2 and 3 (Figure 3.6a & b). From the speciation diagram (Figure 3.7) this is the reduction of the Cu²⁺ from CuCitH according to Eq. 3.4.



There is a second cathodic peak at -1250 mV also seen in the CVs of both the pH 2 and pH 3 solutions (Figure 3.6a & b). These peaks can be assigned to the reduction of Cu₂Cit₂²⁻ which according to Figure 3.7 is present in both solutions (small amounts at pH 2) according to Eq. 3.5.



The CV of the solution at pH 3 (Figure 3.6b) has a third cathodic peak at -1900 mV corresponding to the reduction of $\text{Cu}_2\text{Cit}_2\text{H}_{-1}^{3-}$, which is also present in solution at this pH (Figure 3.7) according to Eq. 3.6.



Upon switching the polarity at -2000 mV and scanning in the positive direction a single anodic peak corresponding to the stripping peak of copper is seen at 700 and 500 mV in the CVs of both solutions at pH 2 and 3 respectively (Figure 3.6a& b). The reason for one oxidation peak is the stripping of the copper metal off the electrode happens at a single potential. Once the Cu^{2+} is released the system will reach equilibrium according to the speciation diagram through reactions in solutions, which is the cause of the broadness of the anodic peak.

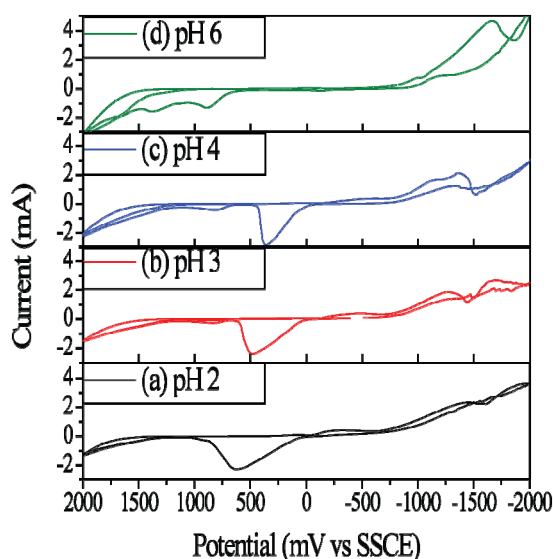


Figure 3.6: CVs of 0.1 M copper nitrate in 0.4 M citric acid at (a) pH 2, (b) pH 3, (c) pH 4, (d) pH 6. The scan rate was 250 mV s^{-1} and reference electrode was SSCE.

The CV of the solution at a pH 4 (Figure 3.6c) also has three cathodic peaks corresponding to the reduction of the different complexes present according to the

speciation diagram (Figure 3.7). The first and second cathodic peaks observed at -500 and -1200 mV are similar to the potential of the cathodic peaks present in the CVs of the solutions at pH 2 and pH 3 (Figure 3.6a & b) assigned to Eq. 3.4 and 3.5 respectively. There is a third cathode peak at -1380 mV in the CV for pH 4 (Figure 3.6c) which corresponds to the reduction of $\text{Cu}_2\text{Cit}_2\text{H}_{-2}^{4-}$ according to Eq. 3.7.¹⁹



According to Rode *et al.* the formation of $\text{Cu}_2\text{Cit}_2\text{H}_{-2}^{6-}_{(\text{ads})}$ passivates the working electrode.¹⁹ This prohibits Eq. 3.6 from occurring at -1900 mV even though according to the speciation diagram (Figure 3.7) $\text{Cu}_2\text{Cit}_2\text{H}_{-1}^{3-}$ is still present in the solution at this pH. Upon reversal of the scan direction there are two anodic peaks, the first at 500 mV due to the dissolution of copper, and the second smaller anodic peak at 780 mV is due to the oxidation of the $\text{Cu}_2\text{Cit}_2\text{H}_{-2}^{6-}_{(\text{ads})}$. The CV of the solution at a pH 6 in Figure 3.6d has two cathodic peaks which correspond to the reduction of the two complexes present according to Figure 3.7: $\text{Cu}_2\text{Cit}_2^{2-}$ following Eq. 3.5 (-1200 mV) and $\text{Cu}_2\text{Cit}_2\text{H}_{-2}^{4-}$ following Eq. 3.7 (-1700 mV). The amount of $\text{Cu}_2\text{Cit}_2^{2-}$ present at pH 6 is small, so upon reversing the polarity, the dissolution of copper is not present in the CV (Figure 3.6d), but there are two anodic peaks at 880 and 1380 mV which correspond to the oxidation of $\text{Cu}_2\text{Cit}_2\text{H}_{-2}^{6-}_{(\text{ads})}$. The increase in current and the presence of the second oxidation peak compared to the CV of the solution at pH 4 (Figure 3.6c) can be attributed to the fact that the majority of Cu^{2+} is $\text{Cu}_2\text{Cit}_2\text{H}_{-2}^{4-}$.

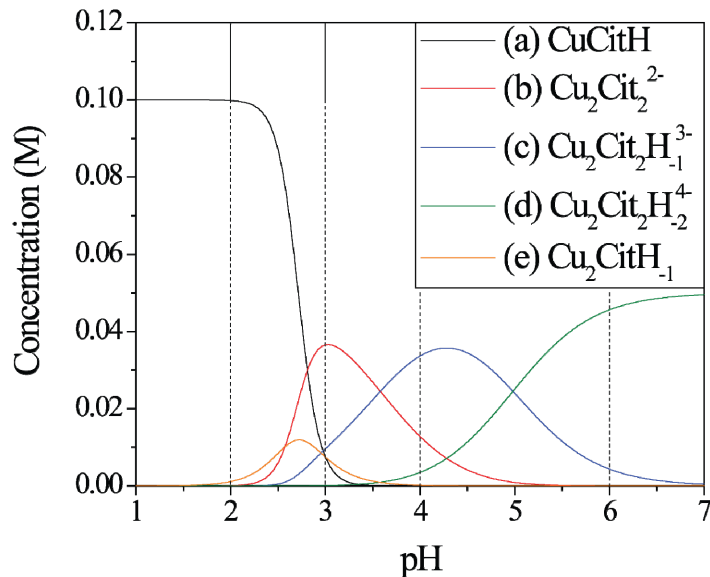


Figure 3.7: Calculated speciation Diagram of 0.1 M $\text{Cu}(\text{NO}_3)_2$ and 0.4 M citric acid. The concentrations of; **(a)** H_3Cit , **(b)** H_2Cit^- , **(c)** HCit^{2-} , and **(d)** Cit^{3-} are shown by the curves while the dashed lines represent the pHs of the CVs in Figure 5.

3.6 The pH dependence of the electrochemistry of antimony citrate

The next system that will be discussed are the antimony citrate solutions. There is considerably less information in the literature for antimony citrate solution composition, but the use of citric acid to make plating baths of antimony is a common means of keeping Sb_2O_3 from precipitating out of solution.^{2,5,15,27} Das *et al.* reported titrations in solution containing antimony and citric acid and determined that there are three different antimony citrate species possible depending on the solution pH.² Using the tabulated data from Das *et al.* a speciation diagram (Figure 3.8) was created with the three complexes that are reportedly formed.² The three complexes only differ by the protonation of the ligands attached to the Sb^{3+} . In solutions with a pH less than 3 $\text{H}_2\text{OSbHCit}$ is the predominate species, in solutions with a pH between 3 and 4.5 $\text{H}_2\text{OSbHCit}$ is predominate, and from 4.5 up to 6 it was determined that HOSbCit is the predominate species in solution.²

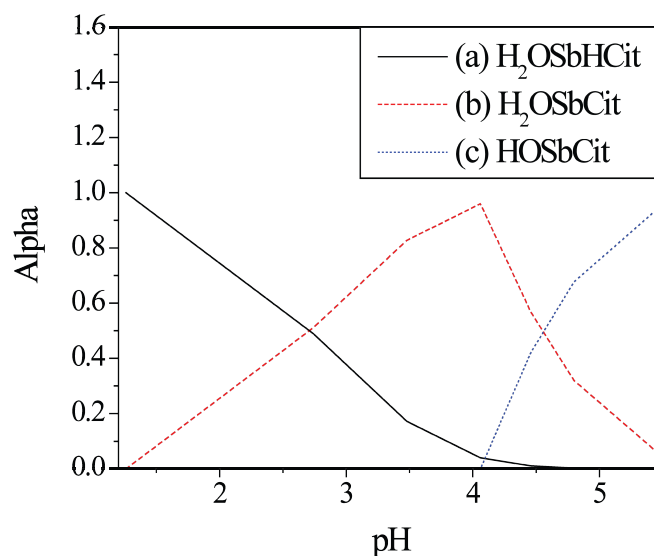
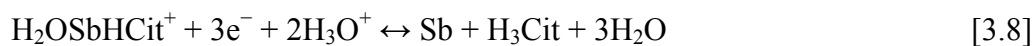
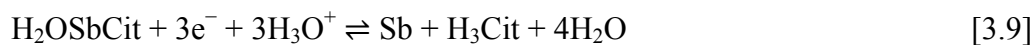


Figure 3.8: Speciation plot for antimony citrate solutions. The complexes only differ by the protonation of the ligands. Between pH 1 and 6 the complex starts as **(a)** H₂OSbHCit at low pH, then **(b)** H₂OSbCit and ends up as **(c)** HOSbCit right before pH 6. The plot was made using tabulated data from Das *et al.*²

Cyclic voltammograms of 0.025 M Sb₂O₃ and 0.4 M citric acid solutions were examined at pH values ranging from 1 to 7. The CVs of three solutions at pH 1, 3, and 5 are shown in Figure 3.9 to demonstrate the pattern observed for the antimony citrate case. Like the CVs taken for the copper citrate solution the CVs were started at the OCP (500 mV) and scanned first in the positive direction until 2000 mV, then the polarity was switched and the potential was scanned in the negative direction. At pH 1 a small cathodic peak at 250 mV is present from a surface phenomenon that occurs on the Pt WE (Figure 3.9a), and then the reduction of H₃O⁺ begins at -300 mV. After switching the polarity at -2000 mV no anodic peaks are observed during the anodic scan which indicates that at this pH the potential for Eq 3.8 is more negative than -2000 mV.



The same behavior is observed in CVs of solutions at pH 2 (not shown), but in the CVs of solutions at pH 3 there is an anodic peak at 250 mV (Figure 3.9b). On the cathodic scan at a pH of 3 the reduction of H_3O^+ starts at the same potential as the pH 1 solution, but less current is passed at pH 3 (Figure 3.9b). The presence of an anodic peak is evidence that antimony is deposited onto the working electrode which would inhibit the reduction of H_3O^+ compared to a bare platinum electrode. While the antimony citrate complex at a pH 3 is not much different than the complex at pH 1 the reduction potential for Eq. 3.10 is shifted positive of -2000 mV and based on the reduction in current for the hydrogen evolution that occurs at -1000 mV antimony could start depositing at potentials positive of -1000 mV.



According to Figure 3.5 only half of the citrate present in solution at pH 3 is fully deprotonated, thus following the deposition of antimony according to Eq. 3.9 equilibrium will be reached via Eq. 3.10.



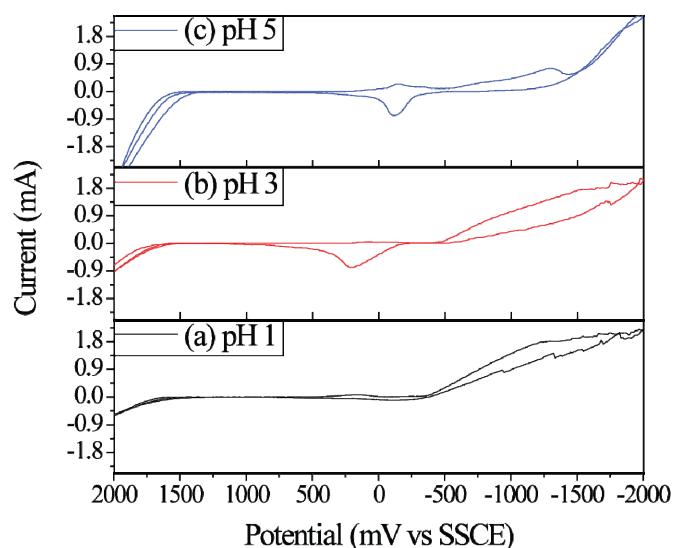
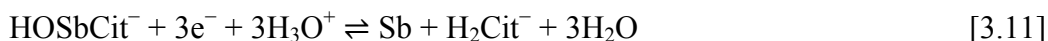


Figure 3.9: CVs of 0.025 M antimony oxide in 0.4M citric acid at **(a)** pH 1, **(b)** pH 3, and **(c)** pH 5. The scan rate was 500 mV s^{-1} and reference electrode was SSCE.

The CV of the pH 5 solution (Figure 3.9c) is the first case where the cathodic peak due to the deposition of antimony can be distinguished from the hydrogen evolution at -1000 mV . This is because the amount of current corresponding to the hydrogen evolution has been reduced by a factor of five compared to the bare platinum electrode (Figure 3.9a). This large reduction is from antimony plating out on the WE corresponding to Eq. 3.11.



According to Figure 3.5 only a small amount of $\text{H}_2\text{Cit}^{2-}$ would be present in the solution at a pH of 5 thus equilibrium will be reached following Eq. 3.12 and 3.13.



There is an anodic peak corresponding to the reverse of Eq. 3.11 in the CV of the solution at pH 5 (Figure 3.9c). Compared to the anodic peak in the CV of the solution at pH 3 the

anodic peak of the solution at pH 5 has shifted to more negative potentials (0 mV) and is considerably larger. This demonstrates that more antimony is deposited from solutions at pH 6 than at pH 3. Using the pH dependence of the complexes reported by Das *et al.* these results show that the reduction potential of Sb^{3+} to Sb^0 shifts to more positive potentials as the pH is raised. With such small changes in the complexes during the change in pH the cause of this dramatic shift in reduction potential is not yet clear.

3.7 The pH dependence of the electrochemistry of antimony copper citrate

Now that the pH dependence of citrate solutions with the individual elements (Cu^{2+} and Sb^{3+}) have been described, the pH dependence of solutions containing 0.025 M Sb_2O_3 , 0.1 M $\text{Cu}(\text{NO}_3)_2$ and 0.4 M citric acid will be addressed. The CVs in Figure 3.10 represent the trend seen for these solutions, and will be explained using the discussion given on the CVs of the separate solutions presented earlier in the chapter. During the cathodic scan of the CV for the solution at pH 2 in Figure 3.10a a cathodic peak occurs at -250 mV, followed by a gradual increase in cathodic current. This reduction peak occurs at a similar potential as the reduction peak corresponding to Eq. 3.4 in the CV of the copper citrate solution at pH 2 (Figure 3.6a). On the anodic scan there is a broad anodic peak that starts at 0 mV and has a maximum at 1200 mV (Figure 3.10a), this peak starts at the same potential as the anodic peak of copper citrate solution (Figure 3.6a), but is larger due to the presence of antimony citrate complexes. As was found in the antimony citrate solution at a pH 1, no evidence of the deposition of antimony is present in this CV (Figure 3.10a). The CV of the solution at pH 4 has one distinct cathodic peak at -1200 mV (Figure 3.10b), which was found to be the reduction potential from Eq. 3.5 in the copper citrate CV of Figure 3.6b. There are two anodic peaks in the CV of the pH 4

solution in Figure 3.10b. The first peak at -100 mV matches the anodic peak of antimony in Figure 3.9b which means after the first reduction peak antimony most of been deposited corresponding to Eq. 3.9. The second anodic peak at 500 mV in Figure 3.10b matches the anodic peaks of the copper citrate solution at pH 3 (Figure 3.6b). At this pH the CV shows that both copper and antimony metal is deposited from solution.

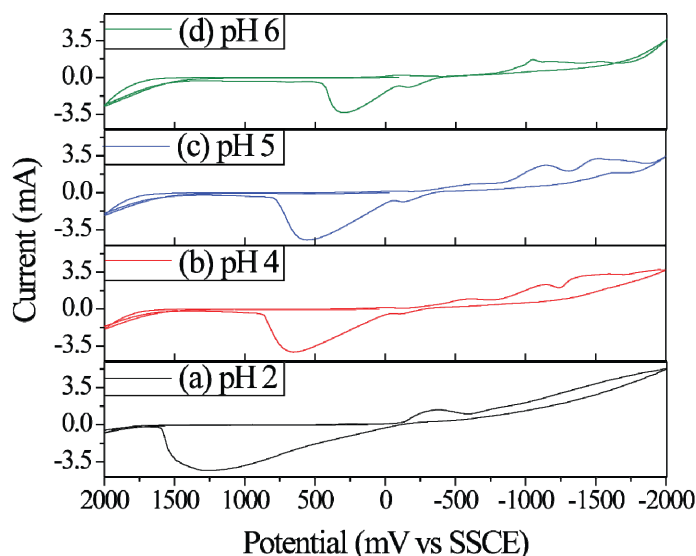
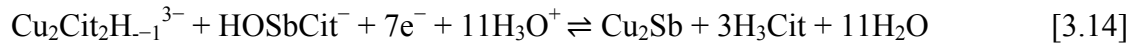


Figure 3.10: CVs of 0.025 M antimony oxide and 0.1 copper nitrate in 0.4 M citric acid at (a) pH 2, (b) pH 4, (c) pH 5, and (d) pH6. The scan rate was 500 mV s^{-1} and reference electrode was SSCE.

The cathodic scan of the CV of the solution at pH 5 has two reduction peaks: the first occurs at -1000 mV and the second at -1100 mV (Figure 3.10c). These peaks occur at the reduction potential found for Eq. 3.5 from CVs of the copper citrate (Figure 3.6c). This potential also corresponds to the reduction potential for Eq. 3.11 found from the CV of antimony citrate solution at pH 6 (Figure 3.9). The anodic peaks are similar to the peaks in the CV of the solution at a pH 4 (Figure 3.10b) but shifted in the negative direction. This is also the case for the anodic peaks in the CV of the solution at pH 6 (Figure 3.10d). As was found in the CV of the pH 5 solution there are two reduction

peaks in the CV of the pH 6 solution (Figure 3.10d), but the potentials are shifted in the positive direction and the current of the first peak (-900 mV) is now larger than the current of the second peak (-1100 mV). Also at this pH, there is a noticeable peak at -1650 mV, which has been found to correspond to the reduction of Sb^{3+} following Eq. 3.11. Performing CVs with different cathodic and anodic limits it was determined that this reduction peak and the oxidation peak at -100 mV are related, and are due to the deposition and dissolution of antimony. Besides this cathodic peak, the CVs of the solutions at pH 4, pH 5 and pH 6 (Figure 3.10b, c, &d) have reduction peaks at similar potentials, and films deposited around (± 300 mV) these potentials have been characterized as Cu_2Sb (discussed in the following chapter). Thus, the cathodic peak at -1100 mV for these solutions has been determined to be the deposition peak of Cu_2Sb , and the larger anodic peak at 300 mV for pH 5 and pH 6 and 500 mV for pH 4 corresponds to the stripping of Cu_2Sb . A few interesting comments need to be made on the effect that solution chemistry has on the electrochemistry of citrate solution containing antimony and copper.

As evidenced by the discussion in the previous sections, as the pH is increased from 1 to 6, the CVs of each individual metal indicate that the Cu^{2+} reduction peak shifts in the negative direction while the Sb^{3+} reduction peak shifts in the positive direction. In solutions with pH values greater than 4 the reduction potentials of both Cu^{2+} and Sb^{3+} converge to similar potentials. In citrate solutions containing both copper and antimony at pH 6 deposition at a single potential (-1050 mV) results in the formation of polycrystalline Cu_2Sb . From this it could be concluded that the process occurs by combining Eq. 3.8 and 3.11 giving Eq. 3.14.



While Eq. 3.14 provides a means of combining the chemistry of the separate solutions, the single potential deposition of crystalline Cu_2Sb cannot be accounted for with simply this equation. It is not common to deposit crystalline multiple-element materials at a single potential. For most two-element depositions the convergence of two reduction peaks leads to a solid-solution or an alloy, not a material with an order crystal structure. Also, without the presence of antimony, copper cannot be deposited from citrate solutions at pH 6 according to Eq. 3.7. One hypothesis is that there is a bi-metallic citrate species in the solution, which brings both Cu^{2+} and Sb^{3+} to the substrate at the same time allowing them to be reduced simultaneously. There are examples of bimetallic antimony citrate complexes with sodium and silver, and there is a report in the literature of a bimetallic copper antimony citrate being crystallized out of aqueous solutions.^{13,27} A second hypothesis is based on the knowledge that copper and antimony are highly soluble in each other, and thus the presence of the two elements on the substrate allows the formation of crystalline Cu_2Sb .²⁸

Before ending the chapter a brief note will be made on the cathodic peak seen in all the CVs shown in this chapter at around 100 mV which has been ascribed to phenomena occurring at the surface of the platinum working electrode. Figure 3.11 shows CVs of the same deposition solution using a platinum and a glassy carbon working electrode. Besides the cathodic peaks assigned to Cu_2Sb deposition being shifted to more negative directions in the CV taken with a GC electrode (Figure 3.11b), the first cathodic peak at 100 mV is missing and a third cathodic peak is seen at -1500 mV. An additional anodic peak (-100 mV) is seen in the CV taken with the GC electrode at a potential that

corresponds to the oxidation peak of antimony assigned from Figure 3.9c. Thus, the third cathodic peak at -1500 mV could be the deposition of antimony shifted to less negative potentials on the GC electrode compared to the platinum electrode. The absence of the reduction peak at 100 mV on the GC electrode supports the conclusion that this peak is from interaction of the surface of the platinum electrode with the electrolyte.

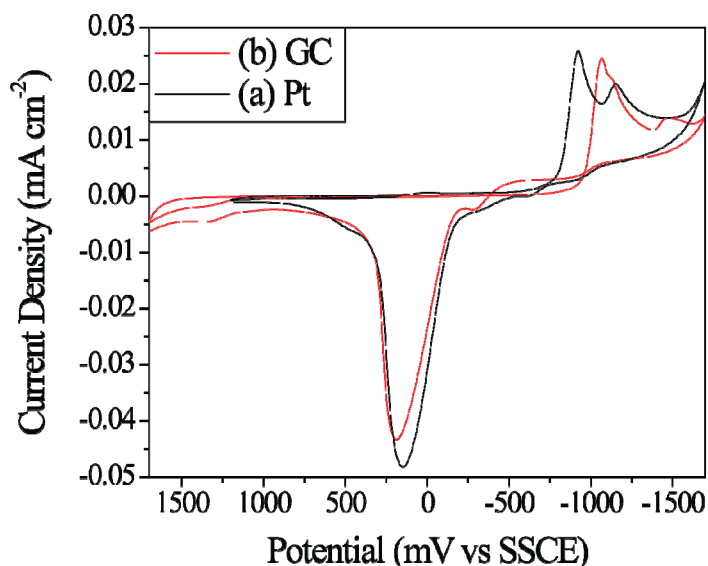


Figure 3.11: CVs of 0.025 M antimony oxide and 0.1 M copper nitrate in 0.4 M citric acid at pH 6. The cyclic voltammograms were taken using (a) Pt WE and (b) glassy carbon WE. The scan rate was 250 mV s^{-1} and the reference electrode was SSCE.

3.8 Conclusions

In this chapter the effect that pH has on the electrochemistry of citrate solution of copper and antimony was shown to be due to the speciation of the solution changing with pH. The electrochemistry of the citrate solutions of copper and antimony was successfully described using the known speciation data. Using the resulting information the CVs of solutions containing both copper and antimony were described. This is the first step in developing a mechanism for the single potential deposition of Cu_2Sb at a single potential from a solution at pH of 6. The final deposition mechanism will be

addressed in Chapter 5. From the investigations discussed above, the optimal deposition solution to deposit Cu_2Sb was found to be 0.4 M citric acid, 0.08 M $\text{Cu}(\text{NO}_3)_2$ and 0.025 M Sb_2O_3 at a pH of 6. Using this solution composition, the deposition conditions were optimized by analyzing films deposited at different conditions, as discussed in the following chapter.

3.9 References

- (1) Pourbaix, M. *Atlas of electrochemical Equilibria in Aqueous Solutions*; 2 ed.; National Association of Corrosion Engineers: Houston, 1974.
- (2) Das, R.; Pani, S. *Journal of the Indian Chemical Society* **1955**, *32*, 537.
- (3) Zhang, Y.; Li, G. H.; Wu, Y. C.; Zhang, B.; Song, W. H.; Zhang, L. *Advanced Materials* **2002**, *14*, 1227.
- (4) Z. G. Gasanov, F. G. A., F. S. Novruzova, Ma *Azerbaidzhanskii Khimicheskii Zhurnal* **1997**, 59.
- (5) Sadana, Y. *Metal Finishing* **1993**, *91*, 57.
- (6) Raub, E.; Dehoust, G.; Ramcke, K. *Metall* **1968**, *22*, 573.
- (7) Mohamed, A. S. F. a. A. K. *Bulletin of Electrochemistry* **1990**, *6*, 677.
- (8) Li, L.; Li, G. H.; Zhang, Y.; Yang, Y. W.; Zhang, L. D. *J Phys Chem B* **2004**, *108*, 19380.
- (9) Leimkuhler, G.; Kerkamm, I.; Reineke-Koch, R. *Journal of the Electrochemical Society* **2002**, *149*, C474.
- (10) Ghosh, J. C.; Kappana, A. N. *Journal of Physical Chemistry* **1924**, *28*, 149.
- (11) Gonzalez, S.; Alvarez, S. V.; Arevalo, A. *Electrochim Acta* **1983**, *28*, 535.
- (12) Uksene, V.; Survila, A.; Zukauskaitė, A. *Russian Journal of Electrochemistry* **1996**, *32*, 884.
- (13) Smith, G.; Sagatys, D. S.; Bott, R. C.; Lynch, D. E.; Kennard, C. H. L. *Polyhedron* **1992**, *11*, 631.
- (14) Cattarin, S. F., F.; Musiani, M.; Guerriero, P. *Journal of Applied Electrochemistry* **1994**, *24*, 439.
- (15) Sadana, Y. N.; Kumar, R. *Plating and Surface Finishing* **1979**, *66*, 58.
- (16) Roy, W. M. a. S. *Proceedings of Electrochemical Society* **2000**, *99*, 61.
- (17) Lozano-Morales, A.; Fitzgerald, J.; Singh, V.; Xie, X.; Podlaha, E. J. *Journal of the Electrochemical Society* **2006**, *153*, C567.
- (18) Daniele, P. G.; Ostacoli, G.; Zerbinati, O.; Sammartano, S.; Derobertis, A. *Transition Metal Chemistry* **1988**, *13*, 87.
- (19) Rode, S.; Henninot, C.; Vallieres, C. C.; Matlosz, M. *Journal of the Electrochemical Society* **2004**, *151*, C405.
- (20) Parry, R. W.; Dubois, F. W. *J Am Chem Soc* **1952**, *74*, 3749.
- (21) McMurry, J.; 5 ed.; Brooks/Cole: Pacific Grove, CA, 2000, p 1284.
- (22) Connelly, N. G.; Geiger, W. E. *Chemical Reviews* **1996**, *96*, 877.
- (23) Survila, A.; Sironiene, B. *Soviet Electrochemistry* **1992**, *28*, 1443.

- (24) Green, T. A.; Russell, A. E.; Roy, S. *Journal of the Electrochemical Society* **1998**, *145*, 875.
- (25) Eskhult, J.; Herranen, M.; Nyholm, L. *J Electroanal Chem* **2006**, *594*, 35.
- (26) Chassaing, E.; Quang, K. V.; Wiart, R. *Journal of Applied Electrochemistry* **1986**, *16*, 591.
- (27) Hartley, D. W.; Smith, G.; Sagatys, D. S.; Kennard, C. H. L. *J Chem Soc Dalton* **1991**, 2735.
- (28) Halimi, R.; Merabet, A. *Surf Sci* **1989**, *223*, 599.

CHAPTER 4

THE SINGLE POTENTIAL DEPOSITION OF Cu_2Sb FILMS

Some of the text contained in this chapter consists of an article that appears in: Mosby, J. M.; Prieto, A. L. *Journal of American Chemical Society* **2008**, 130, 32, 10656.

4.1 Introduction

In Chapter 3 it was demonstrated that solution chemistry plays an important role in the electrochemistry of aqueous citrate solutions of both copper and antimony. From cyclic voltammograms (CVs) it was found that the reduction potential of Cu^{2+} shifted in the negative direction and the reduction potential of Sb^{3+} shifted in the positive direction as the pH was increased. From this work, it was found that Cu_2Sb films could be deposited at a single potential (-1050 mV vs SSCE) from aqueous solution at pH 6. The role of the solution chemistry is only one part of the deposition. For successful electrodeposition the following parameters must also be accounted for: solution temperature, deposition potential, substrate material, and substrate quality. This chapter will focus on how these four parameters affected the electrodeposition of Cu_2Sb .

4.2 Experimental procedures

As determined from the experiments discussed in the last chapter Cu_2Sb films were electrodeposited from aqueous 0.4 M citric acid (99.5+% Aldrich) solutions containing 0.025 M antimony(III) oxide (nanopowder, 99.9+% Aldrich), and 0.08 M copper nitrate hemipentahydrate (99.9+% Aldrich). The specific details on solution preparation are discussed in Chapter 3. Briefly, the solutions were prepared by adding the citric acid to Millipore water (18Ω) followed by the addition of antimony oxide. The copper nitrate was subsequently added to the solution. The solution was ready for deposition after adjusting the pH to a value of 6 using 5 M potassium hydroxide (ACS certified, Fisher).

All depositions were conducted in a three-electrode cell, using three different potentiostats: a BASi 100B, a CHI 660workstation, and Gamry Ref3000. In all cases

platinum gauze was used as the counter electrode, and a saturated sodium calomel electrode (SSCE), 243 mV versus the standard hydrogen electrode, was used as the reference electrode. Either Copper or gold substrates with an area of 2-4 cm² were used as the working electrode. Two types of copper substrates were used. The first substrate was copper foil (0.25 mm thick, 99.98% Aldrich), which was mechanically polished using diamond paste and then chemically polished in 10% H₃PO₄ for less than 10 seconds. The second copper substrate and gold substrates were made using a Denton Vacuum evaporator with a Maxtek MDC-260 deposition controller. Glass slides were washed with Millipore water and methanol. The evaporator was used to deposit 5 nm of chromium onto the slides as an adhesion layer, followed by 200 nm of copper or gold. In order to deposit on a flat surface, clear nail polish was used to insulate the edges of the substrates and the back of the copper foil. The electrodepositions were carried out at a constant potential for ten minute periods. The temperature and the potential were varied in order to find the optimal parameters for Cu₂Sb deposition as discussed in the following sections. After the depositions the films were then copiously rinsed with distilled water and allowed to air dry prior to material characterization.

Compositional analysis of the surfaces of the electrodeposited Cu₂Sb films were performed using survey X-ray photoelectron spectroscopy (XPS) run with a 5800 series Multi-Technique ESCA system and analyzed using Multipak software and XPS Peak 4.1. An Al monochromic source operating at 350.0 W was used to scan from 10 to 1110 eV. XPS survey scans were taken before and after sputtering with an argon ion beam at 2 kv and a 3 by 3 raster. The sputtering removed adventitious carbon and any oxygen that could have formed on the surface of the film during drying. High resolution XPS was

performed using a signal to noise ratio of 200 for the $\text{Cu}2\text{p}^3$ and $\text{Sb}3\text{d}^5$ peaks. The scanning electron microscopy images of films were taken with a JEOL JSm-6500F equipped with energy EDS from Thermo Electron. Unless otherwise noted, an accelerating voltage of 15 kV was used unless stated otherwise to image the films. Energy dispersive spectroscopy (EDS) analysis of the nanowires was performed using an accelerating voltage of 10 kV. The powder XRD patterns were obtained with a Scintag X-2 advanced diffraction X-ray cabinet system using $\text{Cu K}\alpha$ that is equipped with a stationary stage and a Peltier Detector. Since the films are on 0.25 mm thick copper foil or a glass slide, the stage height was adjusted by using wedges of the same thickness.

4.3 Optimizing the deposition potential

Based on CVs of citrate solutions containing 0.025 M Sb_2O_3 and 0.08 M $\text{Cu}(\text{NO}_3)_2$ at a pH of 4, the reduction potential corresponding to the deposition of Cu_2Sb was determined to be -1100 mV. This conclusion was made on based on the potential of the peak in the CV, which is dependent on scan rate and is not always the best potential which to deposit films from. For these reasons the first deposition parameter to be discussed is the deposition potential. The optimal deposition potential was found by depositing five films at different potentials surrounding the cathodic peaks seen in the CV for the pH 6 solution of **Error! Reference source not found.**¹⁰. The five potentials chosen were -800 mV (the onset of the first cathodic peak), -900 mV (inflection point of first peak), -1000 mV (the first peak maximum), -1100 mV (the shoulder of the first peak), and -1200 mV (the backside of the first peak). Surface compositions determined by XPS survey scans of Cu_2Sb films deposited from the non-degassed solutions are shown in Table 4.1. The results in Table 4.1 show that the ratio of Cu/Sb decreased with

potential, with the desired ratio (2:1) found in films deposited between -1000 and -1100 mV.

Table 4.1- XPS compositional data of films deposited at different potentials from solutions containing 0.08 M $\text{Cu}(\text{NO}_3)_2$ 0.025 M Sb_2O_3 and 0.4 M citric acid at a pH 6. In all cases, the films were sputtered with an argon beam for 1 minute.

Potential mV vs SSCE	Cu2p3 Atomic%	Sb3d5 Atomic%
-800	75.9	24.1
-900	74.4	25.6
-1000	67.7	32.3
-1100	66.0	34.0
-1200	62.9	37.1

The surface composition of films deposited at less negative potentials (less than -1000 mV) were copper rich, while films deposited at higher negative potentials (greater than -1200 mV) were antimony rich. This can be explained by examining the CVs in Figure 3.10: the first reduction peak at -1000 mV was found to match the reduction peak for copper citrate and the third reduction peak at -1500 mV was found to match the reduction of the antimony citrate species. From the results listed in Table 4.1 it was concluded that a potential of -1050 mV be used to deposit Cu_2Sb films. Representative XPS survey scans of an electrodeposited Cu_2Sb film before and after the sputtering with argon are shown in Figure 4.1a & b. The atomic percent for copper (65.8%) and antimony (34.2%) given in Figure 4.1 were obtained from fitting the Cu $2p^3$ and the Sb $3d^5$ peaks of a high resolution XPS spectrum with XPS peak. This shows that after sputtering, the surface of the Cu_2Sb films electrodeposited at -1050 mV have the correct 2 to 1 ratio of Cu to Sb respectively.

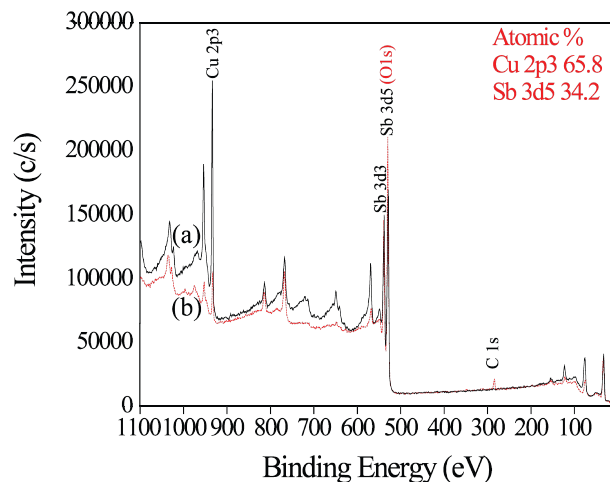


Figure 4.1: XPS survey scans of a Cu_2Sb film deposited at -1050 mV from deposition solution. The atomic percentages were taken from a high resolution scan with a P/N ratio of 300 for both the $\text{Cu } 2p^3$ and $\text{Sb } 3d^5$. **(a)** Survey scan after sputtering at 2 kV for 30.0 seconds, **(b)** Survey scan taken before sputtering.

X-ray diffraction (XRD) patterns, shown in Figure 4.2, were used for phase identification of the films deposited at the potentials listed in Table 4.1. The Cu substrate is responsible for the three peaks with the highest intensity. These three peaks at 43° , 50° and 74° 2θ index to the copper (111), (200) and (220) reflections of the cubic crystal structure of copper (PDF 01-071-4608). Three additional peaks are observed in the XRD pattern of the film deposited at -800 mV (Figure 4.2a). These peaks match the diffraction peaks for the tetragonal crystal structure of Cu_2Sb (PDF 01-085-0492). The broad peak at 44° ($\text{Cu}_2\text{Sb } 003$) is generally used as a fingerprint for the identification of Cu_2Sb in the literature.¹⁻⁶ The absence of additional Cu_2Sb peaks and the copper-rich composition determined by XPS indicates that the deposit comprises of a solid solution of Cu_2Sb and copper metal. Multiple Cu_2Sb diffraction peaks (Miller indices for each reflection are shown in Figure 4.2) appear in the XRD patterns of the films deposited at all other potentials, indicating that the films are more crystalline. The XRD patterns of the films deposited at -900 and -1000 mV (Figure 4.2b & c) are similar, but the peaks of the film

deposited at -1000 mV have higher relative peak intensities than the film deposited at -900 mV. Since all films were deposited for the same amount of time on substrates with the same dimensions, the increased peak intensities is likely due to either increased crystallinity or a higher growth rate (leading to a thicker film). Using the Scherer method the grain sizes of the film deposited at -1000 mV (35 nm) were found to be smaller than the film deposited at -900 mV (90 nm). Although the SEM images of these films also show similar surface morphologies, the film deposited at -900 mV (Figure 4.3a) shows larger features than the film deposited at -1000 mV (Figure 4.3b) which is consistent with the grain size calculated from the XRD patterns.

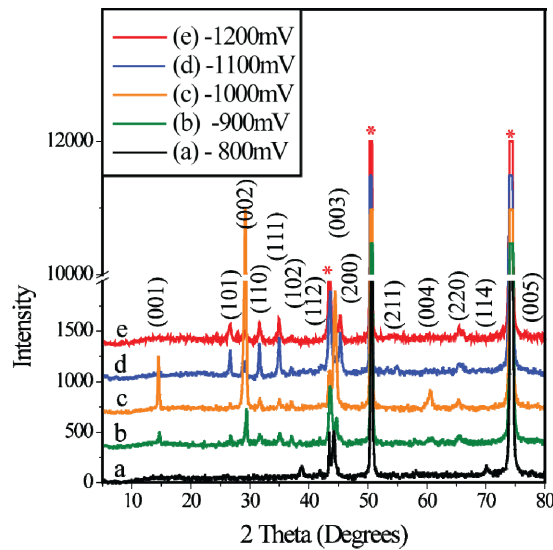


Figure 4.2: Powder XRD patterns of films deposited from solutions containing 0.1 M $\text{Cu}(\text{NO}_3)_2$ 0.025 M Sb_2O_3 and 0.4 M citric acid at a pH 6 at (a) -800 mV, (b) -900 mV, (c) -1000 mV, (d) -1100 mV, (e) -1200 mV.

The XRD patterns of films deposited from -1100 to -1200 mV can be indexed to Cu_2Sb (PDF 01-085-0492) and also have the predicted relative intensities. The morphologies of the films deposited at -1100 and -1200 mV are consistent with the differences between their XRD patterns (Figure 4.2c and d) and those of the films

deposited at -900 and -1000 mV (Figure 4.2a and b). The SEM image of the film deposited at -1100 mV (Figure 4.3c) clearly shows that the deposited material grew in a dendritic manner, instead of smooth congruent films of Cu_2Sb . The observed diameter of the dendritic rods was found to range from 50 to 150 nm with lengths greater than 600 nm. The average particle size calculated from peak broadening using the Scherer method was 50 nm, corresponding to the smallest observed diameter from SEM in Figure 4.3c. The SEM image of the film deposited at -1200 mV (Figure 4.3d) shows small spherical particles with 200 nm diameters on the surface of the film with a calculated grain size less than 20 nm. These small particles are responsible for the broadness of the peaks in the XRD pattern of this film (Figure 4.2e).

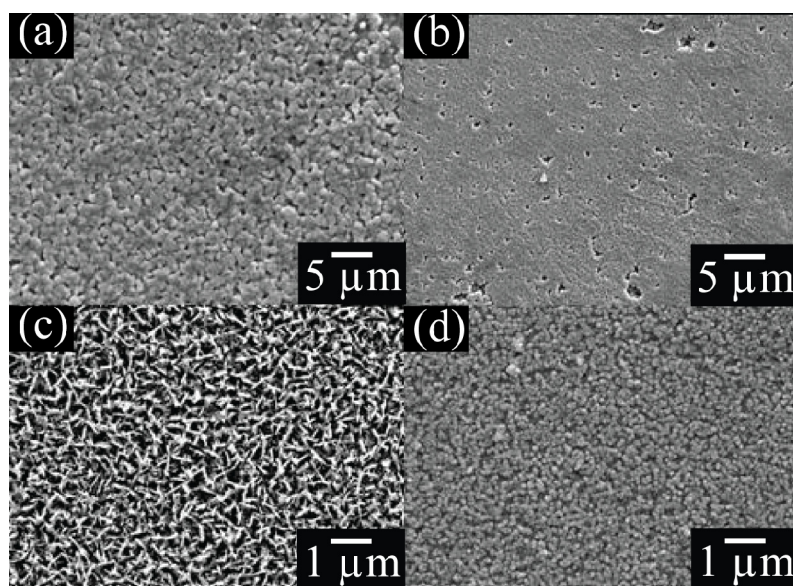


Figure 4.3: SEM images of films deposited at different potentials. The films were deposited at: (a) -900 mV, (b) -1000 mV, (c) -1100 mV and (d) -1200 mV verse SSCE. The pH 6 deposition solution contained 0.1 M $\text{Cu}(\text{NO}_3)_2$, 0.025 M Sb_2O_3 and 0.4 M citric acid.

For this XRD pattern, not only do the two-thetas match the data from PDF no. 01-085-0492 for Cu_2Sb but the relative intensities do as well. It was also concluded that the difference in relative intensities of the diffraction peaks between the films deposited at

high negative potentials (Figure d & e) and the films deposited at low negative potentials (Figure b & c) is indicative of a change in growth direction. The XRD patterns for the films deposited at -1100 and -1200 mV show no preferred orientation, while the films deposited at -900 and -1000 mV show a preferred orientation in (001) direction. From the discussion of the CVs in Chapter 3, it can be concluded that the preferred orientation correlates to electron-transfer limited deposition, whereas the diffusion-limited deposition Cu_2Sb films do not exhibit preferred orientation. The XPS, XRD, and SEM results for the potential dependence on the electrodeposition of Cu_2Sb demonstrated that to obtain the correct composition, high crystallinity, and compact thin films a deposition potential of -1050 mV should be used.

4.4 Temperature effect on crystallinity

The next deposition parameter that will be discussed is the effect that the deposition solution temperature has on the crystallinity of electrodeposited Cu_2Sb films. The temperature of the deposition solution is known to affect the crystallinity of the electrodeposited material. To examine this effect on Cu_2Sb , films were deposited at three different temperatures 5 °C, 22 °C, and 60 °C. XPS spectra of these films showed no evidence of compositional dependence on temperature. The films for this experiment were deposited at -1050 mV from solutions containing 0.1 M $\text{Cu}(\text{NO}_3)_2$, 0.025 M Sb_2O_3 , and 0.4 M citric acid held at pH 6. The Cu_2Sb film deposited at 5 °C is the least crystalline as determined by powder XRD (Figure 4.4c). The SEM image (Figure 4.5a) indicates that two types of morphologies are present. One of the two morphologies is spherical with diameters of ca. 250- 500 nm, which is intermixed evenly with dendritic rods that have a diameter of ca. 20 nm and lengths of 250 nm.

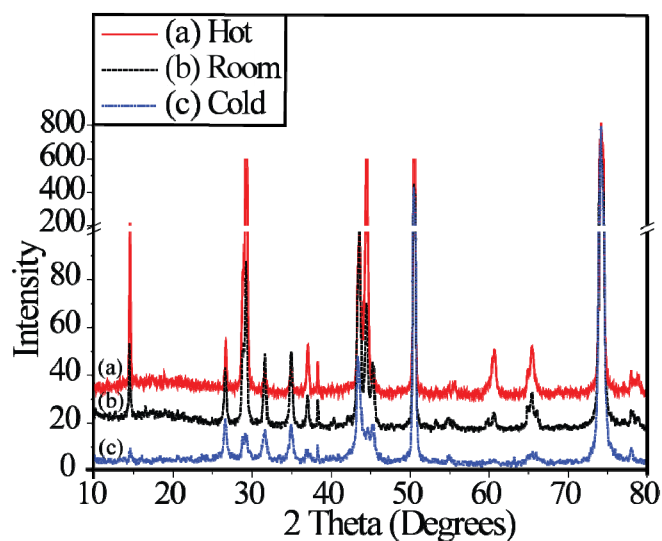


Figure 4.4: Powder XRD patterns of films deposited at different temperatures from solutions containing 0.1 M $\text{Cu}(\text{NO}_3)_2$ 0.025 M Sb_2O_3 and 0.4 M citric acid at a pH 6: (a) 60 °C, (b) 22 °C and (c) 5 °C.

The Cu_2Sb film deposited at room temperature is more crystalline as established by the peak broadness of the XRD pattern (Figure 4.4b) which is a match for Cu_2Sb PDF 01-085-0492. The grains present at the surface of this film are spherical with diameters of 200-300 nm as evidenced by the SEM image in Figure 4.5b. The peak intensities in the XRD pattern of the film deposited at 60 °C show that the films have strong preferred orientation as indicated by the anomalously large intensity for the (001) planes (Figure 4.4a). SEM images of this film (Figure 4.5c and d) illustrate that the surface of the film is composed of stacked cubes which have edge lengths of 100-300 nm. The results obtained from the temperature experiments demonstrated, not surprisingly, that increased solution temperature results in more crystalline films with preferred orientation.

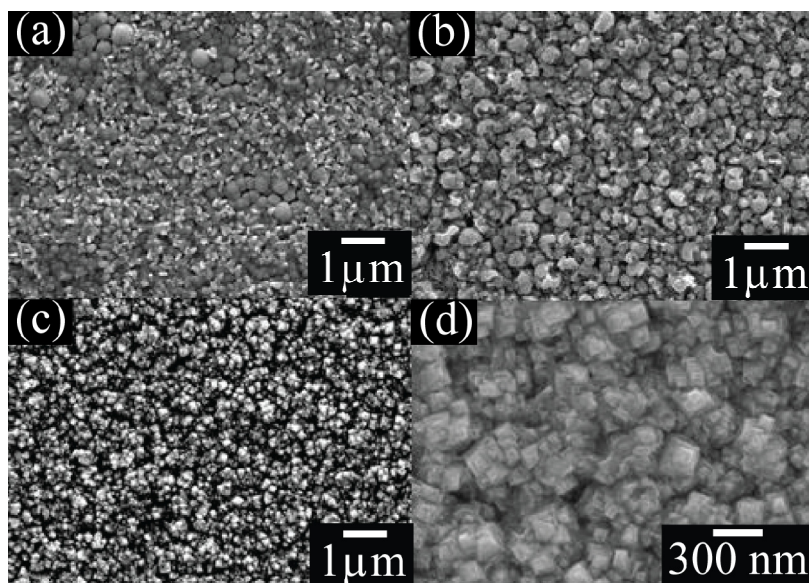


Figure 4.5: SEM images of the Cu_2Sb films deposited at different temperatures; (A) 5 °C, (B) 22 °C, (C) 8,000X 60 °C and (D) 30,000X 60 °C.

4.5 Cu_2Sb films deposited from aqueous solutions

Based on the previous observations, films of Cu_2Sb were electrodeposited at room temperature in solutions of 0.4 M citric acid at a pH of 6 with 0.1 M $\text{Cu}(\text{NO}_3)_2$ and 0.025 M Sb_2O_3 at -1050 mV vs. SSCE. Although the successful electrodeposition of Cu_2Sb was confirmed by the match of the films XRD pattern to the peak positions of Cu_2Sb (PDF 01-085-0492), three very small peaks at 38, 40 and 42° 2θ (circled in Figure 4.6) were observed. Each one of these reflections separately match reflections of different oxides (CuSb_2O_6 , Sb_2O_3 and CuO). We are hesitant, however, to identify the presence of any of these oxide phases on the basis of a single low-intensity reflection in an XRD pattern, especially because there is no evidence from EPS or EDS that oxides are present other than on the surface of the films.

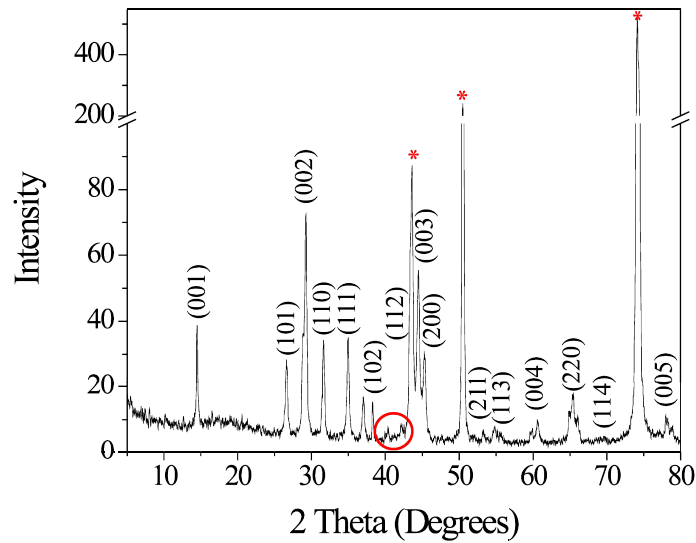


Figure 4.6: Powder XRD pattern of Cu_2Sb film deposited using optimized deposition solution and conditions. The peaks indicated by asterisks are from the Cu substrate, and peaks due to Cu_2Sb are indexed to PDF 01-085-0492. The red circle surrounds

In an effort to probe for the presence of oxide phases or amorphous in homogeneities in the as-deposited films, the film for which the XRD pattern is shown in Figure 4.6 was annealed for 5 hours under argon at 220 °C (XRD pattern shown in Figure 4.7). The peak positions observed in both XRD patterns are identical except that the extra peaks seen in Figure 4.6 are not present after annealing. This result is consistent with the removal of surface oxide phases.

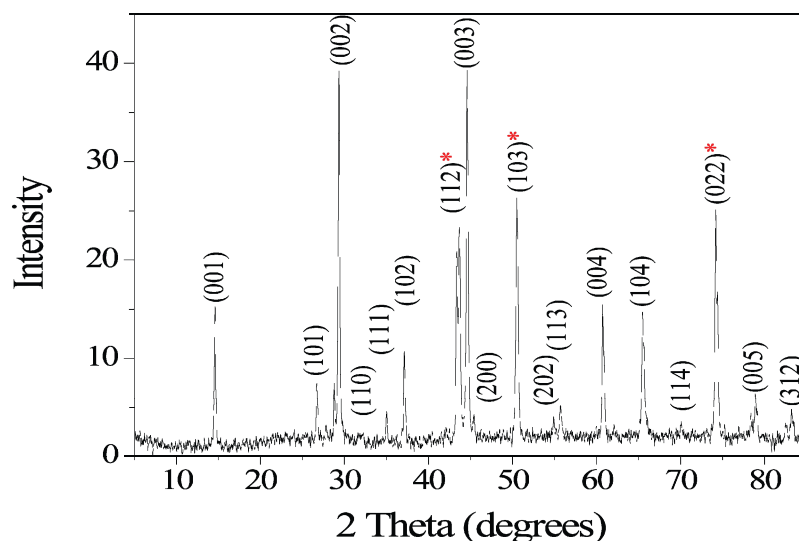


Figure 4.7: Powder XRD pattern of Cu_2Sb film deposited using optimized deposition solution and conditions and annealed for 5 hours at 220°C . The red asterisks indicate the copper substrate diffraction peaks, the other peaks are indexed for Cu_2Sb PDF 01-085-0492.

All films discussed thus far were electrodeposited for ten minutes from unstirred solutions. The Cu_2Sb film deposited at room temperature in Figure 4.6 has a thickness of $32.4\ \mu\text{m}$ as determined by an SEM cross-sectional image (Figure 4.8). Examining this image, it can also be concluded that there are no signs of discontinuities or void space in the electrodeposited film. This SEM image also shows that the electrodeposition of Cu_2Sb covers uneven voids of the copper substrate and deposits at a uniform thickness in this time period. Excluding any nucleation time, this corresponds to an average deposition rate of $3.24\ \mu\text{m}$ per minute, compared to an average of $0.72\ \mu\text{m}$ per minute for the deposition of copper from a $0.2\ \text{M}$ CuSO_4 solution at a constant current of $10\ \text{mA}$.²⁹ The rapid growth rate that we observe indicates that the solution parameters or interaction of the metal precursors with the substrate may facilitate the electrodeposition of Cu_2Sb .

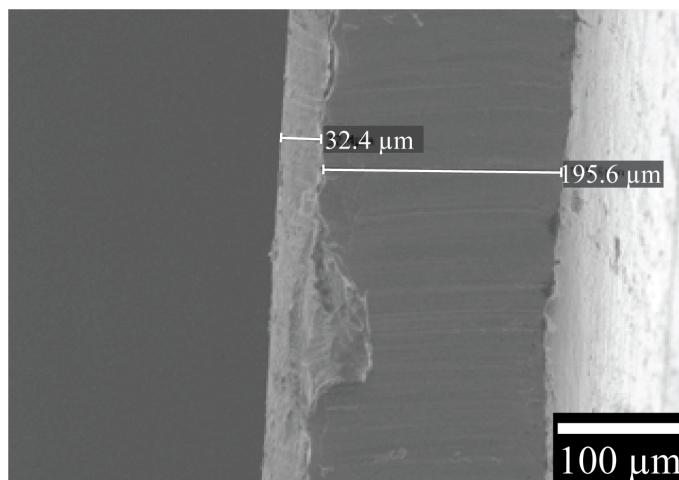


Figure 4.8: SEM of electrodeposited Cu₂Sb film. The film was deposited out of room temperature solution for ten minutes at a potential of -1050 mV vs. SSCE.

In order to establish the effect that the substrate has on the electrodeposited Cu₂Sb, films were also deposited on different substrates. For these depositions the same solution parameters and conditions used on the copper substrate were employed. All efforts to electrodeposit Cu₂Sb films on stainless steel or indium tin oxide substrates were unsuccessful. Cu₂Sb was formed during the deposition but instead of sticking to either of these substrates it fell to the bottom of the beaker. In these instances the substrate interaction with Cu₂Sb prevented films from being deposited, but the substrate was able to provide the appropriate conditions required for the formation of Cu₂Sb. Another substrate that was tested was gold evaporated onto glass. The Cu₂Sb films that were deposited on the gold substrate were found to be slightly less crystalline than the films deposited on copper substrate, but still exhibited a preferred orientation along the (001) direction (Figure 4.9). This implies that the observed preferred orientation for films deposited at -1050 mV is not due to templating by the substrate. These results also demonstrate that Cu₂Sb can be formed using many types of substrate as long as the substrate provides electrons at the correct energy level. For congruent films of the

Cu₂Sb, the metallic substrates that are not highly passivated to electrochemistry yield the best results. Hence we are confident that the speciation of the solution plays a critical role in the single potential deposition of crystalline Cu₂Sb.

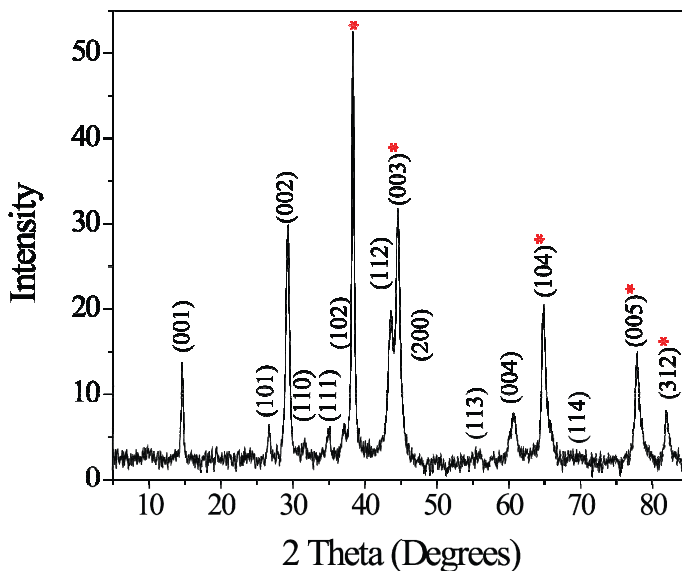


Figure 4.9: Powder XRD pattern of Cu₂Sb film deposited on a gold substrate using optimized deposition solution and conditions. The red stars indicate the gold substrate diffraction peaks, the other peak are indexed for Cu₂Sb PDF 01-085-0492.

With a procedure that allows crystalline copper antimonide to be electrodeposited at a single potential, the next steps in achieving the goals of this research are to deposit nanowires of copper antimonide and perform lithiation studies on the electrodeposited Cu₂Sb materials. The electrodeposition of nanowires of Cu₂Sb will be covered in Chapter 6 while the battery testing will covered in Chapter 9. In order to perform the battery testing of Cu₂Sb thin films, numerous films of Cu₂Sb were needed. Following the procedure given in this chapter this would require mechanically polishing the copper substrate before electrodepositing each Cu₂Sb film. This quickly becomes time intensive as the mechanical polishing of one film requires over 45 minutes of polishing. To reduce

the amount of time required to deposit one film of Cu_2Sb the procedure was modified to deposit on copper substrates that were not mechanically polished.

While congruent films were obtained electrodepositing Cu_2Sb out of room temperature solutions, the crystallinity of the films suffered. While the impact that the crystallinity of the copper antimonide films has on the battery performance is not known, the need of having good crystallinity to aid in the material characterization during the charge and discharge of the material is important. Figure 4.10a is an XRD pattern of a Cu_2Sb film deposited using the same conditions used previously except the copper substrate was not mechanically polished prior to the deposition. The decrease in crystallinity is clear from the absence of most diffraction peaks that correspond to Cu_2Sb . To alleviate this problem, Cu_2Sb films used for the battery testing discussed in Chapter 8 and 9 were deposited from solutions at $55\text{ }^\circ\text{C}$. Figure 4.10b contains a XRD pattern of a Cu_2Sb deposited onto a non-polished Cu_2Sb film from solutions at $55\text{ }^\circ\text{C}$. Comparing the diffraction patterns in Figure 4.10 it can be seen that as temperature increases, a concomitant improvement in the crystallinity is observed, although the crystallinity is not as good as seen with mechanically polished copper substrates (Figure 4.6).

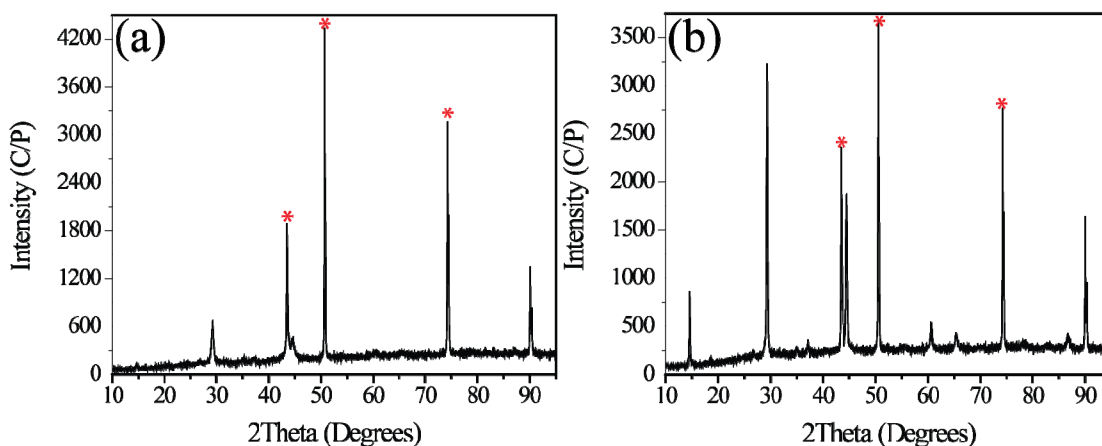


Figure 4.10: XRD patterns of Cu_2Sb films deposited for ten minutes using copper foil substrates not mechanically polished at (a) room temperature, and (b) $55\text{ }^\circ\text{C}$. The red stars indicate the gold substrate diffraction peaks, the other peak are indexed for Cu_2Sb PDF 01-085-0492.

4.6 Conclusion

Copper antimonide films were deposited electrochemically from an aqueous solution and at a single reduction potential. This was achieved by using the optimized solution conditions discussed in Chapter 3 and carefully examining the effect that the deposition parameters had of the resulting film. First, it was determined that deposition at -1050 mV produce highly crystalline films with the correct atomic ratios for Cu_2Sb . Second, we found that the crystallinity of the electrodeposited Cu_2Sb increased with an increase in the temperature. Third, it was found that Cu_2Sb could be deposited onto most substrates. Good sticking of the deposited Cu_2Sb forming thin films was found to occur on only non-passivated metallic substrates. It was also determined that the smoothness of the substrate affects the crystallinity of the deposited film. The films deposited are relatively free of impurities and are of high crystalline compared to Cu_2Sb samples that have been prepared using other literature methods. Thus, the electrodeposition procedure discussed in this chapter fulfills the requirements for a procedure that is needed for

depositing films and nanowire arrays of Cu₂Sb directly onto the current collector for battery testing.

4.7 References

- (1) Vaughey, J. T.; Johnson, C. S.; Kropf, A. J.; Benedek, R.; Thackeray, M. M.; Tostmann, H.; Sarakonsri, T.; Hackney, S.; Fransson, L.; Edstrom, K.; Thomas, J. O. *Journal of Power Sources* **2001**, 97-8, 194.
- (2) Johnson, C. S.; Vaughey, J. T.; Thackeray, M. M.; Sarakonsri, T.; Hackney, S. A.; Fransson, L.; Edstrom, K.; Thomas, J. O. *Electrochemistry Communications* **2000**, 2, 595.
- (3) Thackeray, M. M.; Vaughey, J. T.; Johnson, C. S.; Kropf, A. J.; Benedek, R.; Fransson, L. M. L.; Edstrom, K. *Journal of Power Sources* **2003**, 113, 124.
- (4) Thackeray, M. M.; Vaughey, J. T.; Fransson, L. M. L. *Jom-Journal of the Minerals Metals & Materials Society* **2002**, 54, 20.
- (5) Fransson, L. M. L.; Vaughey, J. T.; Edstrom, K.; Thackeray, M. M. *Journal of the Electrochemical Society* **2003**, 150, A86.
- (6) Fransson, L. M. L.; Vaughey, J. T.; Benedek, R.; Edstrom, K.; Thomas, J. O.; Thackeray, M. M. *Electrochemistry Communications* **2001**, 3, 317.

CHAPTER 5

NUCLEATION PROCESSES INVOLVED IN THE SINGLE POTENTIAL DEPOSITION OF Cu_2Sb

Some of the text contained in this chapter consists of an article that appears in: Mosby, J. M.; Johnson, D. C.; Prieto, A. L. *Journal of the Electrochemical Society* **2010**, 157, 5, #.

5.1 Microscopy studies of electrodeposition nucleation

In the last two chapters of this thesis a procedure was developed for the single-potential deposition of Cu_2Sb from aqueous solutions to obtain crystalline thin films.¹ My interest in electrodepositing Cu_2Sb is to use it as an anode material for secondary lithium-ion batteries: the composition and crystal structure are critical for the desired physical properties. While the optimized deposition solution and parameters developed for the electrodeposition of Cu_2Sb deposits Cu_2Sb films with the correct composition and crystal structure, the parameters still need to be optimized for the deposition of nanowires. Also, a deeper understanding of the electrodeposition procedure for this compound would be useful for extending this technique to other crystalline intermetallics with diverse electronic applications.

Control over the morphology and crystallinity of electrodeposited materials is known to be a function of the nucleation and subsequent growth.² In addition, the competition between nucleation and growth also determines the grain size of the deposited material, which can lead to significant differences in the physical properties.³ For these reasons, the nucleation and growth of metal deposits have been studied extensively using a variety of microscopy techniques such as atomic force microscopy (AFM), scanning electron microscopy (SEM), and transmission electron microscopy (TEM). An added complexity arises for the deposition of intermetallics, semiconductors and alloys as opposed to the electrodeposition of single elements because the composition, crystallinity, and morphology depend not only on the nucleation and growth, but on the reduction potential of the different constituents being co-deposited. It is imperative to be able to investigate the crystal structure, composition, and morphology

during the nucleation and growth of multi-element materials with high spatial resolution in order to develop a deeper understanding of the deposition mechanism.

One example that has provided a wealth of information is the investigation into the time-dependent nucleation and growth of electrodeposited copper. AFM, SEM, and TEM studies on the electrodeposition of copper have contributed to the development of various models for the nucleation and growth processes that occur during electrodeposition.^{2,4-10} Specifically, it is common to use the previously mentioned microscopy techniques to determine whether the deposition can be modeled by either instantaneous or progressive nucleation. The information gathered from these types of studies has led to a higher degree of control over the deposition process, thereby facilitating the synthesis of deposits with desired physical and mechanical properties. For example, *in-situ* AFM was used to examine the effect of Cu^{2+} concentration, potential, pH, and additives on the resulting deposition. It was observed that the pH dictated whether the nucleation was instantaneous or progressive.¹¹ In electrodeposition instantaneous nucleation corresponds to the case where all of the nucleation occurs at the same time; followed by growth of the nucleation sites already present. Progressive nucleation corresponds to the case where nucleation occurs throughout the deposition, so the number of nucleation sites increase with time. In another case, Radisic *et al.* used real time *in-situ* TEM to demonstrate that the electrodeposition of copper fit first-order nucleation kinetics.² It was also determined that under the deposition conditions examined, the nucleation could not be described by either the instantaneous or progressive model inclusively.² These are just two instances where microscopy techniques have been used to improve the understanding of nucleation and growth of

electrodeposited metals. Although the electrodeposition of copper has received the majority of the attention, the information gained from these experiments provides a starting point for the electrodeposition of other metals. It is not as common, however, to use microscopy techniques such as these to investigate the electrodeposition of multi-element materials because the focus has traditionally been on the relative deposition efficiencies of the individual elements.

For the electrodeposition of multi-element materials, the concentration of the precursors and deposition potential are known to be the two most important conditions affecting the material properties.^{12,13} Improved control over the electrodeposition of intermetallics, semiconductors and alloys is still needed because of increased use in electronic applications. These applications require a high degree of control over the electrodeposition in order to be used for device fabrication. For this control to be realized, the processes that occur during nucleation need to be determined. For many cases in the literature, the electrodeposition of multi-element materials occurs by either anomalous codeposition (ACD) or induced under potential deposition (IUPD).¹²⁻¹⁵ Both ACD and IUPD involve first the deposition of one element followed by, and/or accompanied by, the deposition of the second element.¹⁴ Specifically, ACD occurs when the less noble metal is deposited preferentially to the other metal. This can result in the deposited material having a stoichiometry not consistent with the current density of each element depositing individually. In contrast, IUPD describes the case where the deposition of one element allows for the deposition of a second element that otherwise would not deposit for the given deposition conditions.¹⁴ This is also thought to be the route by which multi-element semiconductors are electrodeposited.¹⁵ One example

where a microscopy technique has been used to analyze the nucleation of a mixed element deposition is reported by Han *et al.*¹⁶ Although it was determined that the co-deposition of Sn-Cu followed the progressive nucleation model, a connection between the nucleation model and ACD or IUPD was not presented.¹⁶

As discussed in the previous chapters, a method to electrodeposit crystalline Cu₂Sb from aqueous solutions at a single-potential has been developed.¹ To accomplish this, citric acid was used as a complexing agent to force the Sb³⁺ into non-acidic aqueous solutions. After the pH was adjusted to 6, it was found that Cu₂Sb could be deposited at a single-potential, -1050 mV vs. SSCE, while at more acidic or basic conditions this was not the case. See the previous two chapters for more complete description. The dependence of the deposition on pH is thought to be due to the speciation playing an important role in the deposition. It was not, however, determined whether the material deposited directly as Cu₂Sb or if the deposition followed a route similar to ACD or IUPD. This information is vital if single-potential deposition procedures similar to the one used for Cu₂Sb can be applied to the deposition of other intermetallics, semiconductors, or alloys. To this end, Cu₂Sb has been deposited directly onto TEM grids allowing the nucleation process to be studied along with changes in the composition, crystallinity, and morphology. The results presented here are the first direct evidence illustrating how a deposition similar to ACD or IUPD proceeds during the first stages of nucleation and growth for a crystalline intermetallic. It was observed that within the first second of the deposition, the nucleation sites transition through multiple compositions and crystal structures before forming Cu₂Sb, providing evidence that the solution chemistry is not solely responsible for the single potential deposition of Cu₂Sb. These findings

demonstrate the applicability of TEM coupled with selected area electron diffraction (SAED) and energy-dispersive X-ray spectroscopy (EDS) as an analytical tool to probe the nucleation and growth of multi-element electrodeposited materials. Further studies of the electrodeposited Cu_2Sb on TEM grids will also provide an unhindered investigation of the crystal structure, composition, and morphology changes that occur during the lithiation and de-lithiation of the material as an anode for lithium ion batteries and will be discussed in Chapter 8. This is in contrast to traditional studies where the anode or cathode material is combined with a binder consisting of carbon and a polymer which cannot be subsequently removed after the lithiation or de-lithiation process.¹⁷⁻²²

5.2 Experimental procedures

All electrodeposition baths consisted of aqueous 0.4 M citric acid solutions (99.5% Aldrich) containing 0.025 M antimony(III) oxide (nanopowder, 99.9+% Aldrich) and 0.1 M copper(II) nitrate hemipentahydrate (99.9+% Aldrich). A detailed preparation procedure has been reported previously.¹ Briefly, citric acid was added to Millipore[®] water (18 Ω) followed by the addition of Sb_2O_3 . After dissolution of Sb_2O_3 , the $\text{Cu}(\text{NO}_3)_2$ was added. The solution pH was then adjusted to 6 using 5 M potassium hydroxide (ACS certified), and the depositions were carried out at 50 °C to increase the crystallinity of the final product so that SAED analysis could be used more effectively. Cu_2Sb was deposited potentiostatically using a Gamry Reference 3000 controlled by the Gamry Framework version 5.56 software. The depositions were performed using a three-electrode cell consisting of a Pt mesh flag as the counter electrode and a SSCE as the reference electrode. Cyclic voltammograms (CVs) were performed on a platinum disk electrode purchased from BASi (2.01 mm²) and gold TEM grids with a geometric area of

(7.3 mm²). For the chronoamperometry plot, a copper flag (0.25 mm thick, 99.98% Aldrich) and a TEM grid with copper mesh were used as the working electrode. The analyses performed on the nucleation and growth of Cu₂Sb were conducted by directly depositing the material onto TEM grids while using the grids as the working electrode. Carbon composite TEM grids with copper 200 mesh were purchased from Structure Probe, Inc. (SPI) were used to analyze the nucleation, growth, and changes in crystal structure, while indexed TEM grids with gold 200 mesh (SPI) were used to collect EDS spectra as gold is not an element contained in the deposition product. An optical microscope image of a TEM grid with gold mesh is shown in the inset of Fig. 1. The 95- μ m square holes and 20 μ m bars which make up a 200 mesh TEM grid can clearly be seen. The carbon composite (conducting polymer film blended with carbon fibers)²³ can also be seen within the 95 μ m square holes of the grid.

The Optical microscope image of the TEM grid was taken on an Olympus BX52 equipped with a polarizer (model # U-AN360-3) using an Olympus UMPlanF1 lens with a magnification of 10x. A QColor5 Olympus camera was used to obtain digital images using the software QCapture Pro. version 5.1.1.14. High resolution transmission electron microscopy (HRTEM) and SEM images, SAED patterns, and EDS spectra were collected after washing the TEM grids with excess water and methanol. TEM-EDS and SAED data were collected using a Philips CM200 STEM equipped with a Princeton Gamma Tech Prism 2000 energy-dispersive spectrometer operating at an accelerating voltage of 200 kV. SEM-EDS analyses were performed using a JEOL JSM-6500F equipped with a Thermo Electron energy-dispersive spectroscopy detector with an applied voltage of 10

kV. The particle sizes were determined by counting at least 300 particles from a particular deposition time, from multiple regions of a SEM or TEM image.

5.3 Electrodeposition of Cu_2Sb onto TEM grids

For the present study CVs of the deposition solution were taken using TEM grids as working electrodes (WE) and are shown in Figure 5.1. Comparing the platinum WE (Figure 5.1a) to the TEM WEs (Figure 5.1a & b), the reduction peaks on TEM WE were shifted slightly in the negative direction while the corresponding oxidation peaks are shifted in the positive direction. This shift in potentials and slight difference in peak shape indicates the conductivity of the TEM WEs is less than the conductivity of the platinum disk electrode. This is not surprising considering the crystallinity of the platinum WE is much higher than the metals and carbon composite of the TEM WEs.

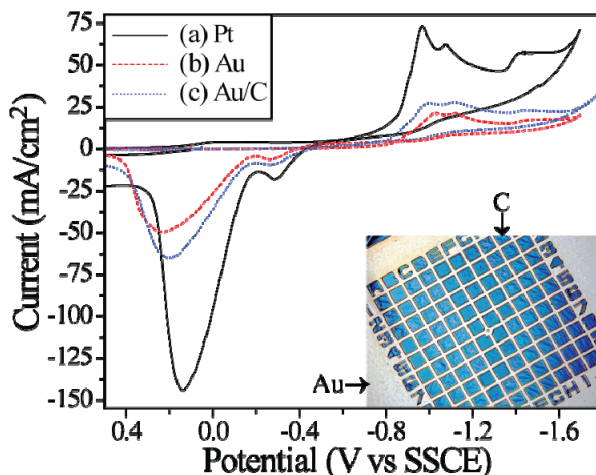


Figure 5.1: CVs ran at 250 mV s^{-1} in deposition solution performed on: **(a)** platinum slug, **(b)** TEM grid with gold mesh but no carbon composite, and **(c)** TEM grid with both the gold mesh and carbon composite. The aqueous solution contained 0.05 M Sb^{3+} , 1.0 M Cu^{2+} , and $0.4 \text{ M citric acid}$ at a pH of 6. The inset is an optical microscope image of a TEM grid with gold mesh and the carbon composite.

CVs were also taken on TEM grids with copper mesh, but are not shown because the oxidation of copper starts to occur at a potential similar to the oxidation of Cu_2Sb .

The reduction peaks on the TEM electrodes with copper mesh are similar to those shown in Figure 5.1b & c. SPI reports that the TEM grids are 55% open space, which is the main cause for the lower current density seen in the CVs taken with the TEM WE. While the CV in Figure 5.1b was performed on a TEM grid in which the carbon composite was removed and thus has the lowest current density, it was not 55% lower than the TEM grid with the carbon composite (Figure 5.1c). This indicates that the carbon composite conductivity is much lower than the mesh material (i.e. gold) of the TEM grid. This is also evident from depositions carried out on TEM WEs as the mesh material has a higher packing density of Cu₂Sb than the carbon composite at short times. This is beneficial for this study because it allows the nucleation sites to be analyzed on the carbon composite at times that do not cause difficulties experimentally. The implication is that the times reported here are not quantitative representations of the Cu₂Sb depositions carried out on a “normal” electrode, but instead are used to chronologically describe the events that occur during the early stages of the single-potential deposition of Cu₂Sb.

5.4 Chronoamperometry

Electrodeposition of Cu₂Sb from aqueous citrate solutions containing Cu²⁺ and Sb³⁺ in a ratio of 2:1 at a potential of -1050 mV vs. SSCE leads to a high nucleation density at time periods less than 1 s. A comparison of the dimensionless current transients between Cu₂Sb electrodeposition and the theoretical models developed by Scharifker and Hills for instantaneous nucleation (Eq. 5.1) and progressive nucleation (Eq. 5.2) is plotted in Figure 5.2.²⁴

$$\frac{i^2}{i_m^2} = \frac{1.9542}{\frac{t}{t_m}} \left\{ 1 - \exp \left[-1.2564 \left(\frac{t}{t_m} \right) \right] \right\}^2 \quad [5.1]$$

$$\frac{i^2}{i_m^2} = \frac{1.2254}{\frac{t}{t_m}} \left\{ 1 - \exp \left[-2.3367 \left(\frac{t}{t_m} \right)^2 \right] \right\}^2 \quad [5.2]$$

Here i_m corresponds to the current at the time for which the derivative of the current with respect to time is zero (t_m). Figure 5.2a clearly illustrates that at short t/t_m the deposition of Cu_2Sb onto copper foil (\square) and TEM grids with copper mesh (Δ) follow the instantaneous nucleation model. It should be noted that a slight deviation between the two plotted current transients is observed. This is a consequence of depositing onto a TEM grid, as stated the Cu_2Sb is depositing onto two different surfaces of varying conductivity—the copper or gold mesh of the TEM grid and the carbon composite film between the mesh. Regardless of the deposition substrate, the experimental data deviates from both the instantaneous and progressive nucleation models after $t/t_m > 1$. A known cause of the observed deviation from the theoretical models is hydrogen evolution, which is substrate dependent because the rate of $\text{H}_2(\text{g})$ evolution is a function of the electrode material.⁹ Hydrogen evolution must be considered in this system as well and will occur at very different rates on the carbon composite compared to the mesh of the grid.³

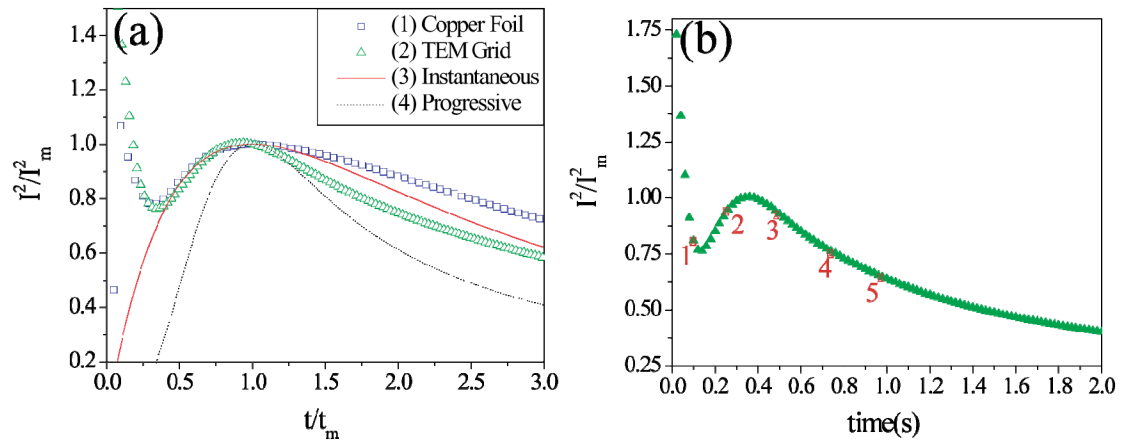


Figure 5.2: (a) Dimensionless current versus dimensionless time curves for the deposition of Cu_2Sb at a potential of -1050 mV vs. SSCE for the following: (1) copper foil and (2) carbon composite of a TEM grid as well as calculated curves for (3) instantaneous and (4) progressive nucleation using Eq. 1 and 2, respectively. (b) Dimensionless current versus time for Cu_2Sb deposition on a carbon composite of a TEM grid. Numbered red triangles indicate the deposition times studied via TEM, SAED, and EDS.

5.5 Scanning electron microscopy

Additional evidence that the nucleation of Cu_2Sb is instantaneous can be found by evaluating representative low magnification SEM images. Figure 5.3a contains a SEM image of Cu_2Sb after a 5 s deposition onto the carbon composite of a TEM grid and shows a nucleation density of 4.8 sites per square micrometer. Comparing this image to Figure 5.3b, which is an image of a 30 s deposition with a nucleation density of 5.0 sites per square micrometer, it is apparent that the number of sites does not significantly increase between the two times, but instead separate nucleation sites have started to merge. This process is the probable cause for the large size distribution observed at longer deposition times. As the deposition time proceeds, the diameter of the nucleation sites increases where measurements taken at 0.5 s, 5 s, and 30 s show diameters of 79 ± 15 nm (image not shown), 223 ± 40 nm (Figure 5.3a), and 395 ± 133 nm (Figure 5.3b),

respectively. Overlapping of the nucleation sites starts to occur after depositing for 30 s (Figure 5.3b), and a 45 s deposition results in merged nucleation sites creating micron-sized islands of deposited material with a cubic morphology (Figure 5.4a). This morphology is consistent with the morphology observed for Cu_2Sb deposited on the mesh part of the TEM grids and films deposited on metal foil substrates shown in Figure 4.5.

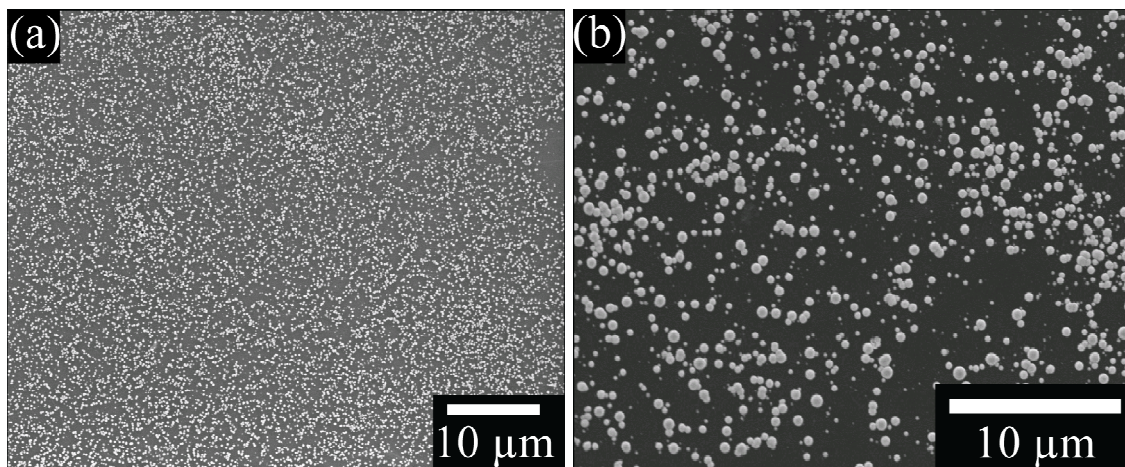


Figure 5.3: (a) SEM image of a 5 s Cu_2Sb deposition on a carbon composite of a TEM grid demonstrating an average particle size of 223 ± 40 nm. (b) SEM image of a 30 s deposition on a carbon composite of a TEM grid demonstrating an average particle size of 395 ± 133 nm.

A significant advantage to depositing onto TEM grids is that the nucleation sites can be imaged from both the front and the back of the grid using SEM, and can be analyzed from both sides as well using EDS. The nanometer thick carbon composite film is acting essentially as a transparent growth substrate, allowing the analysis of the interface between the Cu_2Sb and the growth substrate. A representative image of the nucleation sites imaged through the carbon film for a 45 s deposition is shown in the inset of Figure 5.4a. Separating the nucleation sites from the bulk material is a low-density region that manifests as a dark ring in the SEM images. This contrast difference can be readily observed in the SEM image shown in the inset of Figure 5.4b. In order to determine if

the composition of the nucleation sites and that of the bulk material is equivalent, EDS elemental mapping analysis was performed on an area surrounding a single nucleation site. A representative SEM image is contained in the inset of Figure 5.4b. Two distinct phases are overlaid in false color on the SEM image as seen in Figure 5.4b. The only elements found to be present in measurable quantities were carbon (due to the carbon composite associated with the TEM grid), copper and antimony. The first phase, represented as blue in Figure 5.4b, is copper rich and is mainly associated with the nucleation site. The second phase, represented as orange, is antimony rich and is associated with the low-density ring separating the nucleation site from the bulk material. The phase analysis shows that both phases are present in roughly the same amount in the bulk material. SAED analysis confirms that crystalline Cu_2Sb is present at this deposition time. We suspect that instead of there being equal amounts of the copper rich and antimony rich phases present (which would result in the overall 2:1 Cu:Sb stoichiometry). The hypothesis is that there is a copper rich phase that forms at the initial nucleation site. This phase is separated from the bulk Cu_2Sb by an antimony rich phase. The EDS spatial resolution is not high enough to distinguish the bulk Cu_2Sb as a third phase with the appropriate stoichiometric ratio of copper to antimony. TEM-SAED analyses were performed at various deposition times in order to provide higher spatial resolution data.

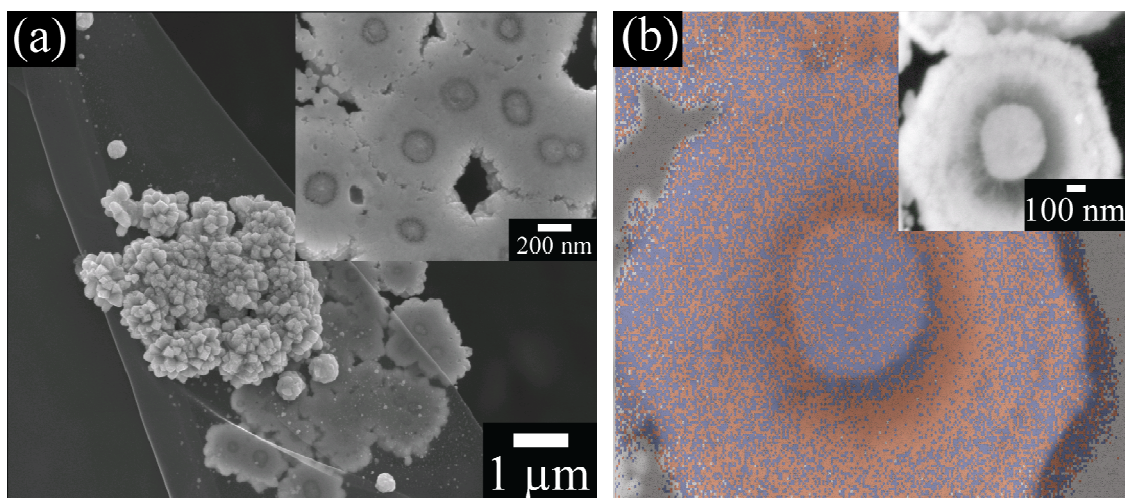


Figure 5.4: (a) SEM image of Cu_2Sb deposited for 45 s at -1050 mV on a carbon composite of a TEM grid. Inset contains a higher magnification image of the back of the deposit. (b) EDS mapping image with false color overlaid onto an SEM image of the back of a single nucleation site of Cu_2Sb imaged through the transparent carbon composite film of a TEM grid. The orange phase is antimony rich, i.e. Cu_{2-x}Sb , while the blue phase is copper rich, Cu_{2+x}Sb . The inset is the SEM image without the elemental overlay.

5.6 Transmission electron microscopy

After applying -1050 mV vs. SSCE for 0.1 s, the carbon composite on the TEM grid contains a large number of nucleation sites. However, the density of nucleation sites is not uniform, and we observed that there is an even distribution covering the carbon composite film (Figure 5.3) in some grid windows, while other grid windows show areas of high nucleation density separated by low density regions (images not shown). This is most likely due to the fact that the carbon composite associated with the TEM grids are not uniform and thus have localized variations in electrical conductivity, resulting in varying current densities during the depositions. SPI reports the thickness of the carbon composite being $35 \mu\text{m}$ with a variation of $\pm 10 \mu\text{m}$. Regardless, lattice fringes with a measured separation of 2.2 \AA , corresponding to (110) planes of antimony (PDF 01-073-5920), are present in HRTEM images of single nucleation sites after a 0.1 s deposition

(Figure 5.5a). Further analysis of the image reveals that lattice fringes are not visible over the entire site for a single zone axis. Also, the contrast difference observed within a single nucleation site alludes to there being either composition or thickness differences. These two observations suggest that the nucleation sites are polycrystalline. This conclusion is supported by the SAED pattern indexed to antimony in the inset of Figure 5.5a. For a deposition time of 0.25 s, the nucleation sites have grown in size and continue to be polycrystalline, as illustrated in Figure 5.5b. In addition to the increased size, a transition occurs as the measured lattice spacing decreases to 1.8 Å, which is indicative of copper (200) planes (PDF 01-071-4608), not antimony. A representative SAED pattern of the nucleation sites for 0.25 s deposition is shown in the inset of Figure 5.5b and confirms the presence of polycrystalline copper.

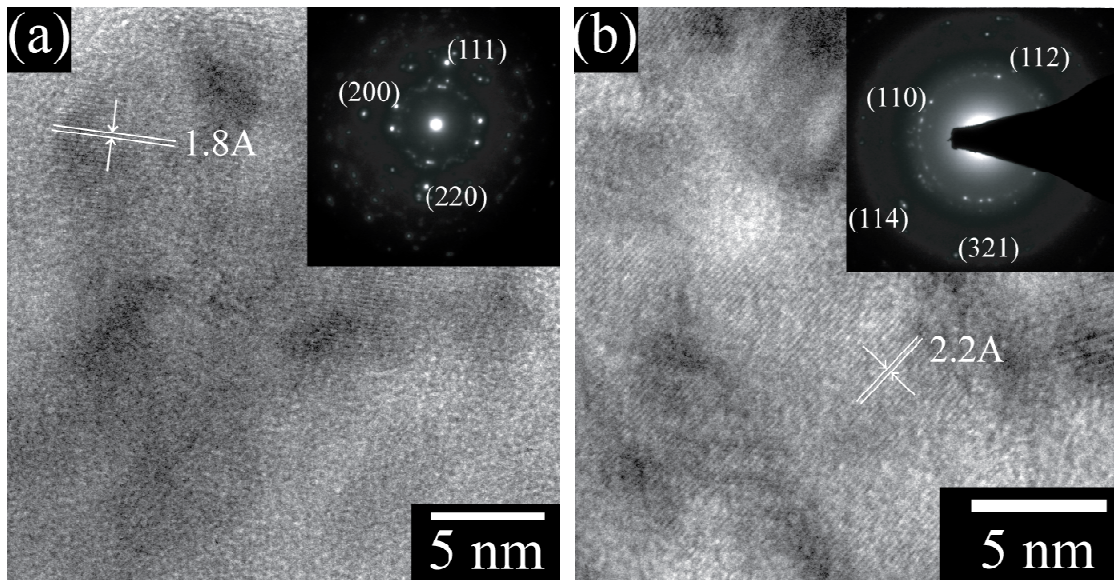


Figure 5.5: (a) TEM image of a nucleation site after a 0.1 s deposition on a carbon composite of a TEM grid at -1050 mV. The measured lattice spacing of 2.2 Å has been assigned to antimony (110). The inset is a SAED pattern of the nucleation site that has been indexed to antimony. (b) TEM image of a nucleation site after a 0.25 s deposition on a carbon composite of a TEM grid at -1050 mV. The measured lattice spacing of 1.8 Å is a match for copper (200). The inset contains a SAED pattern of the deposition site that has been indexed to copper.

At a deposition time of approximately 0.5 s, the nucleation sites go through a morphological and phase change as they become circular and increasingly less crystalline, as evidenced by the lack of intense diffraction spots shown in Figure 5.6a. The diffuse diffraction rings, however, still index to copper. This indicates that the nucleation sites are much less ordered than the sites at earlier deposition times. At deposition times longer than 0.75 s, SAED patterns of the deposit indicate that crystalline Cu_2Sb (PDF 01-085-0492) has formed. A representative TEM image of a nucleation site after depositing for 1 s onto a TEM grid is shown in Figure 5.6b with its corresponding SAED pattern. This data suggests that the circular nucleation sites with a lack of good long range order observed at 0.5 s are going through a transformation to crystalline Cu_2Sb as the deposition time is increased. Because the SAED pattern of the nucleation sites at early stages of the deposition indicate that transitions in the structure of the deposited material are occurring, we used EDS analysis to probe the compositional changes occurring as a function of time.

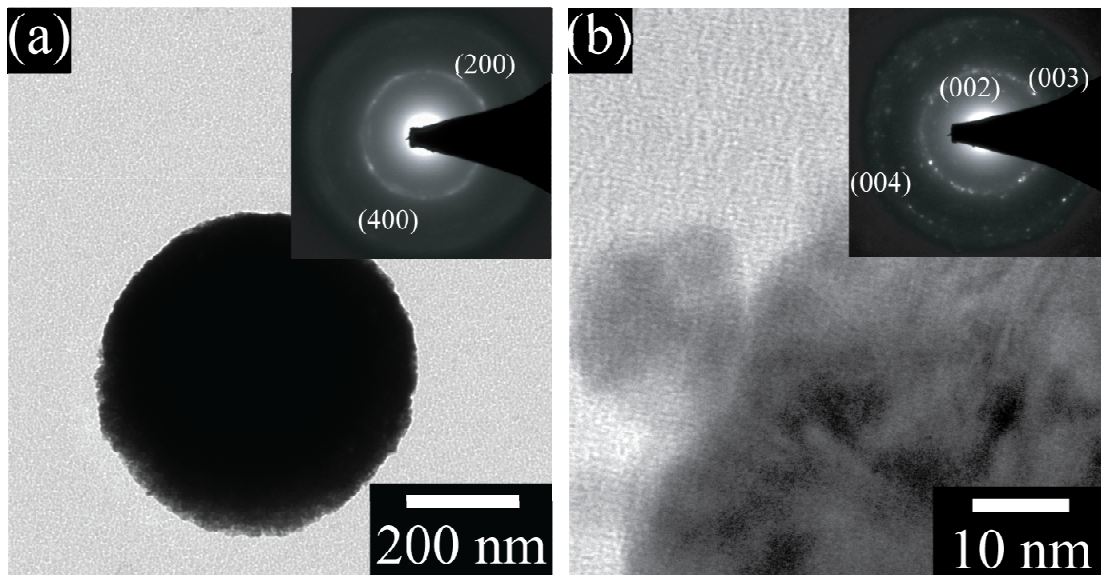


Figure 5.6: (a) TEM image of a nucleation site after a 0.5 s deposition on a carbon composite of a TEM grid at -1050 mV. The inset contains a SAED pattern of the deposition site indexed to copper. (b) TEM image of a nucleation site after a 1 s deposition on a carbon composite of a TEM grid at -1050 mV. The inset is a SAED pattern of the site that has been indexed to Cu_2Sb .

To eliminate potential false signals from TEM grids with copper mesh material, the EDS spectra were collected from samples deposited on the carbon composite of TEM grids with gold mesh. While a standard was not used to quantify the EDS data, qualitatively large compositional changes are observed during the first 1 s of the deposition. Depositions lasting between 0.1 s and 0.75 s are composed of excess copper versus antimony relative to the 2:1 atomic ratio one would expect if Cu_2Sb were deposited directly from solution. Figure 5.7a contains a representative EDS spectrum taken from a 0.1 s deposition showing the presence of antimony; thereby confirming the analysis of the SAED pattern. The EDS spectrum, however, also indicates the presence of significant amount of copper. After a 0.25 s deposition, the EDS spectrum of a nucleation site (Figure 5.7b) illustrates the comparative absence of antimony when compared to copper, suggesting that the nucleation site is composed of mostly copper. The EDS of a deposition performed for 1 s, however, contains clear peaks for both

copper and antimony, as shown in Figure 5.7c. Utilizing the results from all of the analytical techniques presented here—cyclic voltammetry, chronoamperometry, SEM, TEM, EDS, and SAED—the processes that occur during the deposition of crystalline Cu_2Sb from solution will now be discussed.

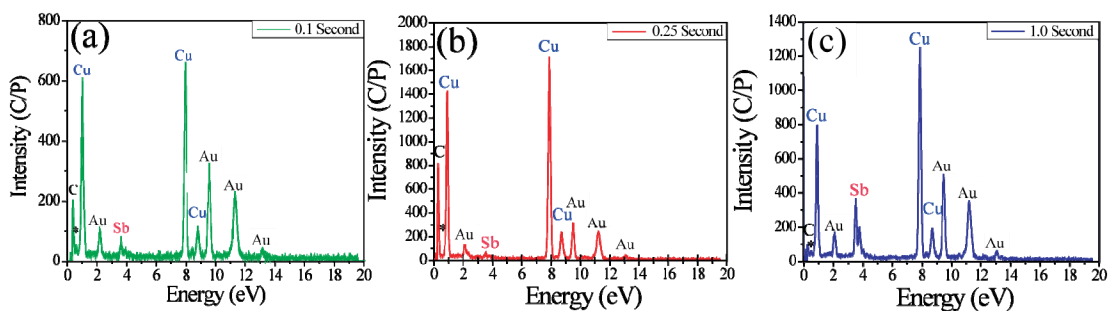


Figure 5.7: EDS spectra of nucleation sites deposited onto carbon composite of a TEM grid with gold mesh for (a) 0.1 s, (b) 0.25 s, and (c) 1 s. The peaks associated with copper, antimony, and gold, which is due to the TEM grid, are labeled in blue, red, and yellow, respectively. The carbon from the TEM grid is labeled in black and the miniscule oxygen peak is identified with an asterisk.

5.7 Discussion

The results presented in this chapter provide chronological details regarding the single-potential deposition of Cu_2Sb . For a deposition time of 0.1 s, the dimensionless current transients are exponentially decreasing due to the double layer capacitance as represented by point 1 in Figure 5.2b. The TEM images collected from samples for this deposition time illustrate that the substrate is populated with nucleation sites. TEM and SAED evidence contained in Figure 5.5a indicate that the sites are polycrystalline antimony. Contrary to this, EDS spectra of the nucleation sites, for which a representative spectrum is contained in Figure 5.7a, clearly show a higher atomic percent of copper when compared to antimony. This can be attributed to the presence of amorphous copper distributed within the sites since copper is not observed in the SAED patterns. In the previous chapter it was reported that copper rich films (determined by X-

ray photoelectron spectroscopy) were deposited at potentials more positive of -1050 mV vs. SSCE. It is possible that at early times the IR drop cause by the current from the double layer charging is changing the potential at the solution electrode interface. This would cause the potential to be positive of -1050 mV vs. SSCE, and thus form a copper rich film. The unconventional sharp increase in current seen in the CVs in Figure 5.1 at -1000 mV can be described by a nucleation site of antimony acting as an activation site for the over potential deposition of copper. As soon as the antimony site is present the copper deposition begins and the rate of the copper deposition increases dramatically.

Referring back to the dimensionless current versus time curve in Figure 5.2b, point 2 corresponds to a deposition time of 0.25 s, which is located immediately before the curve maximum. For this deposition time, the nucleation sites are polycrystalline, but TEM and SAED evidence overwhelmingly supports the fact that copper is the dominant crystalline species present (Figure 5.5b). As in the 0.1 s deposition, the EDS data (Figure 5.7b) continue to show a higher atomic percent of copper when compared to antimony if Cu_2Sb were the only species present. Again, because the current is still higher than at times when the deposition is diffusion limited, the excess copper could be attributed to higher deposition rate for copper as it is at a over potential deposition. It is clear, however, that the nucleation sites contain detectable amounts of antimony even though the element is not observed in the SAED patterns. This could be due to the fact that (1) the antimony has transitioned to an amorphous phase, or (2) the antimony is still crystalline, but the large discrepancy in the atomic percent, which favors copper, overwhelms the diffraction signal from antimony making it unobservable. The conclusion based on the data collected from samples deposited at 0.1 s and 0.25 s is that

polycrystalline antimony is deposited first and subsequently acts as an activation site for the deposition of copper. This is schematically shown in Figure 5.8, and is further supported by the previous study discussed in Chapter 2, as copper metal does not deposit without the antimony species being present in solution.

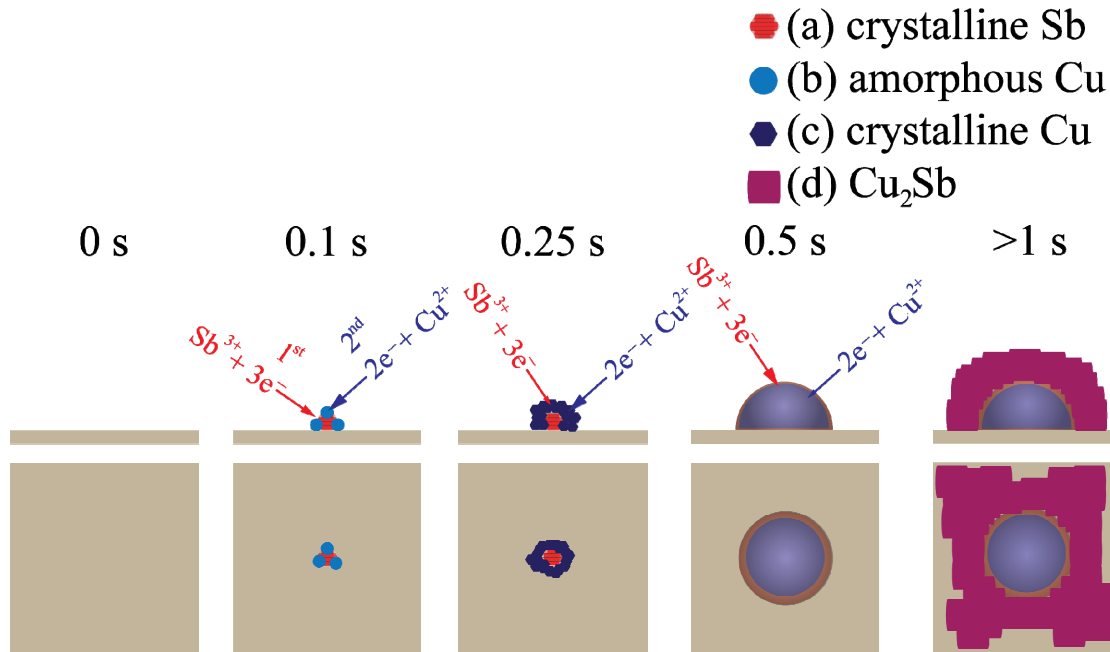


Figure 5.8: Schematic of the processes that occur during the deposition of Cu₂Sb. The different phases are shown for the times that the nucleation sites were examined in the text. The arrow size represents the relative rates at which the two reductions are occurring. At 0.1 s the sites start off with (a) polycrystalline antimony dispersed in (b) amorphous copper. After 0.25 s the sites then transition to mostly (c) polycrystalline copper, which by 0.5 s goes through a further transition to an amorphous site. After 0.75 s (d) Cu₂Sb starts to grow.

After antimony acts as an activation site for the deposition of copper, the deposition sites undergo a phase transition at a deposition time of approximately 0.5 s in which the crystallinity of the nucleation sites dramatically decreases, as illustrated in Figure 5.6a. With respect to the dimensionless current transient curve in Figure 5.2b, a 0.5 s deposition (point 3) occurs after the maximum when neglecting the data points due to the double layer. As the nucleation site transitions further into crystalline copper, the

deposition rate for the copper decreases as antimony is required for the copper over potential deposition. The deposition rate of antimony then exceeds that of copper and the nucleation site becomes a solid solution of antimony and copper instead of polycrystalline copper. This results in the amorphous properties observed in the TEM images and SAED patterns. As the deposition time increases from 0.5 s to 0.75 s (Figure 5.2b point 4), the nucleation sites begin to transition to the final deposition product, crystalline Cu_2Sb (Figure 5.8). The effect of the IR drop on the applied potential at times greater than 0.75 s is small and relatively constant. Once the transformation to Cu_2Sb is initiated, the crystallinity of the deposited material increases with an increase in deposition time, as evidence by the SAED pattern indexed to Cu_2Sb contained in Figure 5.6b. The presence of the amorphous phase and the deposition being diffusion limited results in the deposition of Cu_2Sb instead of the individual elements. It is reassuring to know that even though the deposition occurred onto the carbon composite of TEM grids, the deposited Cu_2Sb had the same preferred orientation that was obtained with thin films deposited on copper foil. As the deposition time reaches 1 s and longer, the nucleation sites have transitioned to polycrystalline Cu_2Sb and the growth of the bulk material continues without an indication that anything but Cu_2Sb deposits.

The behavior observed in the deposition of Cu_2Sb from solution can be described using the instantaneous nucleation coupled with both the ACD the IUPD model that have been previously postulated for the electrodeposition of alloys and semiconductors.¹²⁻¹⁵ As suggested by the data presented above, the nucleation sites are instantaneously deposited as polycrystalline antimony with amorphous copper. The presence of Cu^{2+} allows the deposition of antimony to occur at more positive potentials than otherwise

expected. However, as soon as antimony is deposited the deposition of the nobler element begins. As the deposition time increases, the individual elements, copper and antimony, undergo additional transformations finally resulting in the desired product, polycrystalline Cu_2Sb ; which continues to deposit as the deposition becomes diffusion limited. Since the polycrystalline antimony observed at a deposition time of 0.1 s is acting as an activation site for the subsequent copper deposition and formation of Cu_2Sb , it is not unexpected that the dimensionless current transients contained in Figure 5.2 can be fitted to the instantaneous nucleation model. These observations and the data reported here suggest that the single-potential deposition of Cu_2Sb is occurring through a mix of ACD and IUPD at early times. As antimony is deposited at an underpotential in the presence of Cu^{2+} , and copper deposition is induced by the nucleation site created by the less nobler element. However, we cannot yet determine if the excess copper deposited at approximately 0.5 s causes the transition to Cu_2Sb through solid state diffusion or if the morphology and elemental composition of the nucleation sites at this time along with the deposition being diffusion limited result in the direct deposition of Cu_2Sb out of solution for all deposition times greater than 0.5 s.

5.8 Proposed deposition mechanism based on solution chemistry and nucleation processes

With the processes that occur between the substrate and deposited material investigated, the deposition mechanism will be refined from Chapter 3. Considering the work presented in Chapter 3, the current of the reduction peaks for the different solutions at pH 6 versus the square root of the scan rate are plotted in Figure 5.8. Two important trends are clear. First, the current for the reduction peak of the solution containing only

citric acid (Figure 5.8a) is the lowest of all the reduction peaks, even though citric acid is present at the highest concentration. Second, the current of the first reduction peak of the copper citrate solution (Figure 5.8b) and the deposition solution (Figure 5.8d) are similar. This indicates that the largest reduction peak in the deposition solution (Figure 5.8d) is due to a reduction process involving Cu^{2+} in the $(\text{Cu}_2\text{Cit}_2\text{H}_{-1})^{3-}$ species. As discussed in Chapter 3, the reduction of the $(\text{Cu}_2\text{Cit}_2\text{H}_{-2})^{4-}$ is not observed due to the presence of antimony in solution.

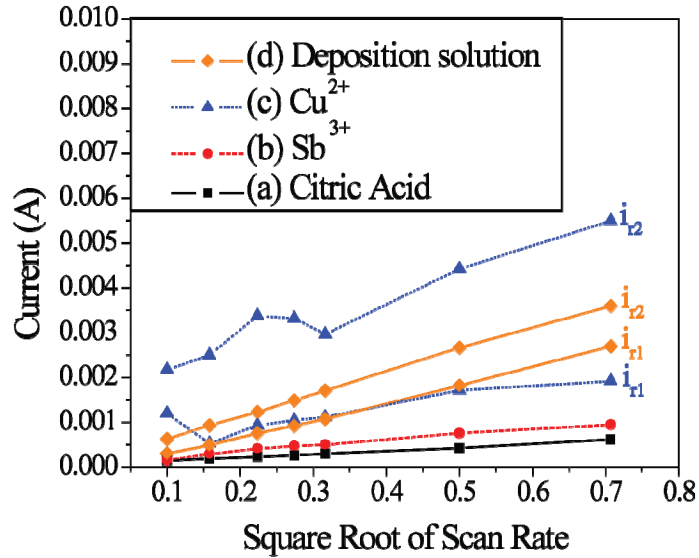
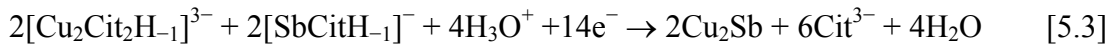


Figure 5.9: Current of the reduction peaks plotted versus square root of scan rate from solutions (a) 0.4 M citric acid, (b) citric acid and 0.025 M Sb_2O_3 , (c) citric acid and 0.1 M $\text{Cu}(\text{NO}_3)_2$ and (d) both metal precursors and citric acid. The i_{r1} & i_{r2} corresponds to the current of the first reduction peak and second reduction peak of the CVs. All solutions were at pH 6. A SSCE reference electrode and a Pt working electrode were used.

Based on the data just described, we propose that Cu_2Sb is deposited at a single potential according to a simple coreduction mechanism.



This reaction accounts for the formation of the final product from slightly acidic solutions, keeping in mind the likely speciation present for the citrate ion. Although there is precedence for a single bimetallic Cu/Sb species in the solid state, the only evidence we have for the presence of such a species in solution under our conditions is from mass spectroscopy experiments.²⁵ Current work is focused on developing the speciation diagram in order to determine the species present under the optimal deposition conditions. Furthermore, deposition from a single bimetallic species would imply that the composition of the films would be constant regardless of potential. It was showed that Cu_2Sb can be deposited at a range of potentials, however the composition of the film changes from Cu-rich to Sb-rich as a function of increasingly negative potentials. This is consistent with the codeposition of two separate species, as noted in reaction described above. The electron imaging studies presented in this chapter also support the reduction of two different species. The activation role that Sb plays before the deposition of copper can occur would require Eq. 3.10 to occur before Eq. 5.3. But with the first two phases of the nucleation sites being copper rich one would suspect that after the activation sites are formed by Eq. 3.10 that copper deposition would occur according to Eq. 3.6. After the first two phase transitions the results from the electron microscopy studies demonstrate that only copper antimonide is deposited which means it is following Eq. 5.3.

5.9 Conclusions

The results from the investigation described here provide evidence that the single-potential deposition of Cu_2Sb can be described by a mix of the ACD and IUPD model. While the times reported in this study are not quantitatively relevant to the depositions on

“normal” substrates, this investigation is unique because TEM grids were used as the working electrode; thereby providing direct compositional, morphological, and crystal structure evidence of the nucleation and growth process. This unique investigation unveiled that the nucleation sites undergo transitions that were not just based on the diffusion of the required elements, but also on the interaction of the elements within the nucleation site. The multiple transitions which occur ultimately leading to the deposition of polycrystalline Cu₂Sb instead of a solid-state alloy of copper and antimony could be a consequence of the high solubility of copper and antimony in each other at moderate temperatures.²⁶ This solubility may be responsible for allowing the solid-state transformations required in order for the direct deposition of Cu₂Sb. The knowledge gained from these experiments will aid in developing a more complete understanding and ultimately better control of the single-potential deposition of crystalline intermetallics from aqueous solutions, and has already been used to aid in developing a procedure to uniformly deposit Cu₂Sb nanowire arrays, as discussed in next chapter.

5.10 References

- (1) Mosby, J. M.; Prieto, A. L. *J Am Chem Soc* **2008**, *130*, 10656.
- (2) Radisic, A.; Vereecken, P. M.; Searson, P. C.; Ross, F. M. *Surf Sci* **2006**, *600*, 1817.
- (3) Budevski, E.; Staikov, G.; Lorenz, W. J. *Electrochim Acta* **2000**, *45*, 2559.
- (4) Vandenbrande, P.; Winand, R. *Journal of Applied Electrochemistry* **1993**, *23*, 1089.
- (5) Brande, P. V.; Winand, R. *Surface and Coatings Technology* **1992**, *52*, 1.
- (6) Winand, R. *Electrochim Acta* **1998**, *43*, 2925.
- (7) Hu, C.-C.; Wu, C.-M. *Surface and Coatings Technology* **2003**, *176*, 75.
- (8) Lin, K. L.; Chen, S. Y.; Mohanty, U. S. *Journal of The Electrochemical Society* **2008**, *155*, D251.
- (9) Aurbach, D.; Zaban, A.; Ein-Eli, Y.; Weissman, I.; Chusid, O.; Markovsky, B.; Levi, M.; Levi, E.; Schechter, A.; Granot, E. *Journal of Power Sources* **1997**, *68*, 91.
- (10) Radisic, A.; Vereecken, P. M.; Hannon, J. B.; Searson, P. C.; Ross, F. M. *Nano Lett.* **2006**, *6*, 238.

- (11) Grujicic, D.; Pesic, B. *Electrochim Acta* **2002**, *47*, 2901.
- (12) Orinakova, R.; Turonova, A.; Kladekova, D.; Galova, M.; Smith, R. M. *Journal of Applied Electrochemistry* **2006**, *36*, 957.
- (13) Podlaha, E. J.; Landolt, D. *Journal of The Electrochemical Society* **1996**, *143*, 893.
- (14) Eliaz, N.; Gileadi, E. *Mod. Aspects Electrochem. FIELD Full Journal Title: Modern Aspects of Electrochemistry* **2008**, *42*, 191.
- (15) Xiao, F.; Yoo, B.; Bozhilov, K. N.; Lee, K. H.; Myung, N. V. *J. Phys. Chem. C* **2007**.
- (16) Han, C.; Liu, Q.; Ivey, D. G. *Electrochim Acta* **2009**, *54*, 3419.
- (17) Sarakonsri, I.; Johnson, C. S.; Hackney, S. A.; Thackeray, M. M. *Journal of Power Sources* **2006**, *153*, 319.
- (18) Fransson, L. M. L.; Vaughey, J. T.; Benedek, R.; Edstrom, K.; Thomas, J. O.; Thackeray, M. M. *Electrochemistry Communications* **2001**, *3*, 317.
- (19) Pearson, W. B. *Z Kristallogr* **1985**, *171*, 23.
- (20) Sharma, S.; Dewhurst, J. K.; Ambrosch-Draxl, C. *Phys Rev B* **2004**, *70*.
- (21) Ren, J. G.; He, X. M.; Pu, W. H.; Jiang, C. Y.; Wan, C. R. *Electrochim Acta* **2006**, *52*, 1538.
- (22) Bryngelsson, H.; Eskhult, J.; Nyholm, L.; Edström, K. *Electrochim Acta* **2008**, *53*, 7226.
- (23) Warren, J. B.; Kundrath, M. R.; (Connecticut Research Institute, Inc., USA). Application: USUS, 1979, p 10 pp.
- (24) Scharifker, B.; Hills, G. *Electrochim Acta* **1983**, *28*, 879.
- (25) Smith, G.; Sagatys, D. S.; Bott, R. C.; Lynch, D. E.; Kennard, C. H. L. *Polyhedron* **1992**, *11*, 631.
- (26) Halimi, R.; Merabet, A. *Surf Sci* **1989**, *223*, 599.

CHAPTER 6

ELECTRODEPOSITION OF Cu_2Sb NANOWIRE ARRAYS

6.1 Introduction

Following the procedure developed in the last three chapters for the single potential deposition of Cu_2Sb films, the electrodeposition of Cu_2Sb nanowire arrays will be discussed in this chapter. The motivation for depositing nanowire arrays of Cu_2Sb is the battery performance of these arrays should outperform that of the bulk material. The improvements expected by using nanoscale morphology were discussed in detail in Chapter 2. As discussed in the preceding sections using the procedure developed for the deposition of Cu_2Sb films produced wires without modification, but to obtain uniform crystalline nanowire arrays the procedure had to be optimized for depositing Cu_2Sb into anodic alumina (AAO) templates.

6.2 Experimental procedures

Cu_2Sb films were electrodeposited from aqueous 0.4 M citric acid (99.5+% Aldrich) solutions containing 0.025 M antimony (III) oxide (nanopowder, 99.9+% Aldrich), and 0.08 M copper nitrate hemipentahydrate (99.9+% Aldrich). The solutions were prepared by adding the citric acid to Millipore water (18 Ω) followed by the addition of antimony oxide. The dissolution of the antimony oxide was aided by mechanical stirring. The copper nitrate was subsequently added to the solution which then turned deep blue. The solution was ready for deposition after adjusting the pH to a value of 6 using 5 M potassium hydroxide (ACS certified, Fisher). Details on the solution preparation can be found in Chapter 3.

All cyclic voltammograms (CVs) and depositions were conducted in a three-electrode cell, using a BAS 100B potentiostat, CHI 660workstation, and a Gamry Ref3000. In all cases platinum gauze was used as the counter electrode, and a saturated

sodium calomel electrode (SSCE), 243 mV versus the standard hydrogen electrode, was used as the reference electrode. For nanowire depositions, the substrates were prepared by evaporating copper and gold onto the back of the AAO templates using a Denton Vacuum evaporator with a Maxtek MDC-260 deposition controller. The alumina templates used are Anopore[®] membranes developed by Whatman[®]. The diameter of the alumina membranes are 13 mm with a nominal pore size of 200 nm and a thickness of 60 μm . A copper wire is attached to the corresponding substrate using graphite paste to make electrical contact. In order to deposit on a flat surface, clear nail polish was used to insulate the edges of the substrates, the back of the templates, and the copper wire. For the preliminary work the wires were deposited for 2 h in a stirred solution after the template was fully wetted (constant open circuit potential (OCP)). As discussed in detail later, different potential pulse procedures were investigated to improve the uniformity of the pore filling and wire growth.

The powder X-ray diffraction (XRD) patterns were obtained with a Scintag X-2 advanced diffraction X-ray cabinet system using Cu $K\alpha$ that is equipped with a stationary stage and a Peltier Detector. The Optical microscope images were taken on an Olympus BX52 equipped with a polarizer (model # U-AN360-3) using an Olympus UMPlanF1 lens with a magnification of 10x. A QColor5 Olympus camera was used to obtain digital images using the software QCapture Pro. version 5.1.1.14. Scanning electron microscopy (SEM) images, and energy dispersive spectroscopy (EDS) spectra analyses were performed using a JEOL JSM-6500F equipped with a Thermo Electron energy-dispersive spectroscopy detector with an applied voltage of 10 kV. Mechanical polishing with diamond paste was used to remove the back contact on the template after wire growth.

Removal of the back contact was required in order to perform SEM and EDS of the bottom of the template. To collect cross-sectional SEM images of the wires growing in the template, a piece of the template was removed and held at 90° angle with respect to the sample holder using carbon paste. The template was then dissolved away in a solution composed of 3.5% by volume H₃PO₄, and 45 g l⁻¹ CrO₃, allowing images of the wires without the template to be obtained.

6.3 Cu₂Sb nanowire arrays obtained using procedure for Cu₂Sb films

After the procedure for the electrodeposition of copper antimonide films was perfected, nanowires arrays were electrodeposited in alumina templates using the same conditions and parameters. The only differences in the deposition procedure used to deposit wires were: the templates were wetted with the deposition solution until a constant OCP is reached, and the solution is mechanically stirred during the deposition. Figure 6.1 is a powder XRD pattern of wires deposited at -1050 mV vs. SSCE for 2 h. The labeled diffraction peaks are indexed to Cu₂Sb (PDF no. 01-0850492). Based on the relative intensities of the diffraction peaks the same preferred orientation (001) is observed as was found for deposited films of Cu₂Sb (Figure 4.5), except there is no sign of the diffraction peak corresponding to the (001). The broad diffraction peak from 20 to 28° two theta is the diffraction peak of the amorphous AAO template.

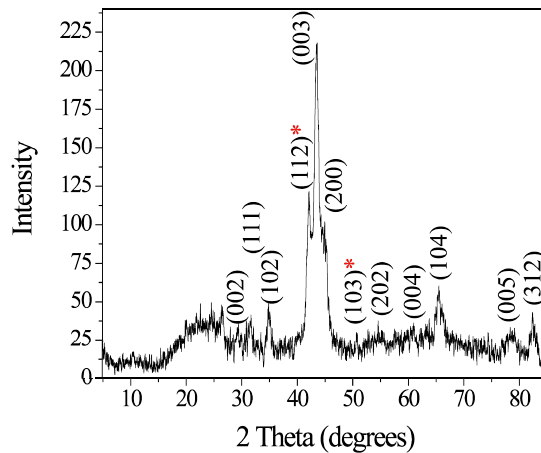


Figure 6.1: Powder XRD pattern of Cu_2Sb nanowires deposited in alumina template using optimized deposition solution and conditions. The red stars indicate the diffraction peaks of the copper substrate (PDF no. 01-071-4608), and the indexed peaks match Cu_2Sb (PDF no.01-085-0492).

A collection of SEM images of the Cu_2Sb nanowires deposited with this constant potential deposition can be seen in Figure 6. Figure 6.2a & b are SEM images of the bottom of the template after the substrate was mechanically polished off. These images show that the wires fill the entire diameter of the pore, which demonstrate that there are no wetting complications between the deposited Cu_2Sb nanowires and the template. While most of the pores shown in Figure 6.2a are filled this was an isolated growth, most of the template was empty. Figure 6.2c, d & e are SEM images of the cross section of the template which show the Cu_2Sb nanowires have no discontinuities throughout the wire length. It is also apparent from the cross-sectional SEM images that the wire length is not uniform and the wires do not fill the entire length ($60\ \mu\text{m}$) of the template. Figure 6.2e & f is an SEM image of a group of wires after a majority of the template was dissolved away. The longer unbroken wires seen are about $9\ \mu\text{m}$ long, and the average diameter of the wires is $200\ \text{nm}$ which correlates to the diameter of the AAO pores. Unfortunately the results shown in Figure 6.2 are the best out of multiple trials. Cu_2Sb

nanowire arrays deposited using the procedure developed for depositing Cu_2Sb films, lead to non-reproducible composition, and crystallinity. Also, the pore filling and wire length obtained using this procedure were not uniform.

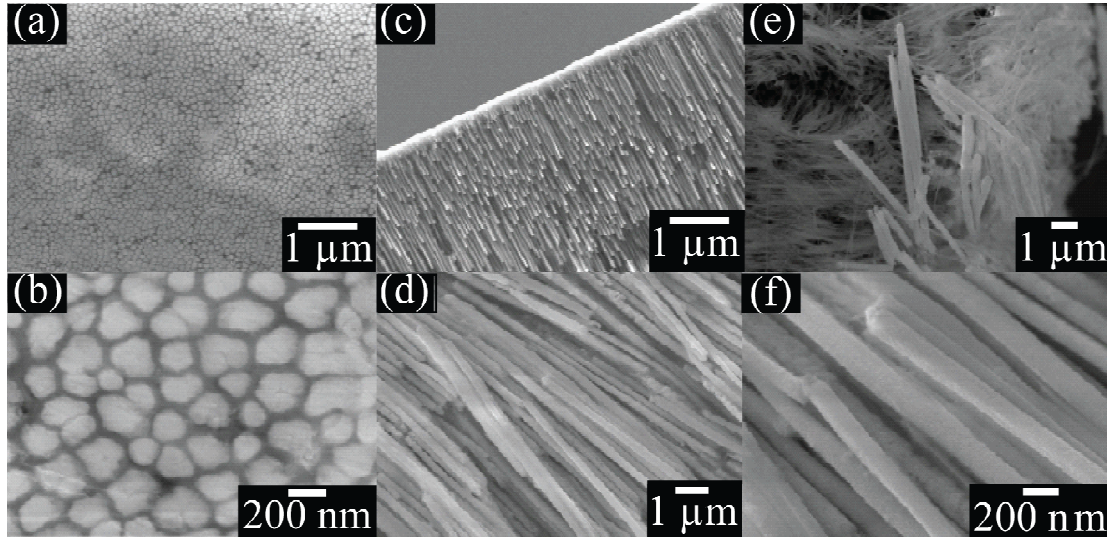


Figure 6.2: SEM images of the Cu_2Sb wires deposited at different temperatures. (a) back of template 3,000X, (b) back of template 70,000X, (c) cross section 3,000X, (d) cross section 9,500X, (e) wires 8,000X, and (f) cross section 30,000X.

6.4 Introduction to pulse potential electrodeposition of Cu_2Sb nanowire arrays

To overcome these problems found from depositing Cu_2Sb nanowire arrays at a single potential, potentiostatic pulse deposition was employed. Galvanostatic pulse deposition is known to increase the uniformity of the deposit by eliminating the diffusion profile that is established during the deposition.¹⁻⁴ The poor reproducibility and non-uniform Cu_2Sb nanowire arrays deposited at a single potential is from non-uniform diffusion profiles that are established in the individual pores of the AAO template during the deposition. In pulse deposition (pulse plating), there are two time parameters which can be controlled: the on time (T_{on}) and the off /reverse time (T_{off}). The motivation for using this technique to deposit nanowire arrays in templates is that the concentration gradient established during T_{on} dissipates during T_{off} . This should allow for more

uniform wire growth, pore filling, and limit composition affects that are created by local concentration gradients established in the pores. There are examples of improved wire growth in templates using pulse deposition, yet no systematic investigation was found in the literature describing how the different parameters affected the wires deposited.⁵ This section of the chapter will cover the experimental results of the pulse potential deposition of Cu₂Sb nanowire arrays, and provide insight to how the different parameters affected the deposited nanowires.

In potentiostatic pulse deposition there are four parameters that can be adjusted that affect the quality and properties to the resulting material. These four parameters are labeled in a schematic of a square wave potential input signal shown in Figure 6.3. Besides the two time parameters (T_{on} and T_{off}) the other two parameters shown in Figure 6.3 are the deposition potential (E_f) and the “quiet” potential (E_r). For the preliminary pulse deposition experiments, the E_f was the same potential used in the single potential deposition of Cu₂Sb (-1050 mV vs. SSCE). The preliminary experiments were performed using the CHI potentiostat which does not permit OCP conditions during the T_{off} . Thus, the potential used for the E_r was varied in attempt to pass as close to zero current as possible. This was in order to stop the deposition long enough for the concentration gradient to dissipate without depositing at a different potential or oxidizing the material deposited during the T_{on} .

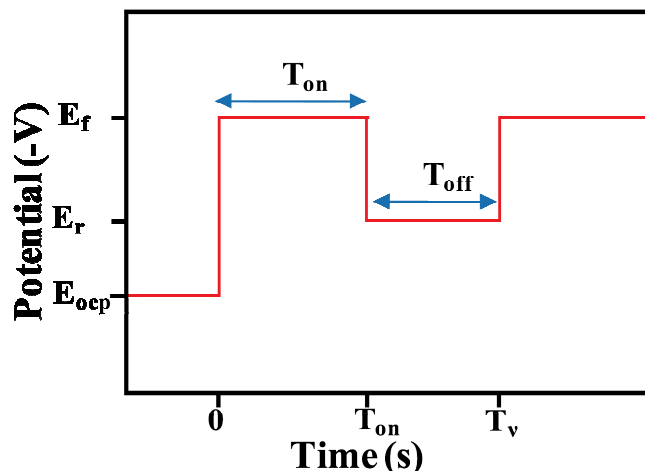


Figure 6.3: Example of input signal for the pulse deposition technique. The T_{on} is the time of the deposition pulse, T_{off} is the time of the zero current pulse, E_{ocp} is the open circuit potential, E_f is the deposition potential, and E_r is the potential that is applied during T_{off} .

6.5 Optimizing the pulse potential deposition of Cu_2Sb films

Before adding the complexity of depositing into AAO templates, films were deposited using pulse deposition to determine the effect that the different parameters had on the resulting films. Table 6.1 shows the variety of different parameters examined. The first parameter to be investigated was the potential (E_r) applied during T_{off} . Looking at the values for the E_r in Table 6.1 it can be seen that the potential found to give a current closest to zero was -525 mV vs. SSCE. Looking at a CV of the deposition solution (Figure 3.2) this potential corresponds to a potential where the current is zero between potentials that cause either cathode or anodic currents to pass. When the E_r was more negative of this potential the XRD diffraction of the films deposited had diffraction peaks that match $Cu_{3.3}Sb$. Potentials more positive than -450 mV vs. SSCE were not tested because these potentials would strip any material deposited.

The next two parameters investigated (Table 6.1) were the time constants T_{on} and T_{off} . For all of the pulse depositions discussed in this chapter the times used for the T_{on} and T_{off} are considerably longer than the time needed to charge the double layer (discussed in more detail in Chapter 7). This means any differences in the deposits obtained using different T_{on} and T_{off} are due to changes in the diffusion profile caused by Faradaic processes, not non-Faradaic processes. While keeping T_{off} constant at 1.5 s, it was found that films deposited with shorter T_{on} times had diffraction peaks matching $Cu_{3.3}Sb$, while films deposited with longer T_{on} times had diffraction peaks matching Cu_2Sb . Varying T_{off} while keeping the T_{on} constant at 1.5 s, it was found that the crystallinity of the Cu_2Sb peaks increased with shorter T_{off} times.

Table 6.1- Summary of parameters examined for the pulse potential deposition of Cu_2Sb films onto copper substrates. Each range “-” corresponds to five different values tested between the limits shown.

T_{on} ms	T_{off} Ms	E_r -mV	E_f -mV	Examined Parameter
5-50	15-15000	-600	1050	Pulse period
5- 50000	15-150000	180	1050	Pulse period
150	1500	450-525	1050	Dead potential
300- 3000	1500	525	1050	T_{on}
1500	150-7500	525	1050	T_{off}
150- 7500	75- 3750	525	1050	Pulse period

An interesting observation can be made from the results discussed above. The best results were obtained when the time parameters were the closest to a single potential step deposition, because longer T_{on} times and shorter T_{off} times produce the most crystalline films. The powder XRD pattern with the most crystalline Cu_2Sb peaks from this series of experiments is shown in Figure 6.4. This film was deposited using a T_{on} of 1.5 s, T_{off} of 0.15 s, E_f of -1050 mV vs. SSCE, and an E_r of -525 mV vs. SSCE. Although this film was the most crystalline out of the films deposited using pulse

deposition, the crystallinity is much lower than the films previously deposited using a single potential step (determine by peak width at half height).

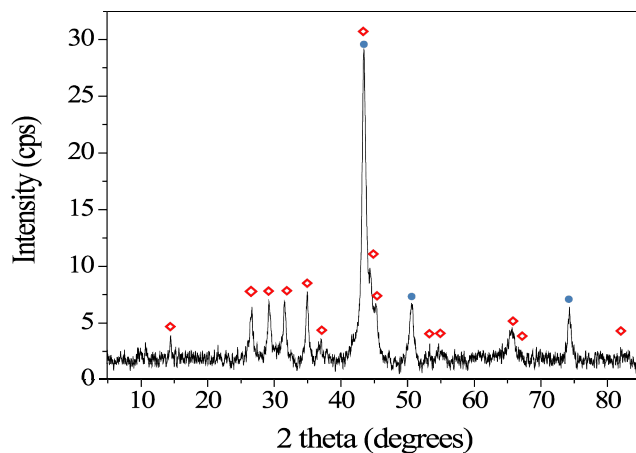


Figure 6.4: Powder XRD pattern of Cu_2Sb film deposited using pulse deposition technique onto copper substrates. T_{on} was 1.5 s, T_{off} was 0.15 s, E_f was -1050 mV vs. SSCE, and E_r was -525 mV. The red diamonds are diffraction peaks that match Cu_2Sb (PDF no. 01-085-0492), and the Blue circles are diffraction peaks that match copper (PDF no. 01-071-4608).

6.6 Optimizing the pulse potential deposition of Cu_2Sb nanowire arrays

After the optimal parameter for the pulse potential deposition of Cu_2Sb films was determined, pulse potential deposition of Cu_2Sb nanowire arrays was attempted using templates with copper current collectors. A summary of the different parameters used to deposit nanowires are shown in Table 6.2. The XRD patterns of all the nanowires grown during these experiments consist of a few broad peaks making the exact characterization of the wires difficult. The broadness of the peaks also meant that the wires grown using this technique were not very crystalline, which is problematic for characterization during the battery testing. Starting with the same parameters that produce the best Cu_2Sb film it was found that only four broad diffraction peaks could be indexed to Cu_2Sb (Figure 6.5).

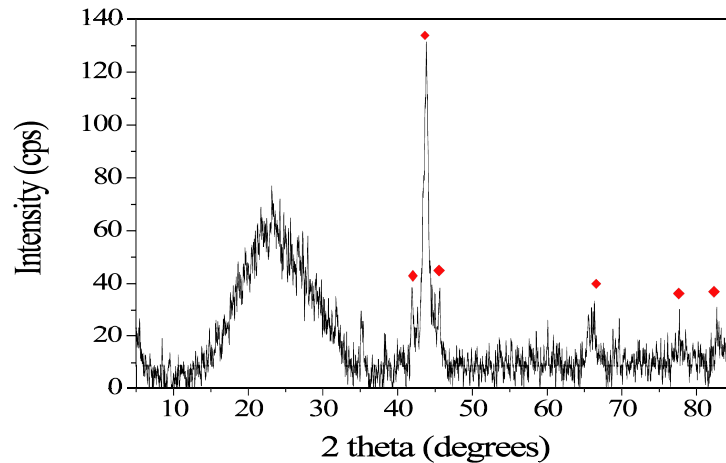


Figure 6.5: Powder XRD pattern of Cu_2Sb nanowires deposited using pulse deposition onto a copper substrate. T_{on} was 1.5 s, T_{off} was 0.15 s, E_f was -1050 mV, and E_r was -525 mV. The red diamonds are diffraction peaks that match Cu_2Sb (PDF 01-085-0492).

Decreasing both the T_{on} and T_{off} and trying different potentials for E_f only ended up decreasing the number of diffraction peaks obtained. SEM images of the nanowire arrays that were grown using the pulse deposition under all conditions examined did have uniform pore filling within the entire template and uniform wire length. In attempt to get both uniform pore filling and crystalline nanowires, depositions were carried out by using the pulse deposition procedure for one to five minutes, followed by bulk deposition. All wires deposited with this procedure had one broad diffraction peak in the powder XRD which made it difficult to characterize the nanowire array as Cu_2Sb .

Table 6.2- A summary of parameters examined for the pulse potential deposition of Cu_2Sb nanowires onto copper substrates. Each range (-) corresponds to five different values tested. Bulk electrolysis was performed at: -800 , -900 , -1000 , -1100 , -1200 mV vs. SSCE.

T_{on} ms	T_{off} ms	E_r -mV	E_f -mV
1500	150	525	1050
150	15	525	1050
1500	150	525	900 - 1300
1500	150	525	1050

Although the crystallinity of the nanowire arrays grown with the pulse potential deposition is poor, it did lead to uniform pore filling and wire length. A comparison of the pore filling and wire length of arrays deposited with pulse potential and single potential depositions is shown in Figure 6.6. Comparing the SEM images (Figure 6.6e & f) of the back of the template after the back contact has been removed, shows that almost every pore is filled in the pulse potential case (Figure 6.6e). Unlike the arrays grown with a single potential step, the pores of the entire template were filled when pulse potential deposition was used. Comparing the SEM images of the pulse potential deposited nanowires (Figure 6.6a & c) to single potential deposited wires (Figure 6.6b & e), it is clear that the wires grown with the pulse procedure have a uniform length. Uniform wire length will be an important property for device fabrication later on.

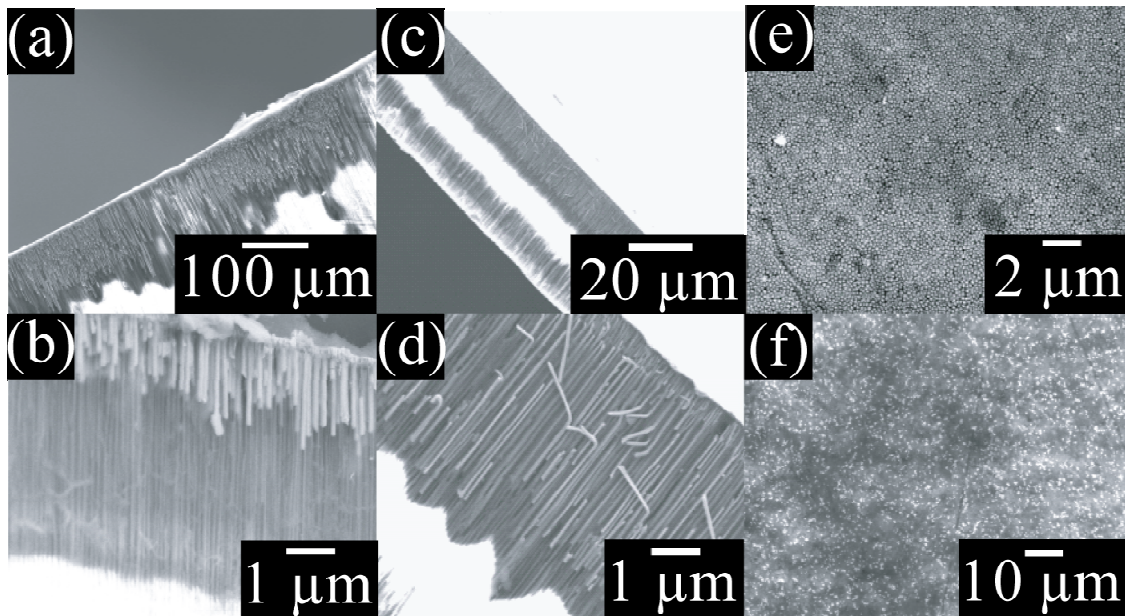


Figure 6.6: SEM images of Cu_2Sb nanowires deposited into alumina templates with copper substrates. The wires were deposited using bulk electrolysis at -1050 mV vs. SSCE for (a, b, f); and pulse deposition (c, d, e) with T_{on} of 1.5 s, T_{off} of 0.15 s, E_f of -1050 mV vs. SSCE, and E_r of -525 mV vs. SSCE.

During the pulse potential deposition experiments, a template was left soaking in the deposition solution for five hours (usually only an hour is needed) to wet the pores before the deposition was carried out. The copper substrate was completely dissolved after the five hours leaving only the template and the nail polish remaining. To determine if this was a random event or a consistent process, a glass slide with an evaporated copper film was set in the deposition solution and allowed to soak. After three hours the evaporated copper film had been completely removed from the glass slide. This effect had not been noticed before because during the single potential step depositions a cathodic potential is applied as soon as the substrate is placed into solution. Examining the OCP (-200 mV vs. SSCE) of the deposition solutions and the CVs of copper solutions (Figure 3.5) it became obvious that the OCP was negative enough to cause the oxidation of the evaporated copper following Eq 3.4. This means that there is a high possibility that unwanted stripping of the copper substrate is occurring during the wetting of the pores. Thus, it was decided to use evaporated gold contacts on the AAO templates for the remaining pulse potential deposition experiments.

6.7 Pulse potential deposition of Cu_2Sb onto gold substrates

The pulse procedure was first examined on gold substrates evaporated onto glass slides. During the initial experiments a procedural complication arose. The gold did not wet well to the glass slide, even though a Cr layer was used to improve the cohesion. Different techniques were used in order to improve the wetting of the gold onto the glass slides. The two most successful were annealing under argon in a tube furnace and flame annealing using a H_2 flame. It was later determined that the evaporator was not calibrated correctly, leading to thick films being evaporated at fast rates. The extra thick

films evaporated at fast rates was soon determined to be the source of the wetting issue, which was fixed after proper calibration.

A benefit of using the gold substrates compared to the copper substrate is that it allowed the examination of the current profiles using different pulse parameters before carrying out the depositions. This came from the ability to apply E_f for T_{on} , E_r for T_{off} , and then anodic potential that stripped off any material deposited leaving a clean gold substrate. This was not possible with copper because the anodic potential would also strip the copper substrate. This allows multiple experiments with different parameters to be examined using the same substrate and solution, which is much simpler than have to deposit a film every time a parameter is changed. An example of the current time behavior on a gold substrate can be seen in Figure 6.7. In Figure 6.7, during the T_{on} , there is a peak in the current response corresponding to the nucleation and growth of the material on the substrate. During T_{off} the current response levels out at different currents depending on the E_r applied. From current plots like the one shown in Figure 6.7, it is possible to adjust the E_r until a potential is found which passes the smallest amount of cathodic current. Examining current time plots like that in Figure 6.7 also allowed the T_{on} and T_{off} to be chosen relative to the different current behavior seen at different times.

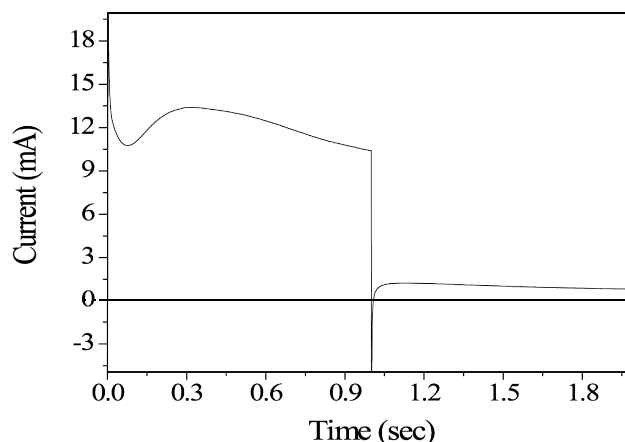


Figure 6.7: Current behavior during one full cycle of a pulse experiment conducted using a gold electrode. With a T_{on} and T_{off} of 1 s, and E_f of -1050 mV, and a E_r of -525 mV vs. SSCE.

To examine the effect the T_{on} on the deposition of Cu_2Sb relative to the peak in Figure 6.7, two times were chosen before the peak in Figure 6.7 and three times were chosen after the peak. The T_{off} for these experiments was 1 s, chosen by examining the time required for the current due to E_r to be constant. The E_f and E_r used for the experiments are listed in Table 6.3. The E_r was found by examining plots like Figure 6.7, as described earlier. It was found during these experiments that the XRD patterns of films deposited with short T_{on} times had diffraction peaks corresponding to $\text{Cu}_{3,3}\text{Sb}$. As T_{on} got longer more Cu_2Sb peaks were observed in the XRD patterns. The best film deposited onto gold substrates following these experiments used the parameters listed in the last row of Table 6.3.

Figure 6.3- A summary of parameters used for pulse deposition of Cu₂Sb films onto gold substrates. The E_f and E_r are in respect to a SSCE reference electrode.

T_{on} ms	T_{off} ms	E_r -mV	E_f -mV
500	1000	400	1050
100	1000	400	1050
250	1000	400	1050
750	1000	400	1050
1000	1000	400	1050

The powder XRD pattern of the most crystalline Cu₂Sb film using the parameters listed in the last row of Table 6.3 is shown in Figure 6.8. This pattern is similar to the diffraction pattern seen in Figure 6.5, except based on the peak to noise ratio it would seem that the film in Figure 6.5 is less crystalline (there are other factors that could cause this difference. e.g. different substrate size). In both experiments the E_f was -1050 mV vs. SSCE and the E_r only differed by 125 mV (this does not cause a large change in the current response), but the time parameters were completely the opposite. In one case long T_{on} and short T_{off} gave the best results, while in the other case short T_{on} and long T_{off} gave the best results. This inconsistency could be based on the stripping of copper in the first set of experiments, which didn't occur in the second set of experiments.

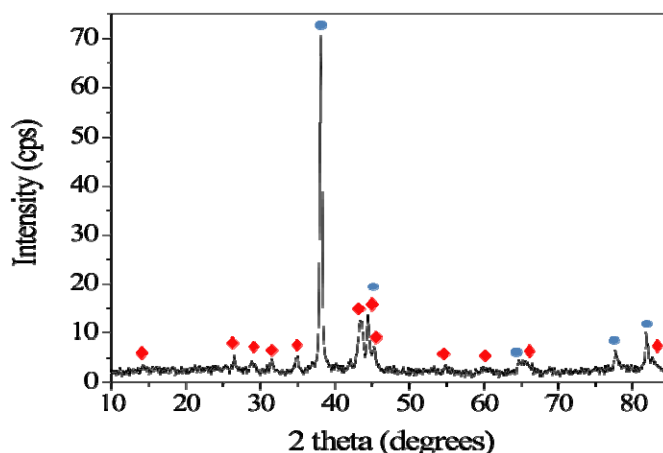


Figure 6.8: Powder XRD pattern of film deposited using pulse potential deposition. T_{on} was 1 s, T_{off} was 1 s, E_f was -1050 mV, and E_r was -400 mV vs. SSCE. The red diamonds are diffraction peaks that match Cu_2Sb (PDF no. 01-085-0492), and the blue circles are indexed to gold (PDF no. 01-071-4614).

6.8 Modified pulse potential deposition based on theory and TEM investigation

To eliminate the complications from using a E_r that is not “zero”, the Gamry potentiostat was used, which allows a sequence of different procedures to be implemented in one experiment. This allows the E_f of -1050 mV vs. SSCE to be applied for the T_{on} and then an OCP experiment can be ran for T_{off} . For these experiments the same time parameters summarized in Table 6.3 were used. Before these experiments were performed the mathematics of a pulse potential deposition was investigated to help determine the best parameters to use for the experiments. This mathematical treatment can be found in Chapter 7. During the qualitative mathematical treatment discussed in Chapter 7 it was determined that the T_{off} needs to be longer than 1.3 s to mitigate the diffusion profile that is established during the T_{on} . Also, the TEM investigations discussed in Chapter 5 demonstrated that a T_{on} of over 1 s was needed to permit the transformations that occur during the nucleation and growth of the electrodeposited Cu_2Sb . Based on the results from both of these investigations a T_{on} and T_{off} of 2 s was

used with the resulting current and potential profile are shown in Figure 6.9. From these profiles it can be seen that the current stabilized within the first ten seconds (Figure 6.9b), but the OCP potential during the T_{off} did not stabilize until after ninety seconds (Figure 6.9a). The current profile stabilizing by ten seconds is representative of the nucleation of the pores, so by ten seconds the Cu_2Sb nucleation has occurred in all the pores that are going to grow wires. The OCP profile on the other hand is based on the material that is deposited during the T_{on} . This means that up to ninety seconds the material being deposited into the pores is changing, but after ninety seconds when the OCP is stabilized the material deposited is no longer changing. This time frame is much longer than what was determined to be needed in Chapter 5 during the TEM investigations.

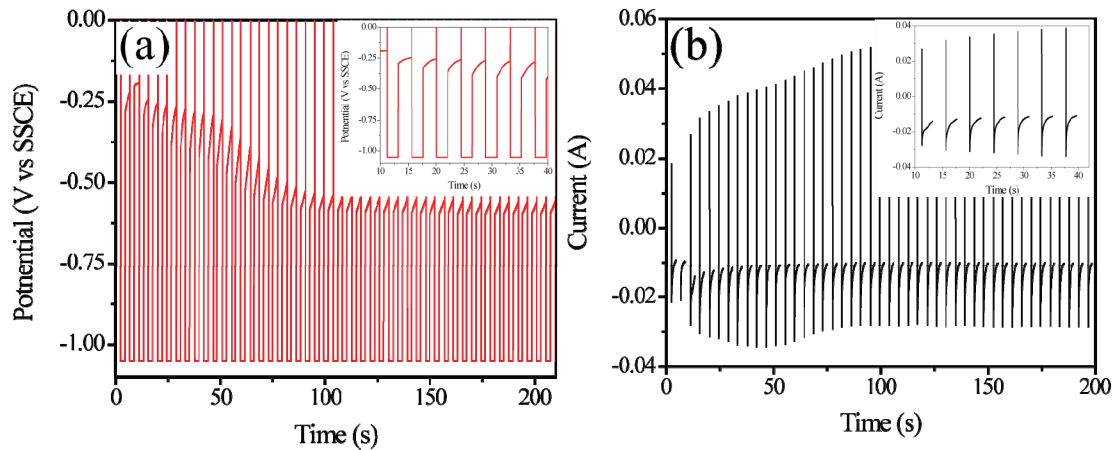


Figure 6.9: (a) The potential profile of the OCP measured during the T_{off} and the (b) current profile of the deposition for a pulse potential deposition of Cu_2Sb . The insets show the details from 10 to 40 s. The T_{on} was 2s, the T_{off} was 2 s, and E_f was -1050 mV.

Using the procedure discussed above for which the potential and current profiles are given in Figure 6.9, uniform Cu_2Sb nanowire arrays with good crystallinity were deposited. The powder XRD pattern of a nanowire array deposited with this procedure is shown in Figure 6.10. By comparing peak width at half height of the diffraction pattern

in Figure 6.10, the nanowire array is more crystalline than the arrays deposited using a single potential step deposition (Figure 6.1). Also, based on relative peak height the same preferred orientation is found in the nanowires deposited using this procedure as was found in the single potential step deposition of Cu_2Sb films (Figure 4.7). The broad diffraction that is observed in the diffraction pattern from 15° to 40° two theta is from the AAO template which is still present.

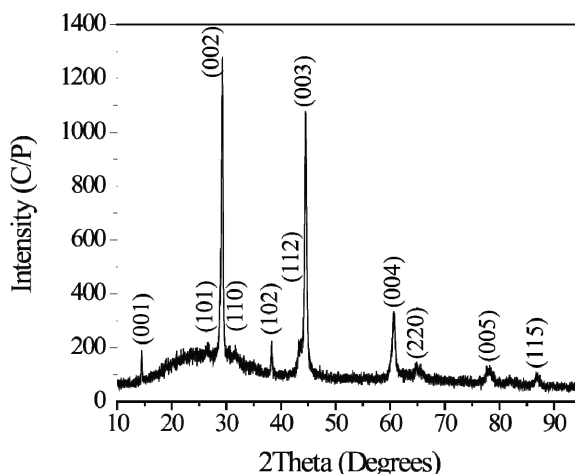


Figure 6.10: XRD pattern of Cu_2Sb nanowire array deposited using the pulse potential deposition procedure and Gamry instrument. The T_{on} was 2s, the T_{off} was 2 s, and E_f was -1050 mV. The diffraction peaks are indexed to Cu_2Sb (PDF no. 01-085-0492).

The uniformity of the Cu_2Sb nanowires deposited with this procedure is evidenced from the SEM images shown in Figure 6.11. The SEM images in Figure 6.11a shows Cu_2Sb nanowires filled the entire template. Certain parts of the template were not completely removed after soaking in the dissolution solution for twenty four hours as evidenced by the center of the SEM image in Figure 6.11b. This has undesirable consequences for battery testing, as will be discussed in Chapter 9. Looking at higher magnification image of the wires where most of the template has been removed (Figure 6.11c) it can be seen that the wires have collapsed onto each other, which creates the

texture observed in Figure 6.11a. The wires shown in Figure 6.11 are between 4-5 μm (4000-5000 nm) in length and only 200 nm in diameter. It is not uncommon that nanowires with this aspect ratio do not stand straight up off the current collector. Examining the SEM image of the cross section of the Cu_2Sb nanowire array (Figure 6.11d) it is clear that the wires are congruent for the entire length with no sign of compositional changes via EDS (not shown).

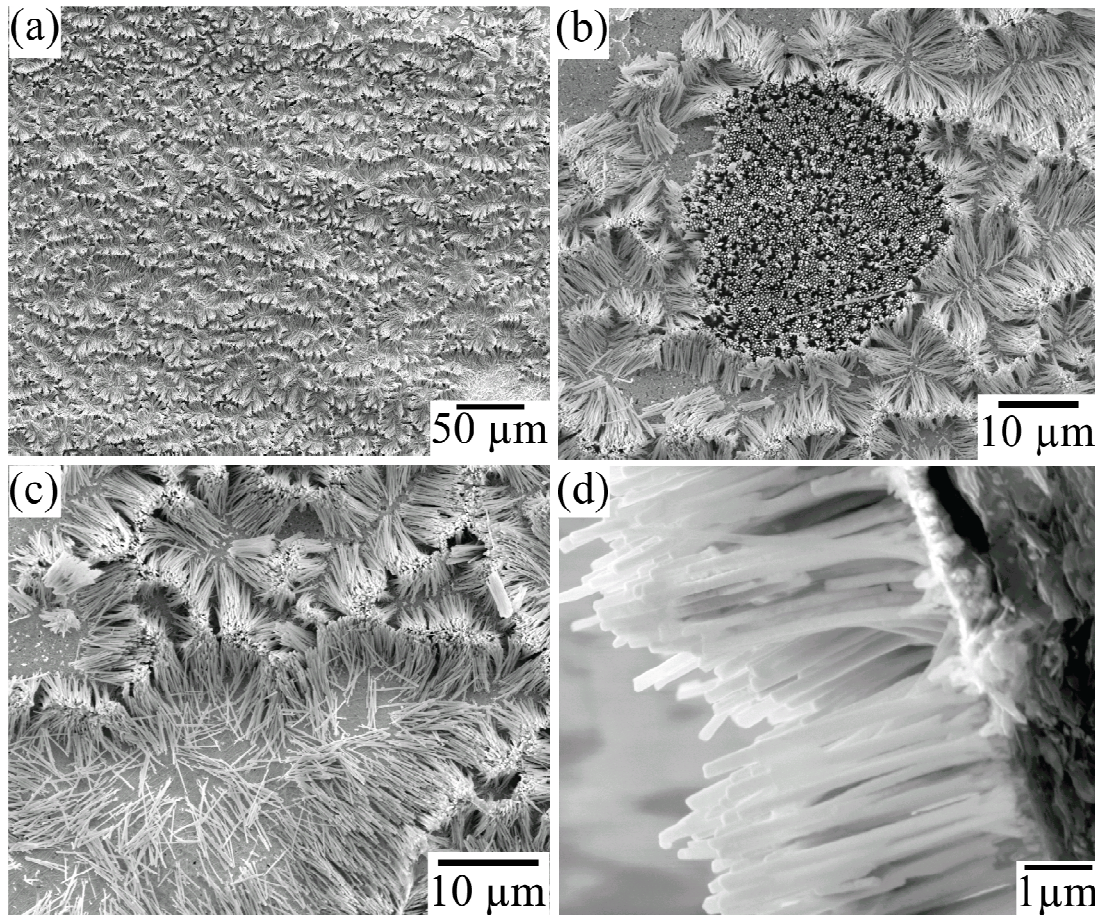


Figure 6.11: SEM images of Cu_2Sb nanowire array deposited using the pulse potential pulse potential deposition procedure and Gamry instrument. **(a)** SEM image from the top of Cu_2Sb nanowire array at 300X, **(b)** SEM image from top of array at 1500X, **(c)** SEM image from top of array at 2000X, and **(d)** cross sectional SEM image of array at 20000X. The T_{on} was 2s, the T_{off} was 2 s, and E_f was $-1050\ \text{mV}$.

6.9 Conclusions

In this chapter, the single potential deposition procedure for depositing Cu_2Sb films developed in Chapter 4 was modified to deposit nanowire arrays of Cu_2Sb . It was determined that a single potential step deposition lead to poor reproducibility and non-uniform pore filling, thus a procedure for pulse potential deposition was developed. As there is not much in the literature on pulse potential deposition, experiments were performed in order to determine the effect that the different deposition parameters had on the deposited material. In doing this a few procedural complications arose that delayed successful results, but after performing a qualitative mathematical treatment of the pulse potential deposition (Chapter 7) and performing TEM studies of the nucleation and growth of Cu_2Sb (Chapter 5) a procedure was developed that deposits crystalline, uniform Cu_2Sb nanowires from aqueous solutions at room temperature.

6.10 References

- (1) Ibl, N.; Puipe, J. C.; Angerer, H. *Surface Technology* **1978**, *6*, 287.
- (2) Ibl, N. *Surface Technology* **1980**, *10*, 81.
- (3) Podlaha, E. J.; Landolt, D. *Journal of The Electrochemical Society* **1996**, *143*, 893.
- (4) Mishra, R.; Podlaha, E. J. *Journal of the Electrochemical Society* **2006**, *153*, C422.
- (5) Trahey, L.; Becker, C. R.; Stacy, A. M. *Nano Lett.* **2007**.

CHAPTER 7

MATHEMATICS OF PULSE POTENTIAL DEPOSITION

7.1 Introduction to math of pulse deposition

The potentiostatic pulse technique used to deposit uniform Cu₂Sb nanowire arrays discussed in the last chapter is not a common electrodeposition procedure. This is the reason that experiments were performed testing how the different parameters affected the nanowires that were deposited. The parameters that control the deposition are: (1) the time that the deposition potential is applied (T_{on}), (2) the time that no charge is being passed (T_{off}), (3) the deposition potential (E_f), and (4) the potential applied during the “quiet” time (E_r). On the other hand, the mathematics for galvanostatic (current controlled) pulse plating have been worked out and it has been used thoroughly in the literature.¹⁻⁵ Since this has not been done specifically for the potentiostatic (potential controlled) case, the concepts for the galvanostatic pulse plating and chronoamperometric reversal techniques are used to develop a qualitative mathematical treatment for the potentiostatic case in this chapter. The results from this qualitative treatment were used to help focus the experiments performed in the last chapter that finally lead to an optimized procedure for depositing uniform nanowire arrays of Cu₂Sb. First, an overview of the theory behind galvanostatic pulse deposition found in the literature will be presented, starting with a book edited by Puipe, and Leaman.⁶

Whenever a potential is applied between two electrodes in solution the total current density (j_t) that is measured is made up of two components: a faradaic (j_f) and non-faradaic (j_c) component as seen in Eq 7.1.

$$j_t = j_c + j_f \quad [7.1]$$

The simple circuit diagram in Figure 7.1 can be used to model this situation, and to derive the current density from the two components.

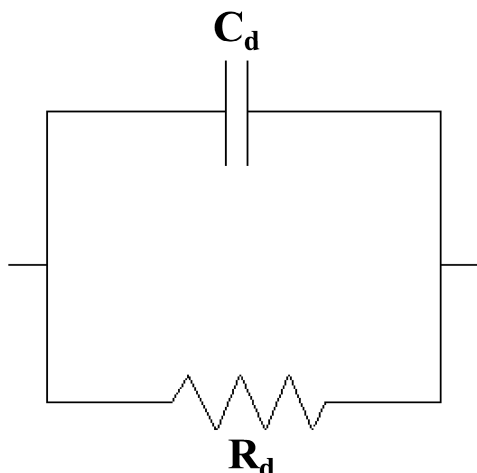


Figure 7.1: Circuit corresponding to an electrode in solution. C_d is the double layer capacitance, R_s is the faradaic resistance.

The faradaic component is shown in Eq 7.2 and the non-faradaic component is shown in Eq 7.3.

$$j_F = j_0 \left[\exp\left(\frac{\alpha z F \eta}{RT}\right) - \exp\left(-\frac{(1-\alpha) z F \eta}{RT}\right) \right] \quad [7.2]$$

$$j_c = \frac{dQ}{dt} = C \frac{d\eta}{dt} \quad [7.3]$$

Where η is the over potential, z is the number of electrons, R is the gas constant, j_0 is the value of the current density (parameter controlled by potentiostat), T is the temperature and F is Faradays constant ($96485.34 \text{ C mol}^{-1}$). For Eq 7.3, Q is the amount of charge and C is the capacitance. Both Eq 7.2 and 7.3 depend on the overpotential, which changes in time to maintain the desired current density in galvanostatic experiments. In most electrochemical techniques the input signal, whether it be potential or current, is applied on time frames where the double layer (modeled by the capacitor in Figure 7.1) is charged so quickly, the non-faradaic current can be neglected. Then the current passing

is made up of only the faradaic component (modeled by the resistor in Figure 7.1). Thus, one limit for T_{on} and T_{off} is at long pulse times the current is the same as it would be for a bulk deposition. At this limit all the current density is faradaic and can be related to the over-potential using Eq 7.2.² To determine when this limit applies, the time needed to charge the double layer must be calculated. Rearranging Eq 7.3 to get Eq 7.4, it can be seen that the charging time is dependent on the area of the electrode A , the thickness of the double layer d , and the ratio of over-potential to current density.

$$t_c^* = \frac{C\eta}{j} = \frac{\varepsilon A \eta}{dj} \quad [7.4]$$

Using values that would emulate the deposition of Cu_2Sb it is found that the double layer is charged after 2 ms, after which the current density is made up of only the faradaic component. This is a short period of time, and therefore the effect of charging the double layer should not affect the properties of the material deposited using the bulk deposition or pulse deposition procedures.

So far, we have found that unless the pulse time is shorter than 2 ms the current density can be represented using Eq 7.2 and therefore, differences in the material deposited using pulse deposition and bulk deposition should not be due to the charging of the double layer. It was mentioned in Chapter 6 that pulse deposition is used to change the concentration profile that is created during the deposition. This change in concentration profile is where the differences in the bulk and pulse deposition techniques stem from. In pulse deposition, two diffusion layers get established: the first is called the pulse diffusion layer (δ_p), and the second is the stationary diffusion layer (δ_s).² This is schematically shown in Figure 7.2.

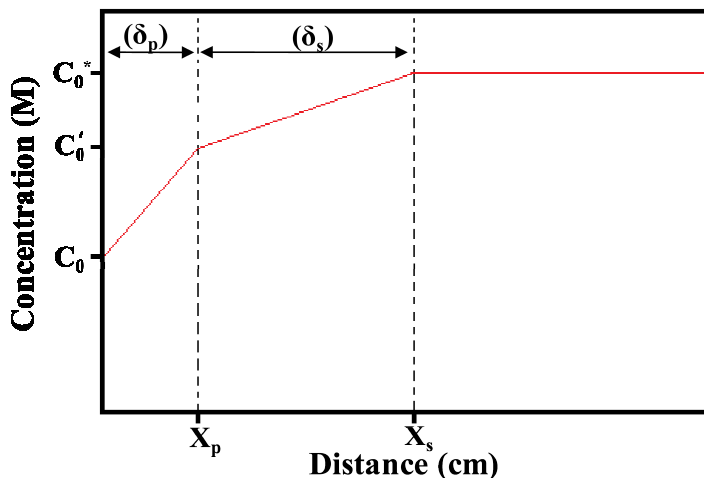


Figure 7.2: Concentration profile established during a pulse deposition. δ_p is the pulse diffusion layer and δ_s is the stationary diffusion layer.

The thickness the two diffusion layers can be calculated using Eq 7.5, where D is the diffusion coefficient of the electro-active species, the time corresponding to δ_p is the pulse length (T_{on}), and time corresponding to δ_s is calculated using Eq 7.5 which is known as the duty cycle (T_θ). One thing pointed out by the authors is the value of δ_p is not dependent on the over-potential or current density, just the diffusion coefficient and T_{on} according to Eq 7.6.²

$$T_\theta = \frac{T_{on}}{T_{on} + T_{off}} \quad [7.5]$$

$$\delta_p = \sqrt{\frac{2DT}{\pi}} \quad [7.6]$$

The current density is then related to the concentration gradients established in both diffusion layers which can be calculated using Eq 7.7 and 7.8.²

$$j_p = zFN_p = \frac{zFD(C'_0 - C_0)}{\delta_p} \quad [7.7]$$

$$j_s = zFN_s = \frac{zFD(C_0^* - C'_0)}{\delta_s} \quad [7.8]$$

These equations demonstrate that the pulse current density is inversely proportional to the pulse diffusion layer (δ_p), and the ($C'_0 - C_0$) is going to depend on the average current (j_s) density and the stationary diffusion layer (δ_s). Though not explicitly shown in Eq 7.7 and 7.8, the concentrations at the electrode surface and at the boundary between the diffusion layers are related to the overpotential of the system through the Nernst equation. The average current density can also be calculated using Eq 7.9, allowing one to then calculate the pulse current density by rearranging and combining Eq 7.6, 7.7, 7.8 and 7.9.

$$j_m = \frac{j_p T_{on}}{(T_{on} + T_{off})} \quad [7.9]$$

Ibl *et al.* used the above equations to describe the current density used to obtain films of copper, cadmium and silver.² By using short pulse times they were able to deposit at high current densities (250 A) without the formation of powders, which is common at these current densities. The benefit of the high current densities from pulse deposition cited in the literature is the improvement in properties of the material such as smoother and denser deposits and have been demonstrated for a variety of metals.¹ In one case, half the amount of gold can be used to get the same conductivity in integrated circuits as when the gold was deposited using a single current procedure.⁷ In a systematic investigation it was found that higher pulse current densities (or short T_{on}) led to the

growth of larger islands, while long T_{off} led to growth of smaller islands.¹ Thus, by controlling the pulse time one can obtain different film morphology and density.

Based on the brief review given above on galvanostatic pulse deposition it can be seen that the most important parameters are the two time constants T_{on} and T_{off} . An attempt to determine this type of relationship for the potentiostatic case will now be discussed, given the theory developed for chronoamperometric reversal techniques.

7.2 Mathematical treatment of potentiostatic pulse deposition

Unlike the galvanostatic case, nothing has been found in the literature that deals with the theory behind potentiostatic pulse deposition directly. So to get a qualitative picture of the system, an attempt will be made using the theory of chronoamperometric reversal (CAR) technique coupled with the Bewick, Fleischmann and Thirsk (BFT) nucleation theory to obtain use full relationships between the four controllable parameters and the properties of the material deposited. The end goal is to have a similar understanding of the effects that T_{on} and T_{off} have on the deposition as has been done for the galvanostatic pulse deposition in the literature. Throughout this mathematical treatment, simulations run in Excel will be presented, to help the reader visualize the results of the equations derived.

At first this treatment will build up to and follow the chronoamperometric reversal (CAR) theory laid out by Bard and Faulkner.⁸ The first step is to come up with a relationship of current with time when a single potential step is applied. When this differential is solved using three basic assumptions, the Cottrell equation (Eq 7.11) is obtained.

$$i(t) = \frac{nFAD_0^{\frac{1}{2}}C_o^*}{\pi^2 t^2} \quad [7.11]$$

In the case of electrodeposition of Cu_2Sb , n (number of electrons) is 7, F (Faradays constant) is $96485.34 \text{ C mol}^{-1}$, A (area of electrode) is 0.124 cm^2 , D_0 (diffusion coefficient) can be estimated as $10^{-5} \text{ cm}^2 \text{ s}^{-1}$, and C_o^* (starting concentration) will be considered to be 0.05 M . The Cottrell equation gives the simplest picture of the current from the first potential step of a pulse deposition. Eq 7.11 is for a large potential step where the kinetics are limited by mass transfer not electron transfer. In the CAR theory this is modified in order to take into account the equilibrium of the system giving the form of the Cottrell equation shown in Eq 7.12. Eq 7.13 gives the value for ξ . In our system D_{red} equals zero, because the reduced form is deposited on the working electrode. To get a rough estimate of the current behavior in our system the D_{red} will be $10^{-15} \text{ cm}^2 \text{ s}^{-1}$ to try to compensate for deposition a solid that doesn't diffuse from the electrode ($D_{\text{red}} = 0$ does not give a real answer).

$$i(t) = \frac{nFAD_0^{\frac{1}{2}}C_o^*}{\pi^2 t^2 (1 + \xi\theta)} \quad [7.12]$$

$$\xi = \left(\frac{D_{\text{Ox}}}{D_{\text{Red}}} \right)^{\frac{1}{2}} \quad [7.13]$$

$$\theta = \frac{C_{\text{Ox}}(0,t)}{C_{\text{Red}}(0,t)} = \exp \left[\frac{nF}{RT} (E - E^{0'}) \right] \quad [7.14]$$

The effect that the potential has on the current response (Eq 7.12) can be seen in Eq 7.14 which gives the value for θ . The $E^{0'}$ for the deposition of Cu_2Sb will be considered to be -900 mV vs. SSCE, which corresponds to the $E_{1/2}$ of the first reduction peak. The E will be E_r (-1050 mV) for T_{on} and E_r (-425 mV vs. SSCE) for T_{off} .

So far, all the theory has been for homogeneous reactions; i.e. no contribution due to nucleation and film growth. At this point using Eq 7.12 the current profile exponentially decreases to zero. The peak in the calculated current profile of a deposition shown in Figure 7.3 is not predicted using Eq 7.12. A simple approach to this problem was found in the literature where the overall current was the summation of the current from Eq 7.12 and the current predicted taking into account the nucleation and growth of a film.⁹ In doing this, Batina *et al.* provides a form of the BFT equation to use for the nucleation (Eq. 7.15).⁹

$$i_l(t) = \frac{\pi n F M h A N_0 k_g^2 t^2}{\rho} \exp\left(\frac{\pi M^2 A N_0 k_g^2 t^3}{3 \rho^2}\right) \quad [7.15]$$

Some new quantities show up in this equation that are related to the physical properties and growth of the material that is being deposited. For Cu_2Sb M (molecular weight) is 248.85 g mol⁻¹, and ρ (density) is 8.46 g cm⁻². The quantities related to the growth are: h (height), N_0 (nucleation sites), and k_g (lateral growth rate). These can only be determined through rigorous measurements which haven't been performed for this system yet, but Batina *et al.* gives a range of values that show the product $hN_0k_g^2$ should be between 20 - 65 mol² cm⁻⁶ s⁻³.⁹ This value will suffice for our estimate of the current profile created during a pulse potential deposition.

Using the simplistic mathematical treatment above and summing the currents found by solving differential equations for the different systems, Eq. 7.12-7.15 can be used to make a theoretical plot of the current response. Figure 7.3 shows simulated current responses from a potential step that is found during the deposition of a material. The calculated plot shown in Figure 7.3 is a good first approximation to the current behavior seen in Figure 6.7 for the T_{on} . The exponential decay in Figure 7.3 is from Eq 7.12 while the peak arises from Eq 7.15.

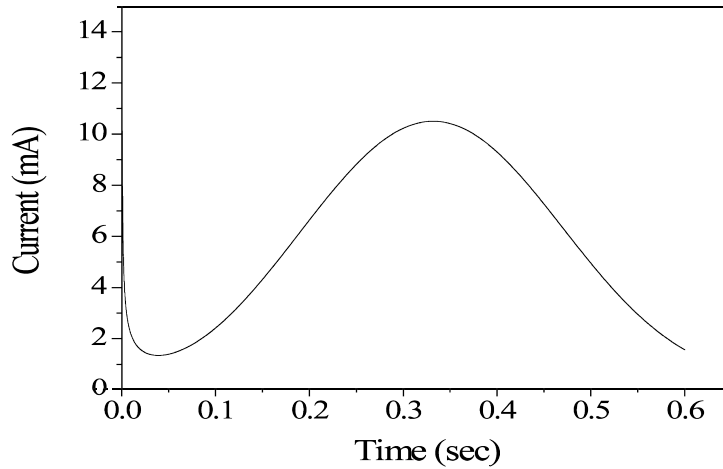


Figure 7.3: Simulated current profile for a single potential deposition using Eq 7.12-7.15. The E_f was -1050 mV and E_r was -425 mV vs. SSCE.

Using the same differential equations that lead to the Cottrell equation, an equation for the solution to the concentration differential can be found. The result obtained by Bard and Faulkner is shown in Eq 7.16. This will be used to estimate the concentration profile during the T_{on} of a pulse deposition.

$$C_{Ox}(x,t) = C_{Ox}^* - \frac{C_{Ox}^*}{(1 + \xi\theta)} \operatorname{erfc} \left[\frac{x}{2\sqrt{D_{Ox}t}} \right] \quad [7.16]$$

There are two competing processes in Eq 7.16. On one hand the concentration is being depleted by the reduction of the species cause by the applied potential, which is represented by the product involving θ . On the other hand, the concentration is being replenished by diffusion of the species to the electrode surface, represented by the product in the error function of Eq 7.16. At short times it the concentration profile is dependent on the electrode potential, while at long times the concentration profile is governed by the diffusion of the species being deposited, diffusing from the bulk solution. The concentration profile established from these two competing process at different values of t are shown in Figure 7.4. At short times there is a dramatic concentration profile where the curve drops off steeply towards the electrode surface.

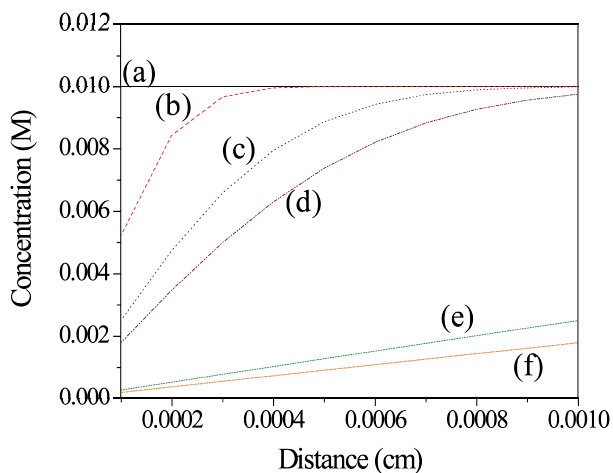


Figure 7.4: A simulated concentration profile for bulk electrolysis deposition using Eq 7.16 for different times. **(a)** before potential was applied, **(b)** 1 ms, **(c)** 5 ms, **(d)** 10 ms, **(e)** 500 ms, and **(f)** 1000 ms. The E_f was -1050 mV vs. SHE.

The discussion, so far, has only described the behavior of a single potential step, which can be used to model a bulk deposition of a film. The next step in achieving the goal of obtaining a mathematical representation of a pulse potential deposition is to apply the E_r after the E_f has been applied. Again, we are going to follow Bard and Faulkner treatment for CAR techniques and use a step function to be able to combine the Eq 7.12-

7.15 with 7.17 to obtain the current during the E_f and E_r .⁸ The current due switching the potential to E_r will also be made up of a faradiac and a non-faradiac process, but as in the case for E_f the time scales we are interested the current will not have any contribution due to the non-faradiac processes. The faradiac current for the E_r given by Bard and Faulkner is related to the potential according to Eq 7.17.⁸

$$i_r(t) = \frac{nFAD\frac{1}{2}C_o^*}{\pi^2} \left\{ \left[\frac{1}{(1 + \xi\theta')} - \frac{1}{(1 + \xi\theta'')} \right] \times \left[\frac{1}{(t - \tau)^{\frac{1}{2}}} \right] - \frac{1}{(1 + \xi\theta')t^{\frac{1}{2}}} \right\} \quad [7.17]$$

The θ' can be calculated using Eq 7.14 and likewise θ'' can be calculated using Eq 7.18.

$$\theta'' = \exp[nf(E_r - E^{0'})] \quad [7.18]$$

Now that we have an equation for the current response due to both E_f and E_r , we can use a step function to combine the two. The equation combining the potential from the two pulses is shown in Eq 7.19. The T_{on} is given by the step function in Eq 7.20 and the T_{off} by Eq 7.21.

$$E(t) = E_f + S(t)(E_r - E_f) \quad [7.19]$$

$$S_\tau(t) = 0 \quad \text{when } t \leq \tau \quad [7.20]$$

$$S_\tau(t) = 1 \quad \text{when } t > \tau \quad [7.21]$$

In our treatment, the step function will be replaced by an “if/then” function in Excel. By doing this, as long as t is less than τ the current will be represented by Eq 7.12-7.15. If t is equal to or greater than τ the current will be represented by Eq 7.17. This simple approach gives the current response shown in Figure 7.5, which is similar to

the experimental result shown in Figure 6.7. The concentration profile of a potentiostatic pulse deposition is not addressed by Bard and Faulkner⁸, but the results discussed above can be used as starting place.

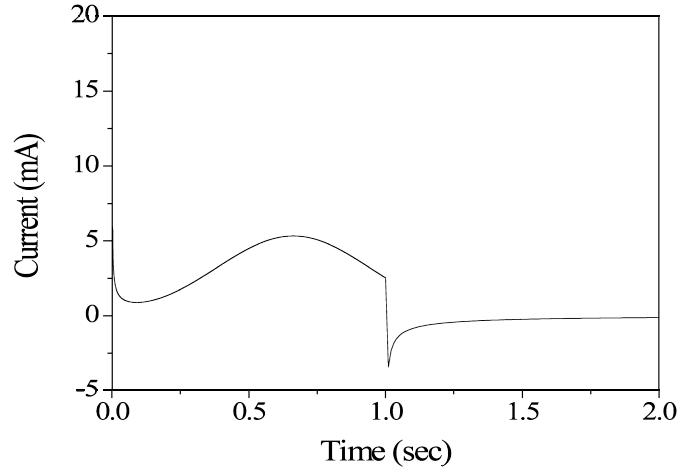


Figure 7.5: Simulated current profile for one pulse cycle. Using a T_{on} and T_{off} of 1 s, and E_f of -1050 mV, and a E_r of -425 mV vs. SHE.

A step function approach to solve the concentration profile will also be used, but with a more complicated $S_\tau(t)$. The complexity arises from the fact that at long T_{off} the concentration gradient will diminish to zero and the concentration profile will look as though the system was never disturbed. To do this, Eq 7.21 needs to be modified to Eq 7.22, and two additional equations (Eq 7.23 and Eq 7.24) are needed.

$$S_\tau(t) = 1 \quad \text{when } \tau \leq t < \tau^* \quad [7.22]$$

$$S_\tau(t) = 0 \quad \text{when } t \geq \tau^* \quad [7.23]$$

$$T_\tau(t) = 0 \quad \text{when } t < \tau^* \quad [7.24]$$

The new time parameter τ^* is determined using the equation for the root square mean displacement. Solving for τ^* using Eq 7.25 with ∇ corresponding to the thickness of the

diffusion layer when the concentration of the oxidize species is zero at the surface of the electrode ($C_{Ox}(0,t) = 0$).

$$\tau^* = \frac{\pi \nabla^2}{2D} \quad [7.25]$$

An equation similar to Eq 7.19 can now be written as Eq 7.26.⁸

$$C_{Ox}(x,t) = C_{Ox}^* + T_\tau(t)(C_{Ox}^I(x,t) + S_\tau(t)C_{Ox}^{II}(x,t - \tau)) \quad [7.26]$$

The concentration profile for T_{on} is the C_{Ox}^I , which Eq 7.16 can be used to solve it. Now a mathematical relationship for C_{Ox}^{II} is needed, which corresponds to replenishing of the concentration during T_{off} . The relationship represented by Eq 7.27 will describe the concentration gradient until Eq 7.23 is true; at which point the concentration has been completely replenished and there is no longer a concentration gradient.

$$C_{Ox}(x,t) = C_{Ox}^* - \frac{C'_{Ox}}{(1 + \xi\theta)} \operatorname{erfc} \left[\frac{x}{2\sqrt{D_{ox}t}} \right] \quad [7.27]$$

It is surprising that the only difference between Eq 7.16 and 7.27 is that the replacement of the C_{Ox}^* with C'_{Ox} . This new concentration can be qualitatively thought of as the C_{Ox}' in Figure 7.2, and can be estimated using Eq 7.28.

$$C'_{Ox}(x,t) = \frac{C_{Ox}^* T_{off}}{\tau^*} = \frac{2D_{ox} C_{Ox}^* (t - \tau)}{\pi \nabla^2} \quad [7.28]$$

This equation could be an over simplification due to the fact that it is based on the idea that at τ^* the concentration is C_{ox}^* and therefore the concentration C_{ox}' is proportional to the fraction of τ^* and T_{off} . The mathematical treatment used above provides a qualitative picture of how the time parameters of the pulse deposition affect the current response and concentration gradients. Differential equations setup and solved specifically for this system would allow a quantitative picture. At this time, this rigorous mathematical treatment would not be beneficial for the project. Using the simple model, a few pulse depositions will be examined using different time parameters related to the experimental results mentioned in Chapter 6. The modeled concentration profile for the experimental time parameters that gave the most crystalline Cu_2Sb is shown in Figure 7.6.

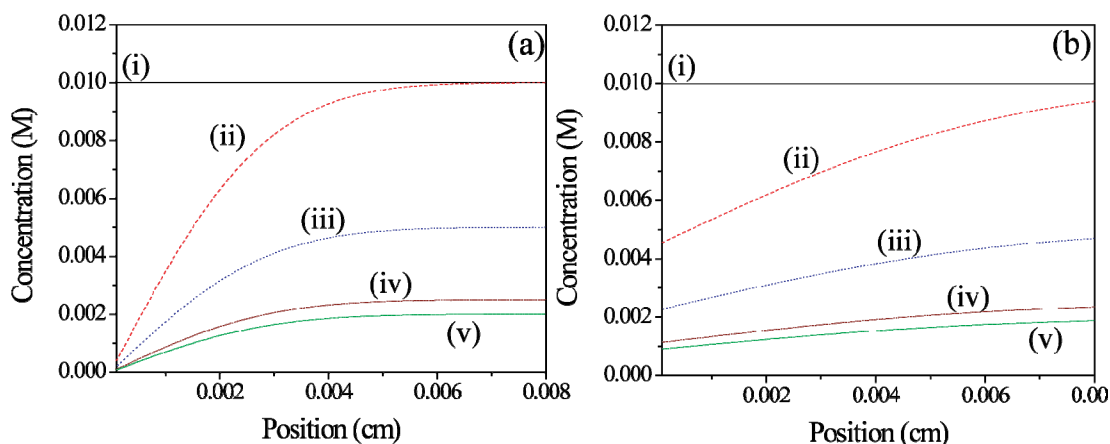


Figure 7.6: Simulated concentration profile for **(a)** single potential deposition and **(b)** pulse deposition using Eq 7.28 with T_{on} of 0.25 s, T_{off} of 1 s, E_f of -1050 mV and E_r was -425 mV vs. SSCE. **(i)** Before potential was applied, **(ii)** first cycle, **(iii)** second cycle, **(iv)** third cycle, and **(v)** fourth cycle.

An interesting observation of Figure 7.6 is that a balance between the T_{on} and T_{off} is reached by the fifth cycle. At this point the change in the concentration gradient caused by T_{on} is similar to the change in concentration gradient from T_{off} . The concentration profile in Figure 7.6 is the opposite from what was thought to be the desired situation

(Figure 7.7). The idea behind using pulse deposition was to eliminate the concentration gradient during the T_{off} , so that the concentration gradient is that seen in Figure 7.7 when a slightly long T_{off} is applied (1.28 s). This led to using T_{off} longer than 1.28 s which ended up providing best crystallinity as discussed in Chapter 6.

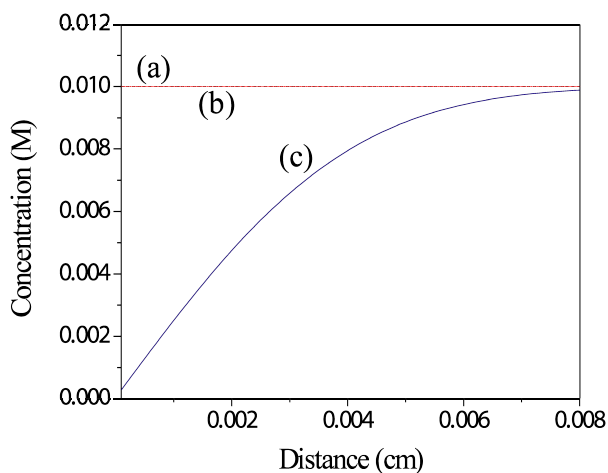


Figure 7.7: A simulated concentration profile of a pulse deposition using Eq 7.28 for different times. **(a)** Before potential was applied, **(b)** T_{off} of 1.28 s, **(c)** T_{on} of 0.5 s. The E_f was -1050 mV, and the E_r was -425 mV vs. SSCE.

7.3 Conclusions

The simplified mathematical approach to modeling the current and concentration behavior of a system during a pulse potential deposition provided insight which directed the experiments discussed in Chapter 6 that were used to develop a procedure to deposit nanowire arrays of Cu_2Sb . From the mathematical treatment it became obvious that the concentration gradient was established quickly and to eliminate it required a T_{off} that is longer than 1.3 s. This mathematical observation was supported by the experimental results presented in Chapter 6. Using the results of the TEM study in Chapter 5 that demonstrated that T_{on} needs to be longer than 2 s, and the results found in this mathematical treatment that T_{off} needs to be longer than 1.5 s, a pulse deposition

procedure that deposit crystalline films and nanowires of Cu₂Sb. The details of the progress to this solution are given in Chapter 6.

7.4 References

- (1) Ibl, N.; Puipe, J. C.; Angerer, H. *Surface Technology* **1978**, *6*, 287.
- (2) Ibl, N. *Surface Technology* **1980**, *10*, 81.
- (3) Podlaha, E. J.; Landolt, D. *Journal of The Electrochemical Society* **1996**, *143*, 893.
- (4) Podlaha, E. J.; Landolt, D. *Journal of the Electrochemical Society* **1996**, *143*, 893.
- (5) Podlaha, E. J.; Landolt, D. *Journal of the Electrochemical Society* **1996**, *143*, 885.
- (6) Puipe, J. C. *Theory and Practice of Pulse Plating*; Electroplators and Surface Finishers Society: Orlando 1986.
- (7) Avila, A. j.; Brown, M. J. *Plating and Surface Finishing* **1970**, *57*, 1105.
- (8) Bard, A. J.; Faulkner, L. R. *Electrochemical methods: fundamentals and applications*; 2 ed.; Wiley: New York, 2001.
- (9) Palomar-Pardavé, M.; Miranda-Hernández, M.; González, I.; Batina, N. *Surf Sci* **1998**, *399*, 80.

CHAPTER 8

BATTERY PERFORMANCE OF Cu_2Sb MATERIAL

8.1 Introduction

The focus of the preceding chapters has been the development of a procedure for the electrodeposition of Cu_2Sb films and nanowires at a single potential from aqueous solutions. That accomplished, this chapter will be concerned with the battery testing of the electrodeposited Cu_2Sb films and nanowires. As mentioned in previous chapters, the ability to directly electrodeposit Cu_2Sb onto the current collector will: (1) improve the characterization of the material during the lithiation and delithiation processes, (2) decrease use of inactive components, and (3) allow the deposition of high surface area Cu_2Sb . Several experimental complications which arose in battery testing small amounts of active material will be addressed prior to a discussing and showing the benefits of testing electrodeposited Cu_2Sb .

8.2 Experimental procedures

Preliminary battery testing was performed in an Argon glove box (O_2 content below 5 ppm) with a CHI600C potentiostat and a three electrode configuration. In this case the reference and counter electrodes were made with lithium metal ribbon (Sigma, thickness 1.15 mm \times width 100 mm, 99.9%). The working electrodes were electrodeposited Cu_2Sb on a variety of copper substrates. For full cell testing the counter electrode is the electrodeposited Cu_2Sb , while the working electrode is LiCoO_2 (Alfa Aesar, 97%) in a slurry of graphite (powder $\leq 20\mu\text{m}$, 99%, Fluka), poly(vinylidene Fluoride) (PVDF, MW 530,000, Aldrich), and 1-methyl-2-pyrrolidinone (NMP, 99%, Aldrich). The slurry made for the graphite electrodes had the following mass percent: graphite (30%), PVDF (10%), and NMP (60%). The slurry made for the cathode material had the following mass percent: LiCoO_2 (30%), graphite (5%), PVDF (5%), and

NMP (60%). According to Yoo *et al.* this slurry recipe result in electrodes with 95% active mass.¹ The slurry was smeared onto copper foil (1.0 mm, 99.999%, Aldrich) and then heated in a vacuum oven at 84 °C for 2 hours. At first the anode material was charged and discharged over a range of 3000 to 0.0 mV vs. Li/Li⁺. This was then altered to 1500 to 5 mV vs. Li/Li⁺ based on the potentials of the lithiation of Cu₂Sb and SEI formation. The full cells were initially tested over a potential range of 2500 to 4500 mV versus Cu₂Sb/Li⁺, which was decreased to 2900 to 3300 mV Cu₂Sb/Li⁺ again based on the lithiation potentials of Cu₂Sb. Two different electrolytes have been used for battery testing. The first and the electrolyte used most often was 1 M LiClO₄ (Aldrich, battery grade, dry, 99.99%) in ethylene carbonate (EC) (Aldrich, anhydrous, 99%), diethyl carbonate (DEC) (Aldrich, anhydrous, 99%), and dimethyl carbonate (DMC) (Aldrich, anhydrous, 99%), in a 1:1:1 ratio by volume. The second electrolyte used was 1 M LiPF₆ (Alfa Aesar, 98%) in EC and DMC in a 1:1 ratio by volume. The charging and discharging rate used range from 5C to C/100, where C (theoretical capacity for the material) is calculated by multiplying the active mass of the electrode by the theoretical specific capacity. This convention for representing current, instead of current density, allows the performance of the battery material to be evaluated by simple analysis of the potential versus time plot. When a material is run at a current that corresponds to 1C then the charge or discharge should take one hour. If it only takes 30 minutes to charge the material at 1C then it becomes evident that only 50% of the expected capacity is present.

As a side note, the CHI potentiostat that was first used for the battery testing of the electrodeposited Cu₂Sb films was found to be unsatisfactory. The ability to count electrons is one of the powerful aspects of electrochemical techniques and is the source of

energy from a battery. The capacity of a battery material is a function of the number of electrons obtained per gram of material, while the power obtained is function of the number of electrons and the voltage at which the electrons are delivered. The leads of the CHI potentiostat are coaxial. This means the main “test” wire, the wire that provides and collects the current/voltage signal is surrounded by the “shield” wire. These wires are separated by a thin insulating layer. The ground wire of a CHI instrument is grounded, so the voltage is zero. With the test wires at voltages other than zero and the shield wires at zero a variable capacitance is formed between the two wires during experiments. The capacitance that is formed is a function of wire length: the longer the wire, the higher the capacitance. The capacitance caused by the wires becomes noise during the charge and discharge of a battery material, shifting the apparent potentials which the material lithiates as well as the measured capacity of the material. In conventional experiments the amount of material tested (and thus the capacity) is large relative to the capacitance of the wires, and therefore the error caused by the wires is not a problem. However, when testing small amounts of material and/or the wires are long the error from the wire capacitance is on the same order of magnitude of the capacity of the material. For the preliminary results obtained using the CHI instrument the capacity of the material (both graphite and Cu_2Sb) did not match literature values. Also, the potentials of the lithiation and delithiation plateaus for both materials did not match what was reported in the literature. This effect can be seen for Cu_2Sb in Figure 8.1a. The determination that this was an instrument artifact and not procedural was confirmed using standard capacitors and resistors.

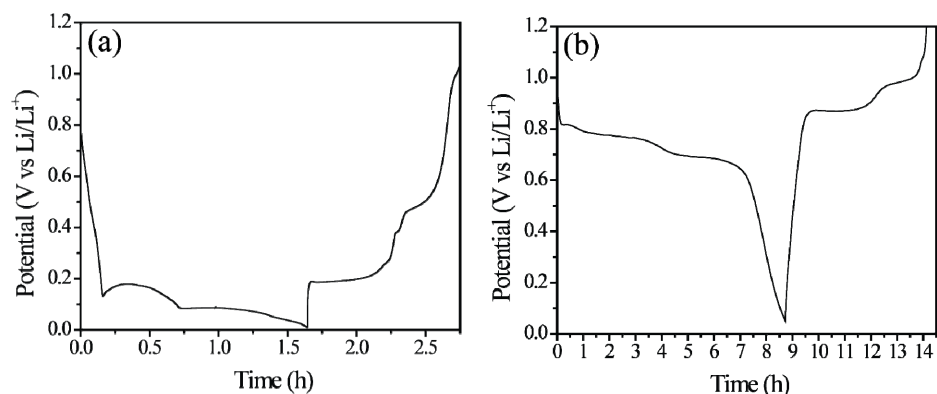


Figure 8.1: Potential profiles of the first cycle of electrodeposited Cu_2Sb run versus lithium metal. **(a)** The potential profile using the CHI instrument and **(b)** using the Gamry instrument. In both cases the Cu_2Sb film was deposited for 10 min and tested in an electrolyte consisting of 1M LiClO_4 in EC, DEC, and DMC (1:1:1 by vol.).

A Gamry Ref3000 potentiostat/galvanostat was purchased after this discovery. The shield wires of the Gamry instrument are driven at the same potential as the test wires, lowering the capacitance effect of the wires. The preliminary testing of Cu_2Sb and graphite electrodes with the Gamry matched the expected results reported in the literature. Unfortunately the capacitance at the start of a test and noise when using long wires still affects the potential actually applied to the test material during the charge and discharge. These two things shift the potential that is actually applied to the test material, and thus hinder the material's cycle performance. This inaccuracy precludes testing in the glove box, forcing the battery testing to be performed in air.

This led to use of Swagelok cells that can be assembled inside an argon glove box and brought into air for testing using short leads. Using the Gamry instrument with short leads sub-microamp current can be controlled with little affect from the undesired consequences of wire capacitance. A schematic of the Swagelok cells can be seen in Figure 8.2. There are two types of cells shown in Figure 8.2. In one of the cells the

center of the union (0.25 inch PFA-420-6, 0.5 inch PFA-820-6) is bored through at the same diameter as the fittings (Figure 8.2a). This allows the cell to be set up in the same configuration as a coin cell. In this configuration two separators are used; the first is a porous polymer film (Celgard C200) the second separator is glass filter paper (Whatman GF/A circles 21 mm diameter). The Celgard acts as an electrically insulating ion conducting layer while the filter paper acts as a reservoir for the electrolyte. The anode material (graphite/Cu₂Sb) is on a copper current collector which is in electrical contact with a stainless steel (SS) rod (McMaster-CARR, 316, precision ground) that allows electric connection to the battery tester to be made. After placing the anode in the middle of the Swagelok union, the electrolyte impregnated separators are placed on top of the anode material. For half cells, lithium metal is then pressed against the separators and a second (SS) rod is used to make electrical connection to the instruments. All of these components have been labeled in the schematic of the Swagelok cell shown in Figure 8.2a. The lithium metal acts as the counter electrode and as a pseudo reference electrode. For full cell testing LiCoO₂ replaces the lithium metal, and becomes the working electrode and the Cu₂Sb is the counter/pseudo-reference electrode.

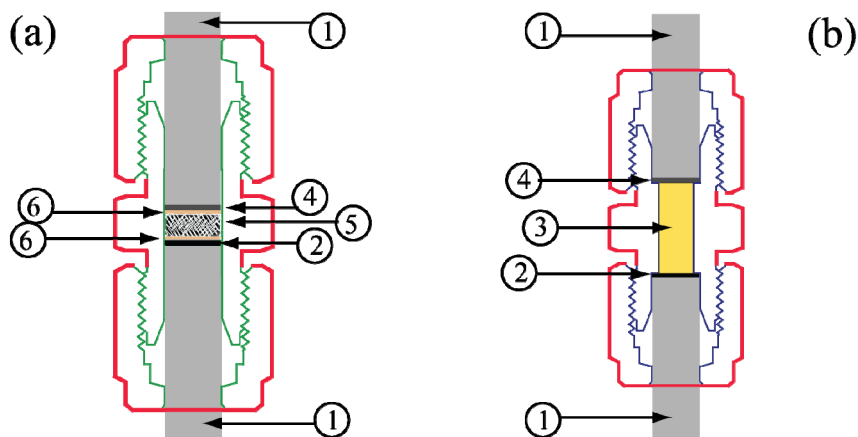


Figure 8.2: Schematic of the (a) first type and (b) second type Swagelok Cells. 1 is the SS rods, 2 is the Cu_2Sb films, 3 is electrolyte solution, 4 is lithium metal, 5 is filter paper soaked in electrolyte, and 6 is Celgard. Details on assembly can be found in the text.

The second Swagelok type cell is schematically represented in Figure 8.2b. The only difference between the two Swagelok type cells is that the center of the Swagelok union has not been bored through in the second type. Thus, there is a smaller diameter in the middle cell, which physically separates the electrodes. The electrolyte of choice is contained in the middle of the union which has the smaller diameter, allowing the material to be tested in a solution environment. This is beneficial for experiments for which the integrity of the material's surface is important. The electrical connection is made following the same procedure used in the first Swagelok type cell. With slight modification the second Swagelok type cells were used to perform the cycling studies on the electrodeposited Cu_2Sb on TEM grids. For this a small screw was tapped into a copper rod (McMaster-CARR, Alloy 145) which was used to hold the TEM grid. The copper rod was used in these experiments and later in all cells on the anode side, because it was found the SS rods leached Fe and Mn into the test cell. Carbon composite TEM grids (copper 200 mesh) were purchased from Structure Probe, Inc. (SPI) and were used to analyze the Cu_2Sb during charge and discharge. The reader is referred to Chapter 5 for

the details of the electrodeposition of Cu_2Sb onto the TEM grids. Following the same configuration of the second Swagelok type cell, a Swagelok t-union can be used. The t-union (0.25 inch PFA-420-3, 0.5 inch PFA-820-3) allows three electrode experiments to be performed, which allows lithium metal to be used as a true reference electrode.

TEM-EDS and SAED data were collected using a Philips CM200 STEM equipped with a Princeton Gamma Tech Prism 2000 energy-dispersive spectrometer operating at an accelerating voltage of 200 kV. Scanning electron microscope (SEM) images of films were taken with a JEOL JSM-6500F equipped with an energy dispersive spectroscopy (EDS) detector from Thermo Electron. An accelerating voltage of 10 kV was used to image the films and collect EDS spectra.

8.3 Voltage profile of electrodeposited Cu_2Sb films

The voltage profile of the lithiation and delithiation of Cu_2Sb is well known, with the crystal structures that are formed at the different stages characterized using powder XRD.²⁻⁶ Upon formation of the solid electrolyte interface (SEI) onto an oxide-free surface, there are two distinct plateaus in the charge and discharge profile. As seen in Figure 8.3 the first charge plateau is at 800 mV vs. Li/Li^+ and the second is at 600 mV vs. Li/Li^+ (-3050 mV vs. standard hydrogen electrode (SHE)), the first plateau is at -2250 mV vs. SHE and the second plateau is at -2450 mV vs. SHE. As discussed in detail in Chapter 2 the first plateau is known to be due to the transformation of Cu_2Sb to Li_2CuSb , and the second plateau is the transformation of the intermediate Li_2CuSb to the final lithiated product of Li_3Sb . The cycle shown in Figure 8.3 is the first cycle and the small amount of charge seen above 800 mV vs. Li/Li^+ is from the breakdown of the electrolyte forming an SEI layer. The formation of Li_2O which is observed from cycling Cu_2Sb

synthesized from conventional solid-state techniques in which oxides are also commonly produced lead to a small plateau at voltages around 2000 mV vs. Li/Li⁺. The absence of a plateau at these potentials in Figure 8.3 is a good indication that any oxide that is formed during the electrodeposition of Cu₂Sb is adventitious oxide on the surface of the film. Cu₂Sb Films more than three years old show the lithiation of the oxide layer in the first charge of the Cu₂Sb. The cycle shown in Figure 8.3 was run at a rate of C/100 (1.1×10^{-6} A cm⁻²), which is sufficiently slow to allow the thermodynamic phases in the lithiation process of Cu₂Sb to be clearly observed. These plateaus become less pronounced as the scan rate is increased and at high rates are not distinguishable from each other.

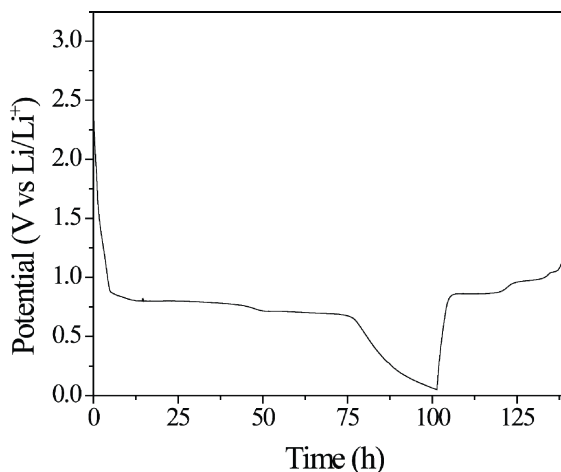


Figure 8.3: The potential diagram of the first lithiation and delithiation of electrodeposited Cu₂Sb film. The film was deposited for 2.5 minutes on a copper substrate, and was cycled using a rate of C/100 (1.1×10^{-6} A cm⁻²) versus lithium in an electrolyte consisting of 1M LiClO₄ in EC, DEC, and DMC (1:1:1 by vol.).

The lithiation shown in Figure 8.3 was started at the OCP (2850 mV vs. Li/Li⁺) and was lithiated to a potential limit of 50 mV vs. Li/Li⁺, and then the polarity was switched and the Li₃Sb was delithiated until the potential limit of 1200 mV vs. Li/Li⁺ was

reached. The upper potential limit of 1200 mV vs. Li/Li⁺ is used because the SEI that is formed on the lithiation step is known to decompose at potentials more positive to this, and thus more irreversible capacity loss would be experienced during cycling. Also seen in Figure 8.3, the lithiation took 100 h while the delithiation only took 40 h. As discussed in the section 8.2, because the Cu₂Sb film cycled in Figure 8.3 was run at C/100 it should take 100 h to lithiate and 100 h to delithiate the film. This means there is a 60% irreversible capacity loss during this cycle, which is common for the first irreversible capacity loss compared to literature values for intermetallics. For example a capacity loss of 54% was reported by Fransson *et al.* for Cu₂Sb in binder cycled at the about the same rate and potential limits.⁵ The potential limits used in Figure 8.3 not only permit the two lithiation steps of Cu₂Sb to occur, but also the plating of lithium metal occurs at potentials close to 50 mV vs. Li/Li⁺. This creates two problems. The first problem is by allowing lithium metal to form, a higher degree of material degradation is observed than if only the lithiation of Cu₂Sb is allowed to occur. This could be one source of the large irreversible capacity loss experienced during the first cycle (Figure 8.3). The second problem is by forming lithium metal the safety benefit of using an intermetallic anode material over graphite is lost. For these reasons the cycle performance of electrodeposited Cu₂Sb films were tested using different potential limits (results are discussed in Chapter 9).

When films of electrodeposited copper antimonide are cycled in a full cell versus LiCoO₂, the two plateaus are still observed (Figure 8.4). The plateaus observed in the full cell are the mirror image of the plateaus obtained from a half cell shown in Figure 8.3 if reflected across an imaginary line at the OCP (2850 mV vs. Li/Li⁺). This is from the

charge and discharge curve for LiCoO₂ only having one characteristic plateau at ca. 3800 mV vs. Li/Li⁺.⁷ Thus, the shape of the charge and discharge curve of Cu₂Sb is superimposed onto the single plateau of LiCoO₂, but since Cu₂Sb is also the counter electrode the potential of the first plateau is 3000 mV vs. Cu₂Sb/Li⁺, and the potential of the second plateau is 3200 mV vs. Cu₂Sb/Li⁺. This means because of the lithiation potential of Cu₂Sb is 500 mV more positive than the potential needed to plate lithium metal (a safety benefit) the potential and power of a battery cell made with Cu₂Sb and LiCoO₂ is lower than the state of the art lithium-ion battery made with graphite. For the cycle shown in Figure 8.4 excess LiCoO₂ was added so the capacity would be limited by the amount of the electrodeposited Cu₂Sb, thus the capacity is similar to that obtained in the half cells of Cu₂Sb (discussed in the next chapter).

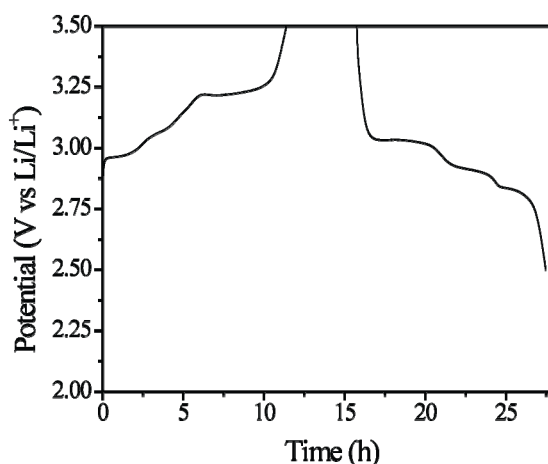


Figure 8.4: Potential profile of full cell with electrodeposited Cu₂Sb versus LiCoO₂ in slurry. The cycle was ran at C/10 from 2500 to 3500 mV vs. Cu₂Sb/Li⁺. The electrolyte consisted of 1M LiClO₄ in EC, DEC, and DMC (1:1:1 by vol.).

The experimental capacity of LiCoO₂ and Cu₂Sb ((140 mAh g⁻¹ and 300 mAh g⁻¹ respectively) reported in the literature mean that the amount of LiCoO₂ in a given cell is more than 2× that of Cu₂Sb based on weight.⁷⁻⁸ This means in a battery made with Si

nanowires which is reported to have a reversible capacity of 3000 mAh g^{-1} only one twentieth of the active mass would be anode material.⁹ Or another way to put it is if a battery had 1 g of active material 0.95 g of that would be LiCoO_2 .

8.4 Lithiation and delithiation of Cu_2Sb electrodeposited onto TEM grids

The technique developed in Chapter 5 (electrodeposition of Cu_2Sb onto TEM grids) was applied to SEM, EDS, TEM and SAED as tools to investigate the processes that occur during the lithiation and delithiation of Cu_2Sb . As was mentioned in Chapter 2, the phases that occur during the transformation between Cu_2Sb and Li_3Sb have been studied with XRD, SEM, and TEM in order to determine the cause of the first irreversible capacity loss.³⁻⁶ Unlike these studies, the Cu_2Sb directly deposited onto the TEM grids, is not in a binder that inhibits the characterization or has to be removed before characterization of the material at the different points of the charge and discharge. Ideally, it also provides a means to directly image the morphology changes that occur during the charge and discharge of Cu_2Sb . Following the procedure in Chapter 5, a 10 s Cu_2Sb electrodeposition onto TEM grids was used for this study, yielding 300-500 nm Cu_2Sb nucleation sites with some overlapping growth between sites. To perform the cycling studies of the Cu_2Sb on the TEM grids, the grids are secured onto a copper rod with a small screw. The copper rod is then inserted into the second type of Swagelok cell shown in Figure 8.2b, so no separator is needed. A separator might affect the morphology changes during the cycling. To establish thermodynamic equilibrium, the material was charged using a multi-step procedure with both constant current and constant potential steps. Starting at the OCP (2850 mV vs. Li/Li^+) a constant current of $1 \times 10^{-6} \text{ A cm}^{-2}$ was applied until the potential for the first plateau was reached. After

reaching the first plateau at 800 mV vs. Li/Li^+ the input signal was switched from a constant current to a constant potential. A potential of 800 mV vs. Li/Li^+ was held until the current density reached $5 \times 10^{-7} \text{ A cm}^{-2}$, then the material was allowed to rest while the OCP was measured. The constant potential/rest was repeated until the change in the OCP during the rest did not exceed 20 mV. The SEM and EDS results of a nucleation site that was charged using this procedure can be seen in Figure 8.5a & b respectively.

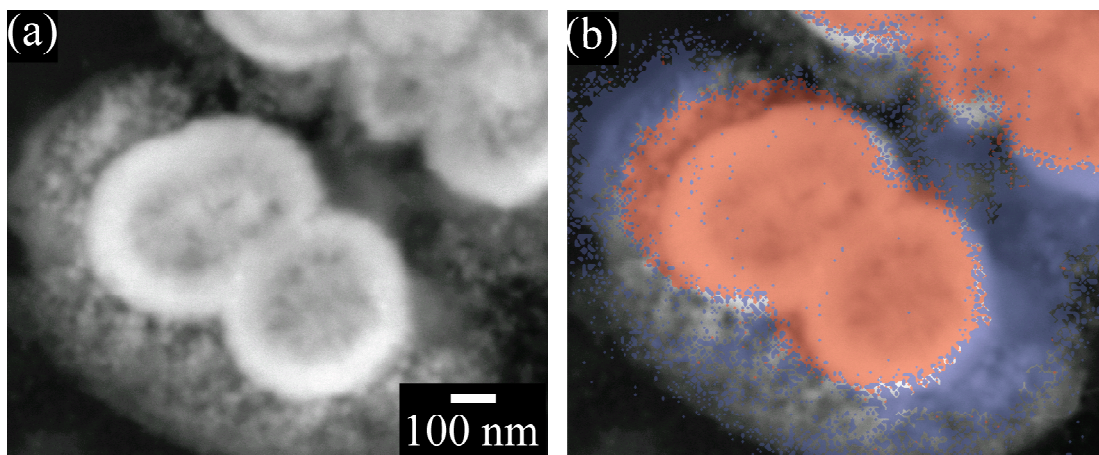


Figure 8.5: (a) SEM image of Cu_2Sb nucleation site after charging to 800 mV vs. Li/Li^+ using a custom charge procedure (see text) to allow thermodynamic equilibrium to be reached. (b) EDS of the SEM image (a) showing the copper rich phase in blue and the antimony rich phase in red. The electrolyte was 1 M LiClO_4 in EC, DEC, and DEM (1:1:1 by vol.).

Following this custom charging procedure the Cu_2Sb nucleation site shown in the SEM image in Figure 8.5a should have completed the first lithiation step leading to Li_2CuSb according to Eq. 1.4. This implies that one mole of copper has been removed for every mole of Cu_2Sb . The extruded copper can be clearly seen as small particles surrounding the original Cu_2Sb site in the SEM image Figure 8.5a. The EDS mapping shown in Figure 8.5b confirms that the small particles surrounding the original sites are copper (the false color for the copper rich region is blue and the antimony rich region is red). The lithium cannot be detected by the EDS, but the copper extruded from the

nucleation site is evidence that lithium was inserted into the material forcing the copper out. While no copper is shown in the false color (poor EDS resolution) of the two phases in Figure 8.5b there is still some copper present in the original site, particularly within the core, which still has the morphology observed from the original electrodeposited Cu_2Sb .

The same procedure just describe was used to thermodynamically charge Cu_2Sb to the second plateau at 660 mV vs. Li/Li^+ . Following Eq. 1.5 during this drop in potential one more mole of copper is extruded while one more mole of lithium is inserted in to the antimony matrix, converting the Li_2CuSb into Li_3Sb . The SEM images of the electrodeposited Cu_2Sb nucleation sites show that the core-shell morphology of the original electrodeposited Cu_2Sb at this potential transformed into a low density site with a uniform composition (Figure 9a). Since not all of the nucleation sites in Figure 9a have lost the original core-shell morphology it is likely that complete thermodynamic equilibrium was not reached. The EDS mapping shown in Figure 9b illustrates not only that more copper has been extruded, but also that the extruded copper is located further away from the nucleation site than was the case for the first charge plateau at 800 mV vs. Li/Li^+ . This is interesting since there should be no driving force for Cu^0 to diffuse further from the nucleation sites by changing the potential.

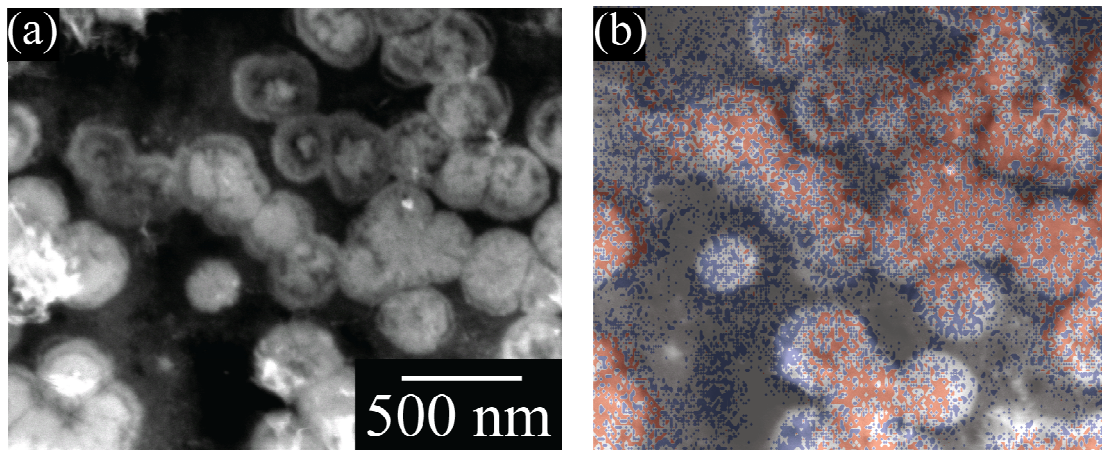


Figure 8.6: (a) SEM image of Cu_2Sb nucleation site after charging to 660 mV vs. Li/Li^+ using a custom charge procedure (see text) to allow thermodynamic equilibrium to be reached. (b) EDS of the SEM image (a) showing the copper rich phase in blue and the antimony rich phase in red. The electrolyte was 1 M LiClO_4 in EC, DEC, and DEM (1:1:1 by vol.).

TEM images of the nucleation sites shown in Figure 8.6 reveal that the density of the sites after reaching equilibrium at the second plateau (660 mV vs. Li/Li^+) has decreased dramatically from the originally electrodeposited Cu_2Sb . Figure 8.7a & b are TEM images of the nucleation sites after being charged to the first and second plateau respectively. The first observation of Figure 8.7a to highlight is the small particles of copper that have been extruded from the nucleation site that are in close proximity to the site. These small particles of copper are quite small and surround the nucleation site evenly. The second observation of Figure 8.7a is the central nucleation site is still too dense for the electron beam of the TEM to penetrate revealing morphology details. After charging to the second plateau completely lithiating the Cu_2Sb to Li_3Sb , the density of the nucleation site has decreased dramatically so that the details of the site's morphology can be observed as the electron beam of the TEM penetrates the entire site. This is further evidence that the central site is lithiated during the extrusion of copper since the densities of Cu_2Sb (8.46 g cm^{-3}), Li_2CuSb (5.37 g cm^{-3}), and Li_3Sb (3.35 g cm^{-3}) decrease as more

lithium is inserted into the antimony matrix.¹⁰ This also excludes the formation of antimony metal as the copper is extruded because the density of antimony metal (6.7 g cm^{-3}) is higher than both lithiated products.¹⁰ The inset in Figure 8.7b shows a magnified view of the morphological details.

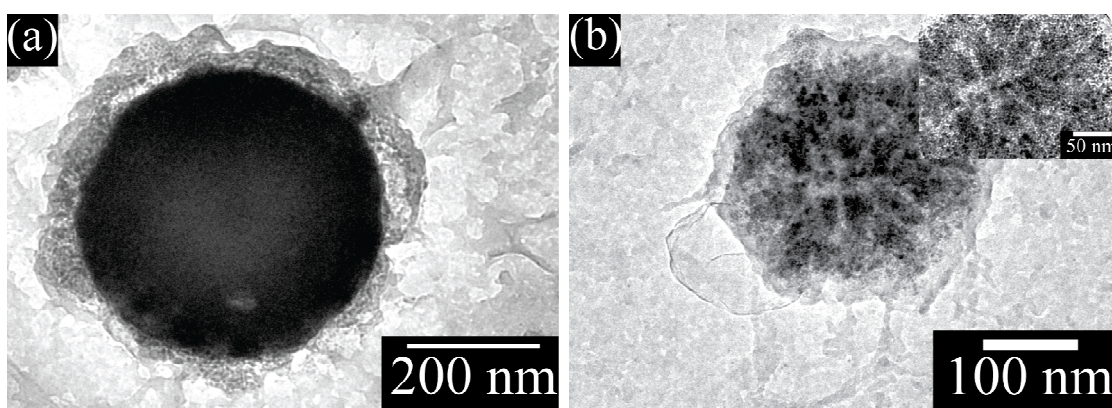


Figure 8.7: TEM images of Cu_2Sb nucleation sites after charging to (a) 800 mV and (b) 660 mV vs. Li/Li^+ using a custom charge procedure (see text) to allow thermodynamic equilibrium to be reached. The inset in (b) is a higher magnification TEM image of the center of the site. The electrolyte was 1 M LiClO_4 in EC, DEC, and DEM (1:1:1 by vol.).

The extruded copper particles surrounding the nucleation sites after charging to the plateaus at both potentials are small and crystalline. HRTEM was used to image the particles on the boarder of the nucleation site shown in Figure 8.7b after charging to 660 mV vs. Li/Li^+ . The edge of the nucleation site with the copper particle surrounding it can be seen in Figure 8.8a. Zooming in on one of these copper particles the radius of the particle was found to be smaller than 10 nm (Figure 8.8b). Although not shown, this small diameter was also found for the extruded copper particles after only charging to the first plateau at 800 mV vs. Li/Li^+ .

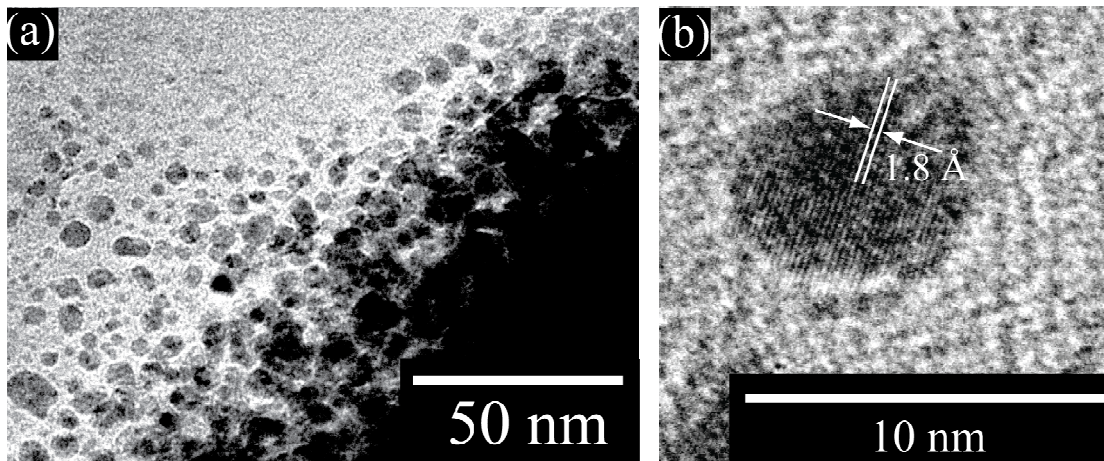


Figure 8.8: TEM images of the extruded copper from a Cu_2Sb nucleation site after charging to 660 mV vs. Li/Li^+ using a custom charge procedure (see text) to allow thermodynamic equilibrium to be reached. **(a)** Shows the edge of the nucleation site with the extruded copper particles. **(b)** A HRTEM image of one of the copper particles. The marked lattice spacing of 1.8 Å matches the (200) of copper. The electrolyte was 1 M LiClO_4 in EC, DEC, and DEM (1:1:1 by vol.).

The lattice fringes that are visible in Figure 8.8b demonstrate the high crystallinity of the particles which match the copper (200) lattice spacing of 1.8 Å. This was confirmed with selective area electron diffraction (SAED) of the particle which was taken and indexed to copper. Again this high crystallinity was observed for copper particles at both charging plateaus. This is the first report in which the extruded copper could be directly imaged due to the absence of a binder used to test the Cu_2Sb . This has two benefits over Cu_2Sb tested in a binder. The first is it allows the material to be imaged without using rough cleaning techniques necessary to remove the binder from the material. The second is the binder acts a physical barrier for the copper diffusion, thus the mobility of the extruded copper seen in these experiments is much different than when a binder is present hindering this process. The large distance between the original nucleation site and the extruded copper could in part explain the irreversible capacity loss.

The same procedure used to reach thermodynamic equilibrium in the experiments discussed above was used to charge the electrodeposited Cu_2Sb to 50 mV vs. Li/Li^+ which is the limiting potential used for the potential profile shown in Figure 8.3. As previously discussed at this potential there is a possibility of plating lithium metal. The SEM images in Figure 8.9 show that there is a large volume expansion experienced by the material when charged to this low potential. The SEM images in Figure 8.9a & b show that the individual nucleation sites have grown into each other with very small amounts of void space present. Also, the expansion has caused a puff effect causing the centers of the original material to be lifted off the substrate. This effect is clear in SEM image from the bottom of the nucleation sites (Figure 8.9a) where the original sites can be distinguished from the expanded material by contrast differences, and it appears that the original material is set back from the surface of the expanded material.

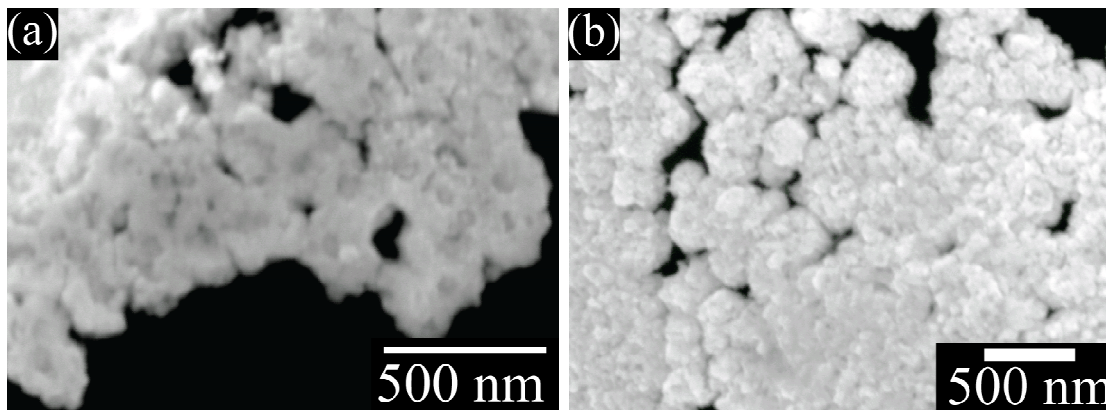


Figure 8.9: SEM images of the (a) bottom and (b) top of Cu_2Sb nucleation sites after charging to 50 mV vs. Li/Li^+ using a custom charge procedure (see text) to allow thermodynamic equilibrium to be reached. The electrolyte was 1 M LiClO_4 in EC, DEC, and DEM (1:1:1 by vol.).

The extensive swelling observed in Figure 8.9a & b is not due entirely to the lithiation of Cu_2Sb , since the final Li_3Sb should have been reached at a potential well positive of this potential. As mentioned, charging the Cu_2Sb down to 50 mV vs. Li/Li^+ leads to plating

of metallic lithium. This accounts for most of the expansion observed in the SEM images shown in Figure 8.9. During the imaging of material charged to 50 mV vs. Li/Li^+ unlike the case at the other two potentials, high magnification images could not be collected due to high charging by the electron beam. This supports the plating of lithium metal, because if the plated metallic lithium was exposed to air during the cleaning process (as was performed with these samples) then the lithium would be converted to Li_2O which would be insulating causing excessive charging during SEM experiments.

After charging to 50 mV vs. Li/Li^+ and discharging to 1200 mV vs. Li/Li^+ using the custom procedure developed to reach thermodynamic equilibrium, the original morphology of the electrodeposited Cu_2Sb is regained. There is a slight difference between the morphology of the electrodeposited Cu_2Sb and that formed after one cycle using this slow procedure. The difference is the separation of the different phases in Figure 8.10a is more pronounced than found in the original electrodeposited Cu_2Sb nucleation sites. This is made clearer by looking at a higher magnification SEM image (Figure 8.10b) which also shows that the layers are more congruent than the layers obtained during the electrodeposition.

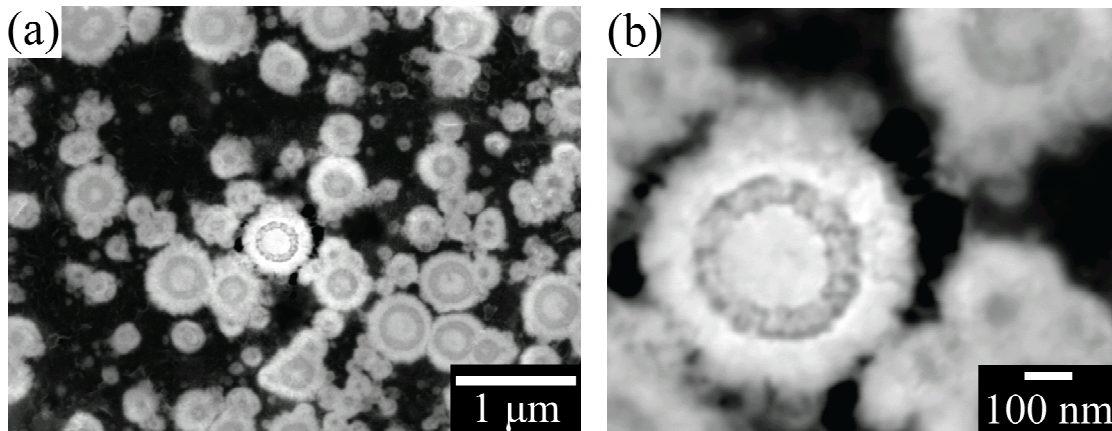


Figure 8.10: (a) SEM image of the bottom of the Cu_2Sb nucleation sites after charging to 50 mV vs. Li/Li^+ using a custom charge procedure (see text) to allow thermodynamic equilibrium to be reached, followed by discharging to 1200 mV vs. Li/Li^+ using the same procedure. (b) A higher magnification SEM image of Cu_2Sb after one cycle. The electrolyte was 1 M LiClO_4 in EC, DEC, and DEM (1:1:1 by vol.).

The observed difference between the electrodeposited Cu_2Sb and the Cu_2Sb formed after one slow cycle is not difficult to explain. The electrodeposited Cu_2Sb is formed in 10 s, which is not enough time to allow the packing and rearrangement necessary to obtain the phase separation and congruency of the slowly formed Cu_2Sb . The reformation of the Cu_2Sb nucleation sites is contrary to what has been reported in the literature recently on the lithiation of Cu_2Sb .¹¹⁻¹² As discussed in Chapter 1 there has been some powder XRD experiments of Cu_2Sb cycled in a binder that suggest Cu_2Sb is not reformed after the first cycle; instead, only a solid solution of $\text{Li}_{2-x}\text{Cu}_{1+x}\text{Sb}$ is formed. The procedure used in this investigation clearly allowed the Li_3Sb to convert completely back to Cu_2Sb . After one cycle at a much faster rate ($C/5$) the original morphology of the nucleation sites was not found. Figure 8.11a & b shows the SEM and EDS mapping image of Cu_2Sb after one cycle at a $C/5$ ($1 \times 10^{-6} \text{ A cm}^{-2}$) rate.

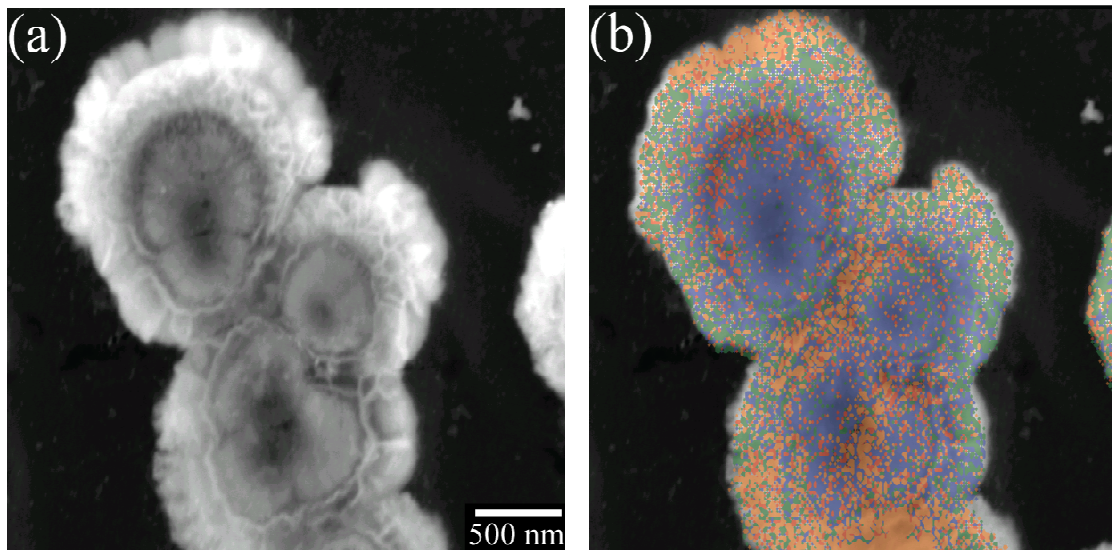


Figure 8.11: (a) SEM image of Cu_2Sb nucleation site after one complete cycle at a rate of $C/5$ ($1 \times 10^{-6} \text{ A cm}^{-2}$). (b) EDS of the SEM image (a) showing the copper rich phase in blue an intermediate phase in green and the antimony rich phase in red. The electrolyte was 1 M LiClO_4 in EC, DEC, and DEM (1:1:1 by vol.).

From the variety of contrast observed in the SEM image of Figure 8.11a it is clear that a rate of $C/5$ is not slow enough for equilibrium to be reached. There are a variety of phases present indicated by the EDS, with the main phases shown in Figure 8.11b. The Cu_2Sb reported in the literature that did not reform Cu_2Sb upon one cycle was ran at similar rates as the results shown in Figure 8.11. This is a clear indication that the processes involved in the delithiation and possibly the lithiation of Cu_2Sb are slow. These results support one hypothesis in the literature that the large irreversible capacity loss experienced by Cu_2Sb during the first cycle is caused by kinetic and not thermodynamic issues.

8.5 Cycling performance of the electrodeposited Cu_2Sb films

The Cu_2Sb cycle performance studies taken with the CHI instrument inside the glove box (Figure 8.1a) had a characteristic drop in capacity after ten cycles. The capacity of the first ten cycles was always found to be less than half of the theoretical

capacity and after 15 cycles only 1% of the capacity remained. As already discussed these results were skewed by instrumental errors causing incorrect potentials to be applied and incorrect capacities to be measured. Using the Swagelok type cells the same potential range and charge rate the cycle performance of an electrodeposited Cu_2Sb film without any binder is shown in Figure 8.12b. There is a clear improvement in cycle performance between the film cycled in the box with the CHI (Figure 8.1a) and the film cycled in the Swagelok cell (Figure 8.12b).

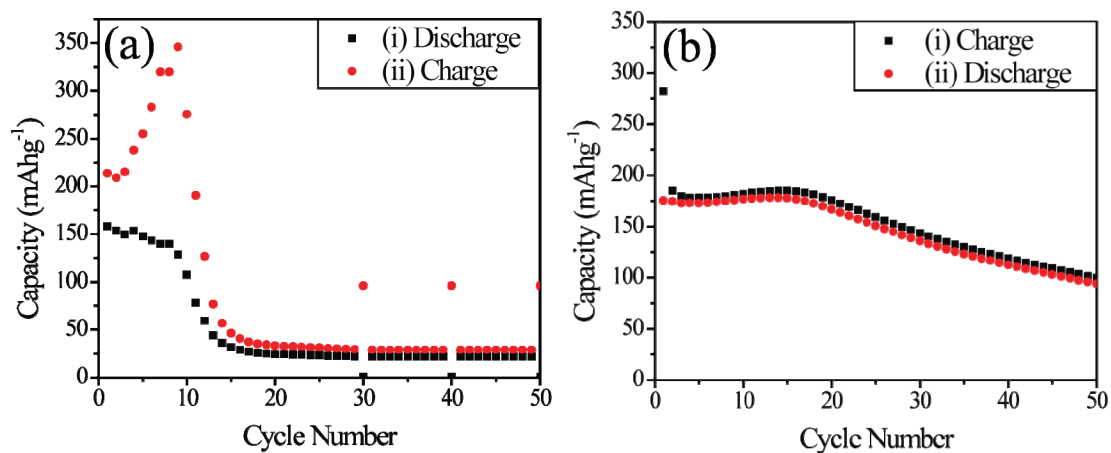


Figure 8.12: The cycling performance of Cu_2Sb half cells performed with (a) the CHI instrument and (b) the Gamry instrument. In both cases the Cu_2Sb was deposited for 10 minutes. The films were both cycled between 1200 and 50 mV vs. Li/Li^+ . The electrolyte used consisted of 1M LiClO_4 in EC, DEC, and DMC (1:1:1 by vol.).

The Cu_2Sb film cycled in Figure 8.12 was deposited for ten minutes, corresponding to a thickness of 32 μm . As seen in Figure 8.12a, even at this rate ($C/5$) the two plateaus corresponding to the lithiation and delithiation of Cu_2Sb can be resolved. After the first cycle the capacity shown in Figure 8.12b drops to 50% of the theoretical capacity, but after a few cycles the capacity increases slightly. This slight increase in capacity results from the pulverization of the Cu_2Sb film which increases the surface area

of the Cu_2Sb and thus increases the amount of Cu_2Sb that can be lithiated at this rate ($C/5$). After the slight increase the capacity starts to fall and continue to decrease for the remaining cycles reaching 10% of the theoretical capacity by the 50th cycle. This decrease in capacity was found to be result from Cu_2Sb pulverization which causes the material to be mechanically cleaved from the current collector. This capacity fade is not reported in the literature where the Cu_2Sb is cycled in a binder, because the binder aids in stabilizing the Cu_2Sb during cycling and keeps the Cu_2Sb in electrical contact with the current collector. In the one example found in the literature in which a thin-film of Cu_2Sb was cycled in the absence of a binder, a higher and more stable capacity was observed but the film thickness was only 50 nm. Decreasing the thickness is one of the first ways that the cycle performance of electrodeposited Cu_2Sb was optimized as discussed in the next chapter.

8.6 Conclusions

In this chapter some of the difficulties that were encountered during the preliminary battery testing of the electrodeposited copper antimonide films and how they were overcome were discussed. With the appropriate equipment and testing procedures it was demonstrated that the electrodeposited Cu_2Sb films had the same lithiation and delithiation potentials as reported in literature during the first cycle. The absence of charge associated with the formation of Li_2O also supported the absence of oxygen impurities when in the bulk of the material. For the first time the extrusion of the copper during the lithiation was directly imaged using electron microscopy techniques without the obstruction of a binder. This allowed the morphology, composition and crystallinity of the Cu_2Sb to be monitored during different stages of the charge and discharge cycle. It

was also demonstrated with the TEM investigation that Cu₂Sb can be reformed after one complete cycle if the rate is slow, supporting the conclusion that the large irreversible capacity loss observed during the first cycle is due to kinetic not thermodynamic issues.

8.7 References

- (1) Yoo, M.; Frank, C. W.; Mori, S.; Yamaguchi, S. *Polymer* **2003**, *44*, 4197.
- (2) Song, S. W.; Reade, R. P.; Cairns, E. J.; Vaughey, J. T.; Thackeray, M. M.; Striebel, K. A. *Journal of the Electrochemical Society* **2004**, *151*, A1012.
- (3) Sarakonsri, I.; Johnson, C. S.; Hackney, S. A.; Thackeray, M. M. *Journal of Power Sources* **2006**, *153*, 319.
- (4) Ren, J. G.; He, X. M.; Pu, W. H.; Jiang, C. Y.; Wan, C. R. *Electrochim Acta* **2006**, *52*, 1538.
- (5) Fransson, L. M. L.; Vaughey, J. T.; Benedek, R.; Edstrom, K.; Thomas, J. O.; Thackeray, M. M. *Electrochemistry Communications* **2001**, *3*, 317.
- (6) Bryngelsson, H.; Eskhult, J.; Nyholm, L.; Edström, K. *Electrochim Acta* **2008**, *53*, 7226.
- (7) Yazami, R.; Lebrun, N.; Bonneau, M.; Molteni, M. *Journal of Power Sources* **1995**, *54*, 389.
- (8) Fransson, L. M. L.; Vaughey, J. T.; Edstrom, K.; Thackeray, M. M. *Journal of the Electrochemical Society* **2003**, *150*, A86.
- (9) Cui, L. F.; Yang, Y.; Hsu, C. M.; Cui, Y. *Nano Letters* **2009**, *9*, 3370.
2010.
- (10) Morcrette, M.; Larcher, D.; Tarascon, J. M.; Edstrom, K.; Vaughey, J. T.; Thackeray, M. M. *Electrochim Acta* **2007**, *52*, 5339.
- (11) Zhang, G.; Huang, K. L.; Liu, S. Q.; Zhang, W.; Gong, B. L. *Journal of Alloys and Compounds* **2006**, *426*, 432.

CHAPTER 9

OPTIMIZING THE BATTERY PERFORMANCE OF Cu_2Sb MATERIAL

9.1 Introduction

The previous chapter introduced the battery testing of electrodeposited Cu_2Sb by discussing some of the difficulties encountered during the preliminary testing. The TEM study in the last chapter also demonstrated the benefit of electrodeposited Cu_2Sb for material characterization during the first cycle. This chapter is going to focus on the optimization of the battery performance of the electrodeposited Cu_2Sb by controlling the thickness of the deposited material, the potential limits used during cycling, and the benefit of high surface morphology. In the process of optimizing the battery performance of the electrodeposited Cu_2Sb in regard to these three parameters, the performance that should be obtained with nanowire arrays of Cu_2Sb will be predicted.

9.2 Experimental procedures

For the charge and discharge experiments presented in this chapter either a Maccor model 4200 test station or a Gamry Ref3000 was used. The working electrodes were electrodeposited Cu_2Sb on a variety of copper substrates and implemented in Swagelok type cells discussed in detail in Chapter 8 (Figure 8.1). The high surface area copper foil (Efoam) came from Circuit Foil Luxembourg Trading Company. It had a thickness of 1.4 mm and an area weight of 185 g m^{-2} . The first cycle of each cell was started at the OCP (2850 mV vs. Li/Li^+) and charged to different lower potential limits that ranged from 50 to 800 mV vs. Li/Li^+ . The cell was then discharged to different upper potential limits ranging from 900 to 1400 mV vs. Li/Li^+ . The Cu_2Sb was then cycled between the chosen potential limits for the remainder of the cycles. The electrolyte used in all cells was 1 M LiClO_4 (Aldrich, battery grade, dry, 99.99%) in ethylene carbonate (EC) (Aldrich, anhydrous, 99%), diethyl carbonate (DEC) (Aldrich,

anhydrous, 99%), and dimethyl carbonate (DME) (Aldrich, anhydrous, 99%), in a 1:1:1 ratio by volume. The charge and discharge rate used for testing the different Cu₂Sb samples in this chapter ranged from 20C to C/100.

9.3 The effect of the Cu₂Sb film thickness of cycle performance

The battery cycling results of Cu₂Sb electrodeposited following the procedure developed in Chapter 3 and 4 is shown in Chapter 8 in Figure 8.12. As mentioned the pulverization of a Cu₂Sb film of this thickness (32 μm) leads to mechanical degradation of the material, which leads to poor capacity retention. Most of the Cu₂Sb cycling performance reported in the literature does not have this problem, because it is cycled in a binder which provides extra mechanical stabilization.¹⁻⁴ One example in the literature where pulse laser deposited Cu₂Sb films were tested, the cycle performance reported was more stable than found in Figure 8.12.⁵ The pulse laser deposited films were only 50 nm which should have less mechanical strain than films that are 32 μm thick leading to improved cycle performance.

In order to investigate the affect that film thickness has on material degradation Cu₂Sb films of different thicknesses were electrodeposited by adjusting the deposition time. Cu₂Sb films were deposited with thicknesses ranging from 100 to 350 nm by depositing from 150 to 600 s. The lower limit of 150 s was chosen based on the time required to cover the entire copper substrate. Figure 9.1a shows a potential profile of the first cycle of a Cu₂Sb film deposited for 150 s, which is representative of all the films used for this investigation. The two lithiation plateaus expected for Cu₂Sb are present at 800 and 600 mV vs. Li/Li⁺ with a small over potential for the two corresponding delithiation plateaus. The absence of charge occurring before 1500 mV vs. Li/Li⁺

demonstrates that the Cu_2Sb film is free from oxygen impurities (Figure 9.1a). The affect of thickness on the capacity retention of electrodeposited films can be seen in Figure 9.1b. In all cases after the first capacity loss, the capacity slightly increases before decreasing, producing a maximum capacity at a certain cycle number. The cycle number of this maximum capacity depends on the thickness of the film. While the trends in the capacity retention (Figure 9.1b) are the same for films of different thicknesses, the number of cycles at which the capacity reaches a maximum is higher for the thinner films. The maximum capacity retention occurred on the 17th cycle for the 350 nm film, the 20th cycle for the 250 nm film and the 25th cycle for the 100 nm film. Interestingly, although the thinnest film has a peak capacity that occurs at a higher cycle number than the thicker films, the thicker films have a higher capacity retention after 50 cycles. The 350 nm Cu_2Sb film retained 55% of the original discharge capacity, where as the 100 nm Cu_2Sb film only retained 40%. This correlates well with the cycle performance of the 50 nm film of Cu_2Sb which was reported to retain 30% of the original capacity after 50 cycles.⁵ The reason that the thinner film performs better than the thick film at low cycle number, but then losses capacity faster than the thick film will be discussed later.

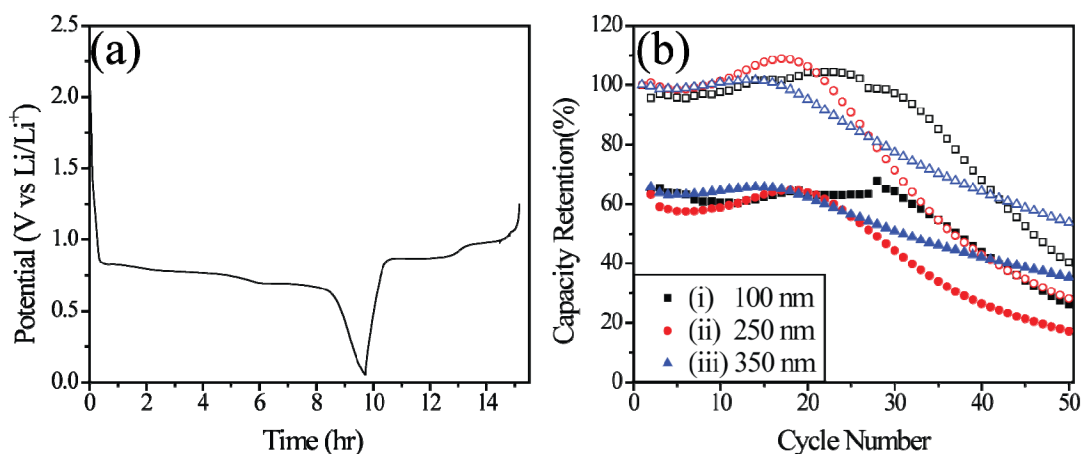


Figure 9.1: (a) The potential profile of a Cu_2Sb deposited for 150 s. (b) The capacity retention of Cu_2Sb films of different film thicknesses. (i) 100 nm Corresponds to a 150 s deposition, (ii) 250 nm corresponds to a 420 s deposition, and (iii) 350 nm corresponds to 600 s deposition. All films were ran in half cells versus lithium metal at a rate of C/10. The open and closed shapes correspond to the discharge and charge capacity retention respectfully. The electrolyte solution used was 1M LiClO_4 in EC, DEC, and DMC (1:1:1 by vol.).

Although the thinnest Cu_2Sb film had the best cycle performance out of the electrodeposited films, retaining only 40% of the original capacity after 50 cycles is still poor cycle performance compared to the Cu_2Sb supported in binder reported in the literature.^{1,3,6-7} This poor performance is directly related to the pulverization of the Cu_2Sb due to the volume changes that occur during the charge and discharge. Without a binder, the pulverization causes mechanical cleavage of the active material off of the current collector, decreasing the amount of material that can still be lithiated and delithiated. After the cells were finished cycling they were taken apart, and the once purple Cu_2Sb films had become black. The thicker films had been cleaved completely off of the current collector. One of the thinner films (after 50 cycles) was cleaned with DEC, acetone and methanol in attempt to remove the SEI layer and analyze with the SEM. Figure 9.2a & b are SEM images of the resulting film. Based on the contrast differences

observed in the SEM image in Figure 9.2a it can be seen that there is two distinct compositions present. Another observation to point out of the SEM image in Figure 9.2a is that the composite that is present has buckled off the copper substrate. At the higher magnification SEM image (Figure 9.2b) distinctly shows one of the compositions appears as bright particles about 100 nm in size that are dispersed within the second darker composition. Using EDS it was determined that the bright spots are composed of copper and antimony while the dark medium they are dispersed in is composed of carbon, oxygen and chlorine.

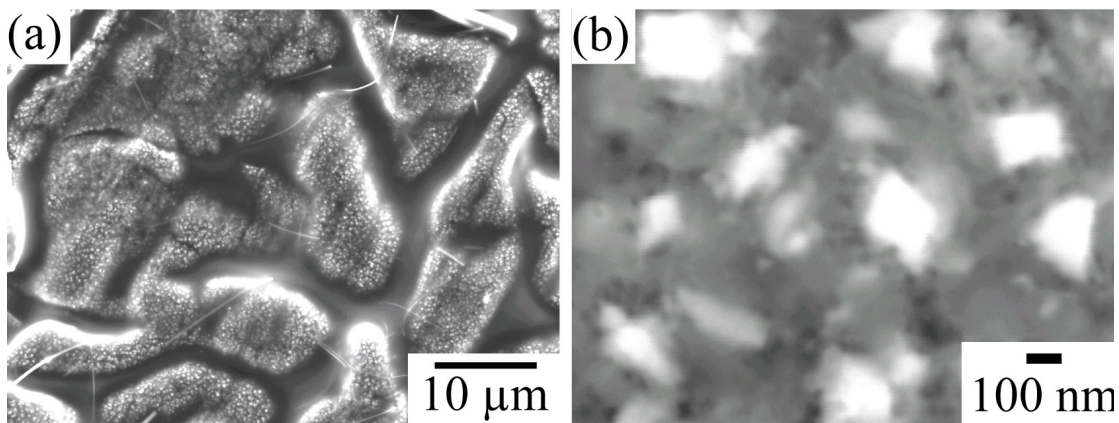


Figure 9.2: SEM images of Cu_2Sb film after 50 cycles in a half cell versus lithium metal. **(a)** A low magnification image showing the entire film is made of up of one phase inter-dispersed into a second phase. **(b)** A high magnification SEM image show the two phases.

The EDS analysis led to the idea that the active material had been dispersed within the SEI that was formed. This was confirmed by imaging the back and edge of the cycled film. Figure 9.3a is an SEM image of the back/bottom of the composite in which the bright particles are evenly dispersed in the SEI throughout the entire thickness. Figure 9.3b shows the cross-section of the film shown in Figure 9.3a. It can be clearly seen that the composite is uniform with a thickness of ca. 1 μm . Thus, it can be concluded that the active material is uniformly dispersed within the SEI which formed

during the cycling. This has a large consequence on the cycle performance of the material. The SEI is not very electrically conducting if it is at all, meaning that as the active material is dispersed into the SEI it is losing electrical contact with the current collector and thus can no longer be lithiated or delithiated. SEM images of electrodeposited Cu_2Sb films after only 10 cycles (not shown), show that the SEI is still a separate layer on top of the Cu_2Sb , which still has its original morphology. The transition from the SEI on top of the Cu_2Sb to the dispersion of the Cu_2Sb within the SEI (Figure 9.2 and 9.3) most likely occurs right after the peak in the capacity seen in Figure 9.1 at which point the pulverization leads to capacity loss.

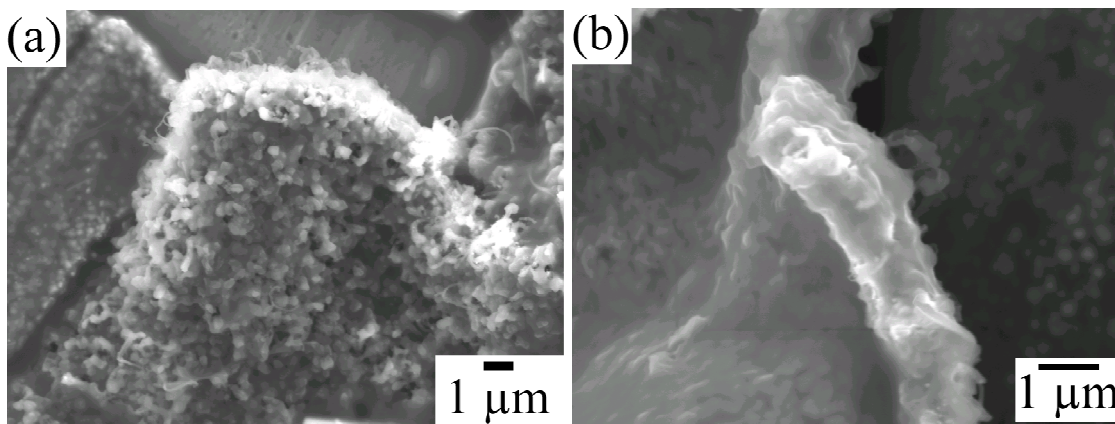


Figure 9.3: SEM images of Cu_2Sb film after 50 cycles in a half cell versus lithium metal. **(a)** A low magnification image shows the entire film is made of up of one phase inter-dispersed into a second phase. **(b)** A high magnification SEM image shows the two phases with the SEI on top of the Cu_2Sb film.

9.4 Cycle performance of Cu_2Sb based on potential limits

The cycling studies discussed in the last section used a lower potential limit of 50 mV vs. Li/Li^+ . This could be one cause of the material degradation since this potential is past the potential needed to fully lithiate Cu_2Sb and was found in Section 8.4 to plate metallic lithium. To determine if this was the cause, the potential limits used to charge and discharge Cu_2Sb were varied. These experiments were performed at a $C/5$ rate

($2.1 \times 10^{-5} \text{ A cm}^{-2}$), which is not slow enough to allow the full lithiation and delithiation of the Cu_2Sb as determined in Section 8.4. Thus, by limiting the lower cut-off voltage to 660 mV vs. Li/Li^+ and not charging to 50 mV vs. Li/Li^+ , the amount of Cu_2Sb that becomes fully lithiated is decreased. Likewise, the fraction of this lithiated material that is delithiated, when an upper cut-off voltage of 1000 mV vs. Li/Li^+ , will be less than when the film is discharged to 1200 mV vs. Li/Li^+ . The potential profiles for Cu_2Sb film cycled between 660 and 1000 mV vs. Li/Li^+ are shown in Figure 9.4a. Using these potential cutoff limits, the processes that occur during a cycle are limited to only the lithiation processes that occur at the two plateaus. The 88% of the charge that was passed during the lithiation of Cu_2Sb films, cycled within these potential limits was obtained during the delithiation step, making the potential profiles very symmetrical (Figure 9.4a). Unfortunately, not lithiating the entire Cu_2Sb film at this rate decreases the capacity obtained, when compared to when the full potential range was used to cycle the films. The discharge capacity retention (open shapes shown in Figure 9.4biii) of Cu_2Sb films cycled between 660 mV and 1200 mV vs. Li/Li^+ was more stable than when the full potential range was used. After 50 cycles, the specific capacity of a Cu_2Sb film cycled with the new potential limits is 90 mAh g^{-1} (Figure 9.4biii), which corresponds to a retention of 60% of the original discharge capacity. Using the full potential range, only 40% of the original discharge capacity is retained after 50 cycles, which correlates to a specific capacity of 92 mAh g^{-1} . It is interesting that even though the capacity retention behavior is very different between Figure 9.1bi and Figure 9.4biii the specific capacity is indistinguishable. At the high potential end the potential shoots up fast after 1100 mV vs. Li/Li^+ , the main reactions that occur above this potential involve only the SEI and not

Cu₂Sb. Using 660 mV vs. Li/Li⁺ but discharging to 1200 mV vs. Li/Li⁺ decreased the capacity retention to only 20% after 50 cycles (Figure 9.4bii). The decrease in capacity retention could be from the SEI being decomposed at these higher potentials, and thus reforming during the charge on the newly exposed material. A lower cutoff potential of 600 mV vs. Li/Li⁺ was used to see if a higher capacity could be obtained. The cycling results for Cu₂Sb films cycled between 600 mV to 1200 mV vs. Li/Li⁺ are shown in Figure 9.4bi. After 50 cycles 45% (101 mAh g⁻¹) of the original discharge capacity is obtained. This is the highest specific capacity obtained so far for electrodeposited Cu₂Sb films. To see if this could be improved, a new lower cutoff potential of 500 mV vs. Li/Li⁺ was also investigated.

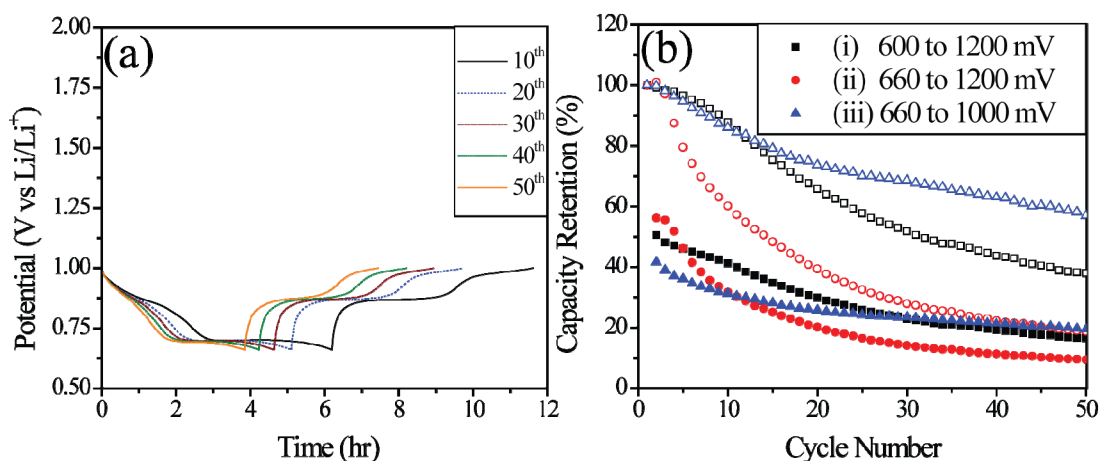


Figure 9.4: (a) The charge and discharge profiles of a Cu₂Sb films cycled between: 600 to 1000 mV vs. Li/Li⁺. (b) Cycle performance of Cu₂Sb films (i) cycled between 600 to 1200 mV vs. Li/Li⁺, (ii) 660 to 1200 mV vs. Li/Li⁺, and (iii) 660 to 1000 mV vs. Li/Li⁺. The films were cycled in 1 M LiClO₄ EC, DEC, DMC (1:1:1 by vol.) electrolyte at C/5 (2.1×10^{-5} A cm⁻²). The open and closed shapes correspond to the discharge and charge capacity retention respectfully.

The potential profile of the charge and discharge of Cu₂Sb films cycled between 500 mV and 1200 mV vs. Li/Li⁺ are shown in Figure 9.5a. While the 80% of the charge passed during the lithiation is obtained during the delithiation for the 5th cycle, by the 25th cycle

only 63% is obtained. The decrease in symmetry upon cycle number when a lower cutoff of 500 mV vs. Li/Li^+ was not observed when 660 or 600 mV (Figure 8.4bi & ii) cutoff was used. The main source of the decrease in symmetry is due to the decrease in the lowest charge and discharge plateaus (600 mV vs. Li/Li^+). After 35 cycles, 25% (63 mAh g^{-1}) of the original discharge capacity was obtained, which was the lowest obtained. A Cu_2Sb film was cycled between 500 and 1200 mV vs. Li/Li^+ (Figure 9.5bi) to test the hypothesis that a lower upper cut-off potential improves cycle performance found previously using the lower cutoff of potential of 660 mV Li/Li^+ . These new potential limits had the worst cycle behavior of all the different limits tested. The capacity retention behavior of the Cu_2Sb films charged to 500 mV vs. Li/Li^+ (Figure 9.5bi) is similar to the behavior seen when the lower cutoff was 50 mV vs. Li/Li^+ (Figure 9.1b). This shape in capacity retention is indicative of pulverization and was not present when the lower potential cutoff was 600 or 660 mV vs. Li/Li^+ (Figure 9.4b). This indicates that the mechanism that led to the pulverization of the electrodeposited Cu_2Sb films producing the SEI composite shown in Figures 9.2 and 9.3 occurs somewhere between 500 and 600 mV vs. Li/Li^+ . From these results it was determined that the best potential limits to used to cycle electrodeposited Cu_2Sb films are 600 to 1000 mV vs. Li/Li^+ . So far the best cycle performance of electrodeposited Cu_2Sb is obtained with thin films cycled within this limited potential window. Now the battery performance of electrodeposited Cu_2Sb on high surface area substrates will be examined.

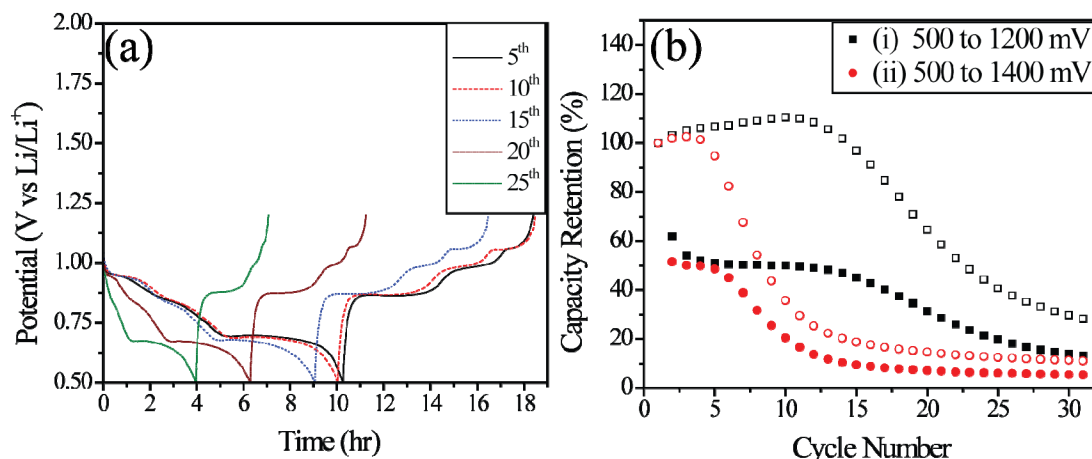


Figure 9.5: (a) The charge and discharge profiles of a Cu_2Sb films cycled between: 500 to 1200 mV vs. Li/Li^+ . (b) Cycle performance of Cu_2Sb films (i) cycled between 500 to 1200 mV vs. Li/Li^+ , and (ii) 500 to 1400 mV vs. Li/Li^+ . The films were cycled in 1 M LiClO_4 EC, DEC, DMC (1:1:1 by vol.) electrolyte at $C/5$ ($2.1 \times 10^{-5} \text{ A cm}^{-2}$).

9.5 Cycling performance of high surface area Cu_2Sb

As mentioned in Chapter 2 one of the strengths of electrodeposition is that it can be used to deposit materials on substrates with a variety of sizes and shapes. Up until now, all the battery testing of electrodeposited Cu_2Sb discussed has been on films of varying thickness on flat copper substrates. While most lithium-ion batteries use thin film technology, there are many improvements associated with using high surface areas and small morphologies, which was discussed in Chapter 1. Under this direction, using the electrodeposition procedure developed in Chapters 3 and 4, Cu_2Sb was deposited onto a high surface area (HSA) copper foam. Comparing the density of the foam given by the manufacture to the density of copper it was determined that 98% of the foam is void space which correlates to a $68\times$ increase in surface area versus the corresponding copper foil. SEM images of the copper foam after Cu_2Sb was deposited on it are shown in Figure 9.6. The structure and amount of void space in the foam is clearly seen in Figure

9.6a, while the details of the morphology of the web that makes up the foam can be seen in Figure 9.6b.

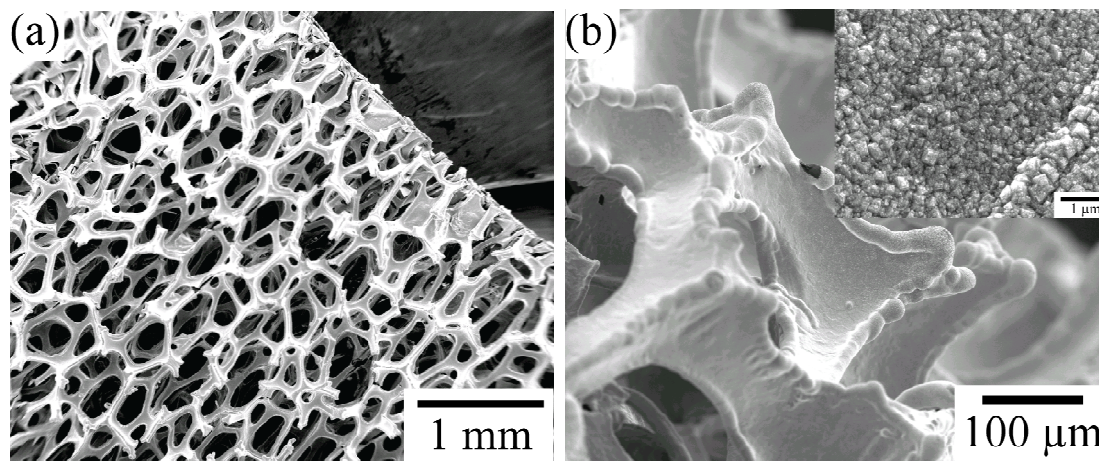


Figure 9.6: SEM images of high surface area copper sponges. **(a)** Low magnification image showing over all structure of the copper sponge. **(b)** High magnification image of sponge with Cu_2Sb electrodeposited onto it. The inset shows the morphology of the electrodeposited Cu_2Sb .

Two observations on the electrodeposition of Cu_2Sb onto the HSA copper foam need to be pointed out. First, the variation in current density caused by the edges of the foams web lead to excess deposition as would be expected (Figure 9.6b) from the presence of a higher electric field. Besides this edge effect, the electrodeposition of Cu_2Sb is uniformly covered on the web with no discontinuities (this is different than Cu_2Sb deposited on thin films). The second observation is the morphology of the electrodeposit shown in the inset of Figure 9.6b is the same morphology is observed as when Cu_2Sb is deposited onto flat copper substrates (Figure 4.5) and TEM grids (Figure 5.4a)

From the results in the earlier sections of this chapter, the battery performance of the Cu_2Sb electrodeposited onto the HSA foam was tested between 600 and 1200 mV vs. Li/Li^+ . Figure 9.7b shows the cycle performance of this material. During the lithiation of

the material a rate of $C/5$ ($2.1 \times 10^{-5} \text{ A cm}^{-2}$) was used for all 90 cycles. The rate at which the material was delithiated was varied according to Table 9.1.

Table 9.1- The different discharge rates used during the cycle study of the Cu_2Sb electrodeposited onto HAS copper foam.

Cycle #	C-rate	Current Density A cm^{-2}
1-30	$C/5$	2.1×10^{-5}
31-50	C	1.0×10^{-4}
51-60	$5C$	5.2×10^{-4}
61-70	$10C$	1.0×10^{-3}
71-80	$15C$	1.6×10^{-3}
81-90	C	1.0×10^{-4}

Unlike, the Cu_2Sb deposited on smooth copper foil, the discharge capacity of the Cu_2Sb on the HSA copper foam is stable at 50% of the theoretical capacity at a rate of $C/5$. When the discharge rate was increased from $C/5$ to $1C$, the material only experienced a 12% drop in capacity. Instrumental errors are thought to be the cause of the drop in capacity observed for the 50th cycle (Figure 9.7b). After this, the discharge rate was increased to $5C$ for which no drop in capacity was observed. The rate was further increased to 10 at which point a 35% loss in capacity was observed between $5C$ and $10C$ discharge rates. Although the charge rate was maintained at $C/5$, the $10C$ discharge rate did not allow all of the material to be discharged fully, so after 4 cycles at this discharge rate the charge only took one hour instead of 5 (Figure 9.7a). In this case, the shorter than expected charge time is not due to material degradation, but to the material not being fully discharged. Zooming in on the discharge step (the inset of Figure 9.7a), which only lasted 15 s it can be seen there is a sloping plateau observed center at 1000 mV vs. Li/Li^+ . While not all of the material was discharged at this rate, a specific capacity of 100 mAh g^{-1} was obtained for at least ten cycles. The next increase in rate to $15C$ ($1.6 \times 10^{-3} \text{ A}$

cm^{-2}) was accompanied by a 82% drop in capacity (most likely due to the material not being discharged fully), but the capacity was regained in the last ten cycles when the discharge rate was decreased back to 1C. Between the last ten cycles ran at 1C and the 20th to 50th cycle ran at 1C there was only a 1% capacity loss.

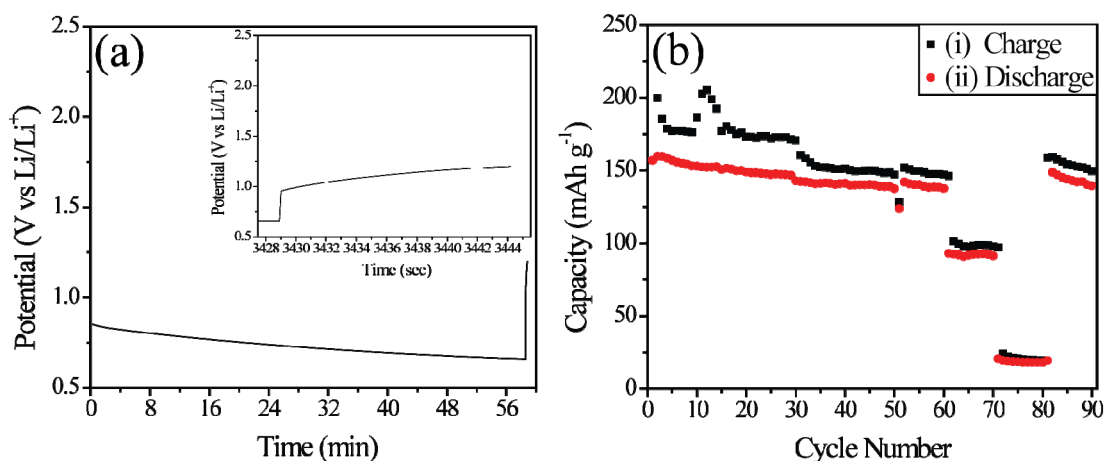


Figure 9.7: (a) Voltage profile of the Cu_2Sb on the HSA copper sponge substrate charge at $C/5$. The inset shows the details of the voltage profile of the discharge at $10C$. (b) Cycle performance of electrodeposited Cu_2Sb on copper sponge (i) charged and discharged at a $C/5$ rate and (ii) discharged: at $C/5$ for the first 30 cycles, C for 20 cycles, $5C$ for 10 cycles, $10C$ for ten cycles, $15C$ for ten cycles, and C for the final 10 cycles.

The cycle performance of the Cu_2Sb electrodeposited onto the HSA copper foam far exceeds that of Cu_2Sb deposited onto smooth substrates. The mechanical stability observed in Figure 9.7b is from the thin deposit on the high surface area substrate, causing more of the active material to be on the surface than deep with the bulk of a film. While the volume expands in three dimensions when lithium is intercalated into the Cu_2Sb , the largest volume expansion is along the (001) direction (by crystal structure), which is also the preferred orientation of the electrodeposited Cu_2Sb . Thus, the mechanical strain of thin films of Cu_2Sb on the HSA substrate is much less than a thick film in which a large portion of the active material is below the surface of the film. The

exceptional rate performance demonstrated in Figure 9.7b is also based on most of the active material being present on the surface. Since, as described in Chapter 2, the shorter the lithium-ion diffusion path, the faster the material can be charge and discharged. In addition, there is less concentration polarization because of the small dimensions. The performance of the Cu₂Sb on the HSA copper substrate reinforces the idea that nanowire arrays of Cu₂Sb will outperform thin films and even the Cu₂Sb on the HSA substrate, based on the surface area of the nanowires having a surface area 7× larger than the HSA foam.

9.6 Cycle performance of Cu₂Sb nanowires

The battery performance of Cu₂Sb nanowire arrays grown in commercial templates following the pulse deposition procedure reported in Chapter 6 was examined in three neck round bottom flask in a argon glovebox and in the Swagelok cells outside of the glovebox. Before the arrays of nanowires can be tested the template is removed by soaking it in a solution composed of 3.5% by volume H₃PO₄, and 45 g l⁻¹ CrO₃ for ca 20 h. Figure 9.8a shows the potential profile of a nanowire array of Cu₂Sb ran versus lithium metal in a three electrode cell at a current of 1×10⁻⁷ A. The two plateaus that are usually observed during the charging of Cu₂Sb are not present; instead there is a small plateau at 700 mV vs. Li/Li⁺ (Figure 9.8a). However, there is slight plateau centered at 1000 mV vs. Li/Li⁺ during the discharge cycle (Figure 9.8a). As discussed in Chapter 8 the long wires required to test inside the glove box causes serious problems when low currents (less than 1×10⁻⁶ A) are used. This is believed to be the cause of the abnormal shape of the potential profile in Figure 9.8a. Because of the necessity of passing low currents to test the nanowire arrays of Cu₂Sb the commercial templates were attached to

stainless steel (SS) rods so the nanowire arrays could be tested in the Swagelok type cells outside of the glove box. After the templates were attached to the SS rods, the nanowire arrays of Cu_2Sb were deposited following the procedure given in Chapter 6. Figure 9.8b shows the potential profile of a Cu_2Sb nanowire array tested in a Swagelok cell after the template was removed, and ran with a current of 2.5×10^{-7} A. Unfortunately, not all of the template was removed as the large amount of charge passed above 1500 mV vs. Li/Li^+ is the lithiation of the Al_2O_3 template. The inset in Figure 9.8b shows a zoomed in image of the potential profile which shows a slight plateau at 800 mV vs. Li/Li^+ during the charge, but during the discharge a plateau is seen at 400 mV vs. Li/Li^+ .

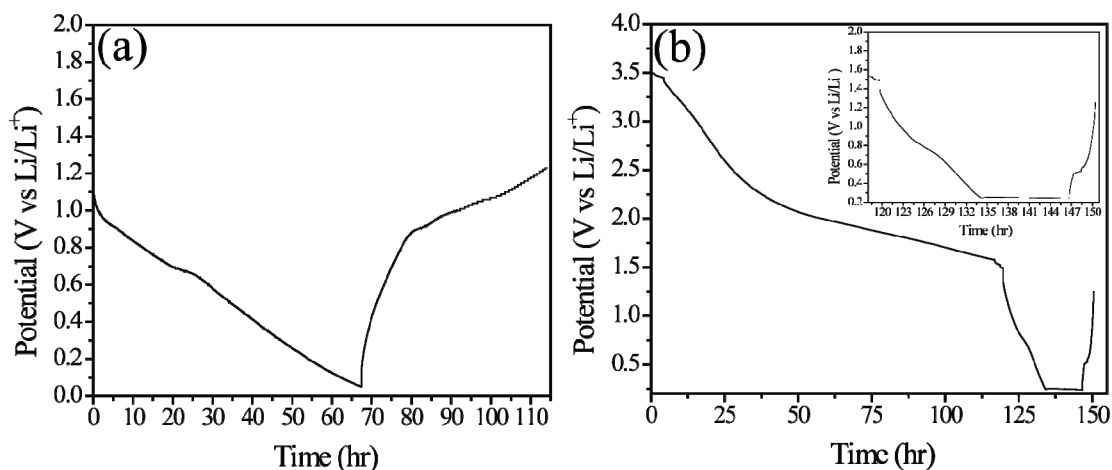


Figure 9.8: Cycle performance of Cu_2Sb nanowire arrays **(a)** cycled in a three electrode cell in side glove box at 1×10^{-7} A, **(b)** and in a Swagelok type cell outside of the glovebox at 2.5×10^{-7} A. The Cu_2Sb arrays were cycled between 50 and 1200 mV vs. Li/Li^+ . In both cases lithium metal was the counter and reference electrode.

Successful battery testing of Cu_2Sb nanowire arrays has yet to be achieved because of the two complications described above. The first is based on the limitation of the instruments and the size of a commercial template. To pass currents that are not significantly affected by instrumental errors a large template/more material should be tested. The second complication is in order to test the nanowire array directly on the

current collector, on which they were grown; all of the template must be removed. This second complication requires the soaking time and solution for which the AAO template is removed to be optimized. The Cu_2Sb nanowire array, which the potential profile is shown in Figure 9.8a, was cycled ten times (46 days) and then washed in DMC, acetone and methanol in order to image the array using SEM. The SEM image in Figure 9.9a is a cross section of the Cu_2Sb array tested in Figure 9.8a. This image shows that the wires are still intact and are surrounded by an SEI layer which was not removed by the washing procedure. Figure 9.9b is a higher magnification of the Cu_2Sb array which shows that the wires are still intact with no sign of pulverization.

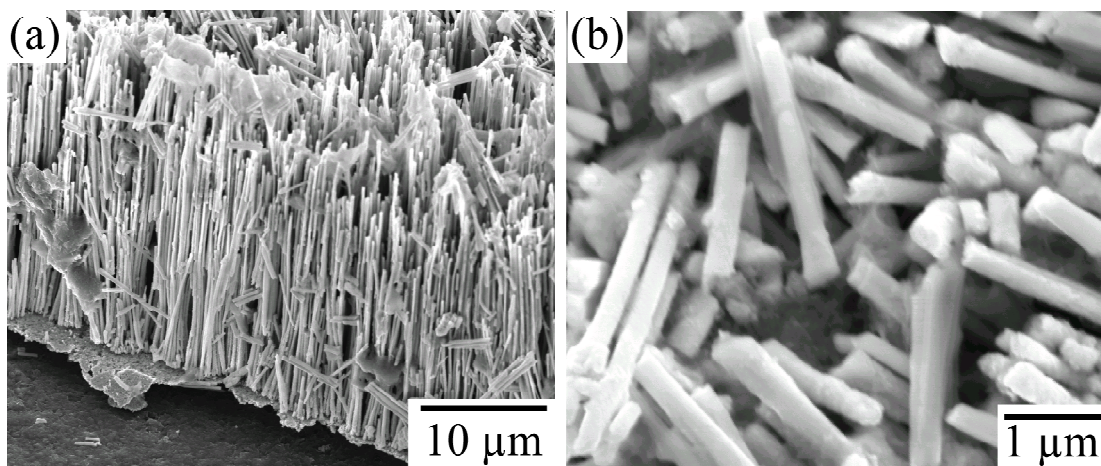


Figure 9.9: SEM images of Cu_2Sb nanowires arrays after being cycled ten times. **(a)** Low magnification image showing cross section of array. **(b)** High magnification image of the wires in the array.

9.7 Conclusions

In this chapter, the battery testing that was used to optimize the cycle performance of electrodeposited Cu_2Sb was discussed. It was first demonstrated that without a binder providing mechanical stability, Cu_2Sb films pulverize after a certain number of cycles. The number of cycles it takes to cause the pulverization was found to be dependent on the thickness of the Cu_2Sb films and the rate at which they were cycled. It was also

determined that the pulverization only occurs if the Cu₂Sb is charged to a potential limit lower than 600 mV vs. Li/Li⁺. A different degradation mechanism is thought to occur at high potentials (1200-1400 mV vs. Li/Li⁺) during the discharge step. In this case it is thought that the SEI which is formed during the lithiation is being destroyed at these potentials, which exposes the active material allowing more SEI to form and further charging. The improvement in battery performance of materials with thin morphologies and high surface areas was demonstrated by the excellent performance of Cu₂Sb electrodeposited onto HSA copper foam. The material was cycled at rates as high as 15C, but besides the first irreversible loss and even after 90 cycles only a 6% capacity loss was experienced with the capacity at still at 50% of the theoretical capacity. The battery performance testing of the Cu₂Sb nanowires array unfortunately was complicated by two procedural issues. After these issues are addressed, the cycling performance of the Cu₂Sb nanowire arrays is expected to exceed that observed for the Cu₂Sb electrodeposited onto HSA foam.

9.8 References

- (1) Sarakonsri, I.; Johnson, C. S.; Hackney, S. A.; Thackeray, M. M. *Journal of Power Sources* **2006**, *153*, 319.
- (2) Ren, J. G.; He, X. M.; Pu, W. H.; Jiang, C. Y.; Wan, C. R. *Electrochim Acta* **2006**, *52*, 1538.
- (3) Fransson, L. M. L.; Vaughey, J. T.; Benedek, R.; Edstrom, K.; Thomas, J. O.; Thackeray, M. M. *Electrochemistry Communications* **2001**, *3*, 317.
- (4) Bryngelsson, H.; Eskhult, J.; Nyholm, L.; Edström, K. *Electrochim Acta* **2008**, *53*, 7226.
- (5) Song, S. W.; Reade, R. P.; Cairns, E. J.; Vaughey, J. T.; Thackeray, M. M.; Striebel, K. A. *Journal of the Electrochemical Society* **2004**, *151*, A1012.
- (6) Morcrette, M.; Larcher, D.; Tarascon, J. M.; Edstrom, K.; Vaughey, J. T.; Thackeray, M. M. *Electrochim Acta* **2007**, *52*, 5339.
- (7) Zhang, G.; Huang, K. L.; Liu, S. Q.; Zhang, W.; Gong, B. L. *Journal of Alloys and Compounds* **2006**, *426*, 432.

CHAPTER 10

CONCLUSIONS

10.1 Single potential deposition of Cu₂Sb thin films from aqueous solutions

The work presented in this thesis covered the development of a procedure for the electrodeposition of crystalline copper antimonide films and nanowires from aqueous solutions at a single potential. This material was synthesized in order to examine the solid-state transitions that Cu₂Sb goes through during the lithiation and delithiation as an anode material for lithium-ion batteries. The electrodeposition procedure developed was desired as a low cost fabrication route for lithium-ion battery materials and devices. The first step of achieving this goal required investigating the relationship between the solution speciation and the electrochemistry of antimony citrate and copper citrate solutions. In Chapter 3, the known speciation data for antimony citrate and copper citrate was used to describe the cyclic voltammograms of the solutions at different pH values. It was found that the reduction potential of antimony shifted to more positive potentials as the pH was increased, because of the deprotonation of the antimony citrate complexes. Also, the reduction potential of Cu²⁺ shifted to more negative potentials as the pH is increased, because of the different copper citrate species present at different pH values. These trends caused the reduction of antimony and copper to converge to a similar potential in a citrate solution at a pH 6. Using the optimized solution composition, the deposition parameters were optimized in order to deposit reproducible crystalline Cu₂Sb for battery testing.

10.2 Optimizing the Cu₂Sb film deposition

Copper antimonide films were deposited electrochemically from room temperature aqueous solutions at a single reduction potential. This was achieved by examining the effect that the deposition parameters had on the films deposited from the

optimized deposition solution. It was determined that a deposition potential of -1050 mV vs. SSCE produced crystalline Cu_2Sb films with the correct composition and uniform cubic morphology. Potentials more positive to this produced Cu_2Sb films that were copper rich, and potentials more negative to this produced films of Cu_2Sb that were antimony rich. The effect the solution temperature has on the Cu_2Sb deposition was also examined, and as expected the crystallinity of the electrodeposited Cu_2Sb increased with an increase in temperature. It was also found that Cu_2Sb could be synthesized at all conducting substrates, but good adhesion of the formed Cu_2Sb leading to thin films was only found to occur on non-passivated metallic substrates. The smoothness of the substrate was determined to affect the crystallinity of the deposited film; the smoother the substrate the more crystalline the deposited Cu_2Sb . The films deposited are relatively free of impurities and are highly crystalline compared to Cu_2Sb samples that have been prepared using other methods reported in the literature. Following the results of the work discussed in Chapter 4, a procedure was developed that produces Cu_2Sb films that meet the requirements for battery testing.

10.3 Electron microscopy investigation of the electrodeposition of Cu_2Sb

The successful electrodeposition of crystalline intermetallics from aqueous solutions at a single potential is not common. To investigate the processes that occur during the nucleation and growth of Cu_2Sb a procedure was developed to deposit Cu_2Sb directly onto TEM grids. The results from these investigations described in Chapter 5 provide evidence that the single potential deposition of Cu_2Sb can be described by a combination of the ACD and IUPD models. While the times reported in this study are not quantitatively relevant to the depositions on “normal” substrates, this investigation is

unique because TEM grids were used as the working electrode; thereby providing direct compositional, morphological, and crystal structure evidence of the nucleation and growth process. This unique investigation unveiled that the nucleation sites undergo transitions that are not just based on the diffusion of the required elements to the substrate, but also on the interaction of the elements within the nucleation sites. The high solubility of copper and antimony in each other may be responsible for allowing the solid-state transformations required for the direct deposition of Cu_2Sb . The knowledge gained from these experiments will aid in developing a more complete understanding and ultimately better control of the single-potential deposition of crystalline intermetallics from aqueous solutions. The results were also used to aid in developing a procedure to uniformly deposit crystalline Cu_2Sb nanowire arrays.

10.4 Pulse potential deposition of Cu_2Sb nanowire arrays

The established procedure for the electrodeposition of Cu_2Sb films was used as a starting point to develop a procedure to electrodeposit Cu_2Sb nanowire arrays. It was determined that the single potential step deposition used for films led to poor reproducibility and non-uniform pore filling. To address these problems a pulse potential deposition procedure was developed. Reviewing the experiments performed on the pulse deposition of Cu_2Sb , a qualitative mathematical approach was developed to model the current and concentration behavior of the system during the experiments to provide insight in creating a successful deposition procedure. In the process of performing experiments and developing the qualitative mathematical treatment, the results of the nucleation studies performed in Chapter 5 were also used to develop the final deposition

procedure. Using this procedure, crystalline, uniform Cu_2Sb nanowire arrays were deposited from aqueous solutions.

10.5 Preliminary Cu_2Sb battery testing

Developing a procedure for the electrodeposition of Cu_2Sb permitted the exploration of Cu_2Sb films and nanowire array battery performance to be investigated. After addressing instrumental complications, it was demonstrated that the electrodeposited Cu_2Sb films had the same lithiation and delithiation profiles as is reported in literature for Cu_2Sb synthesized with different techniques. The preliminary battery testing also showed that there was an absence of charge associated with the formation of Li_2O , which supports that oxygen impurities are not present in the electrodeposited material. For the first time the electrodeposition procedure allowed the extrusion of the copper during the lithiation to be directly imaged using electron microscopy techniques without the obstruction of a binder. This allowed the morphology, composition and crystallinity of the Cu_2Sb to be monitored during different stages of the charge and discharge cycle. It was also demonstrated with the TEM investigation that Cu_2Sb can be reformed after one complete cycle if the charge and discharge rate is slow, supporting the conclusion that the large irreversible capacity loss observed during the first cycle is from kinetic and not thermodynamic issues.

10.6 Optimizing the battery performance of Cu_2Sb

After investing the details of the lithiation and delithiation of electrodeposited Cu_2Sb , battery testing was performed in order to optimize the cycle performance. Without the presence of a binder the number of cycles it takes to cause pulverization was found to depend on the thickness of the Cu_2Sb films and the rate at which they were

cycled. It was also determined that the pulverization only occurs if the Cu_2Sb is charged to a potential limit lower than 600 mV vs. Li/Li^+ . The improvement in battery performance of materials with small morphologies and high surface areas was demonstrated by the excellent performance of Cu_2Sb electrodeposited onto HSA copper foam. After 50 cycles at a rate of C/5 the material only lost 1% of the capacity, after the initial irreversible capacity lost that occurs during the first cycle. The Cu_2Sb deposited on the HSA copper foam was cycled at rates as high as 15C, after which only a 6% capacity lost was experienced after 90 cycles. These results support the theory that battery materials with high surface area experience less structural degradation during cycling. The testing of the battery performance of the Cu_2Sb nanowire arrays unfortunately was complicated by two procedural issues from electrochemically testing small amounts of materials. After these issues are addressed, the cycling performance of the Cu_2Sb nanowire arrays is expected to exceed that observed for the HSA foam. The procedure developed for the electrodeposition of Cu_2Sb nanowire arrays has also provided the first step needed for the fabrication of 3D solid-state lithium-ion batteries, which are currently being developed.